SANDIA REPORT
SAND2011-8080
Unlimited Release
Printed October 2011

Nanomanufacturing: Nano-Structured Materials Made Layer-by-Layer

P. Randall Schunk, Scott A. Roberts, Michael E. Chandross, Gary S. Grest, Hongyou Fan, E. David Reedy, James V. Cox, Kristianto Tjiptowidjojo, Shengfeng Cheng

Prepared by P. Randall Schunk
Sandia National Laboratories
Albuquerque, New Mexico 87185 and Livermore, California 94550

Sandia National Laboratories is a multi-program laboratory managed and operated by Sandia Corporation, a wholly owned subsidiary of Lockheed Martin Corporation, for the U.S. Department of Energy's National Nuclear Security Administration under contract DE-AC04-94AL85000.

Issued by Sandia National Laboratories, operated for the United States Department of Energy by Sandia Corporation.

Available to DOE and DOE contractors from
U.S. Department of Energy
Office of Scientific and Technical Information
P.O. Box 62
Oak Ridge, TN 37831

Telephone: (865) 576-8401
Facsimile: (865) 576-5728
E-Mail: reports@adonis.osti.gov
Online ordering: http://www.osti.gov/bridge

Available to the public from
U.S. Department of Commerce
National Technical Information Service
5285 Port Royal Rd.
Springfield, VA 22161

Telephone: (800) 553-6847
Facsimile: (703) 605-6900
E-Mail: orders@ntis.fedworld.gov
Online order: http://www.ntis.gov/help/ordermethods.asp?loc=7-4-0#online

SAND2011-8080
Unlimited Release
Printed October 2011

Nanomanufacturing: Nano-Structured Materials Made Layer-by-Layer

P. Randall Schunk*
Nanoscale and Reactive Processes Department, 1516

Scott A. Roberts
Thermal and Fluid Processes Department, 1514

Michael E. Chandross, Shengfeng Cheng
Computational Materials Science and Engineering, 1814

Gary S. Grest
Surface and Interface Science, 1114

E. David Reedy, James V. Cox
Component Science and Mechanics, 1525

Hongyou Fan
Ceramic Processing and Inorganic Materials, 1815

Kristianto Tjiptowidjojo
Department of Chemical and Nuclear Engineering, University of New Mexico

*Sandia National Laboratories
P.O. Box 5800
Albuquerque, New Mexico 87185-MS0834

Abstract

Large-scale, high-throughput production of nano-structured materials (i.e. nanomanufacturing) is a strategic area in manufacturing, with markets projected to exceed $1T by 2015. Nanomanufacturing is still in its infancy; process/product developments are costly and only touch on potential opportunities enabled by growing nanoscience discoveries. The greatest promise for high-volume manufacturing lies in age-old coating and imprinting operations. For materials with tailored nm-scale structure, imprinting/embossing must be achieved at high speeds (roll-to-roll) and/or over large areas (batch operation) with feature sizes less than 100 nm. Dispersion coatings with nanoparticles can also tailor structure through self- or directed-assembly. Layering films structured with these processes have tremendous potential for efficient manufacturing of microelectronics, photovoltaics and other topical nano-structured devices. This project is designed to perform the requisite

R&D to bring Sandia's technology base in computational mechanics to bear on this scale-up problem. Project focus is enforced by addressing a promising imprinting process currently being commercialized.

ACKNOWLEDGMENTS

Invaluable contributions to this project from Professor Bonnecaze of the University of Texas at Austin and S. V. Sreenivasan of Molecular Imprints Inc. and the University of Texas at Austin are greatly appreciated. We would also like to thank a Sandia summer intern Eric Benner and a University of New Mexico summer student Ethan Secor for their contributions.

CONTENTS

FIGURES

1. INTRODUCTION

1.1 High-throughput manufacturing – at the Nanoscale

"Manufacturing" implies "practical", which usually translates to low-cost and high-throughput production of a product. Of course this concept is central to many industries ranging from consumer products to high-tech materials and devices to large-scale transportation systems. Fabricating a film, fiber or monolithic material with controlled structure at the nano-scale is often prototyped on the bench-top but rarely goes beyond that. An explosion of such nano-material discoveries the past decade or more has resulted in the keen interest to scale-up experimental fabrication to a viable manufacturing processes.

So-called "Nano-Manufacturing" is a term becoming more popular in this regard. Basically, a nano-manufacturing processes is one which has truly achieved financial viability through clear connection (understanding) between process parameters and nano-scale structure. Since the 'nanoscale' had been defined as length scales of 10-100 nm in one physical dimension, then a successful nano-manufacturing process is one that successfully controls material microstructure at this scale. Several examples which could be categorized as nano-manufacturing are imprint lithography (10-40 nm feature sizes), nanoparticle dispersion coatings for conductive materials (10-100 nm feature sizes), and polymer processing co-extrusion (hundreds of layers less than 100 nm thickness per layer). Interestingly, enhanced photolithography using extreme ultra-violet (EUV) or immersion techniques seems to have hit a barrier at 100 nm feature size, although smaller features have been achieved but with much more expensive steps severely limiting economic viability.

Photovoltaic devices (PVs) are prime examples of products that require layered nano-materials for improved efficiency. This is particularly the case for so-called organic photovoltaic (OPV) devices, which are limited to a narrow range of applications because of their low-efficiencies (5-8% conversion). In contrast, silicon-based PVs can achieve efficiencies just shy of 50%, but they are much more expensive to produce, requiring vacuum technology and clean-room fabrication. In Figure 1 we illustrate a classic OPV cell. Layers of this cell include those for electrodes (anode and cathode) which are typically cast dispersions of colloidal particles, P-N junction layers which are structured at a level to minimize exiton diffusion lengths between the donor-acceptor interfaces, and light-capturing films structured for antireflection and other desirable optical traits. Each layer can conceivably be made and combined in an ultra-efficient process which accommodate flexible substrates and traditional techniques such as thin-film coating, drying, phase change, and imprinting. Actually, many companies are currently making organic photovoltaic products or components with efficient roll-to-roll processes (e.g. Konarka, 3M, Corning). However, achieving a low-cost integrated device with higher efficiencies requires more breakthroughs in materials-patterning at very small scales, and the manufacture of those materials in a high-throughput process.

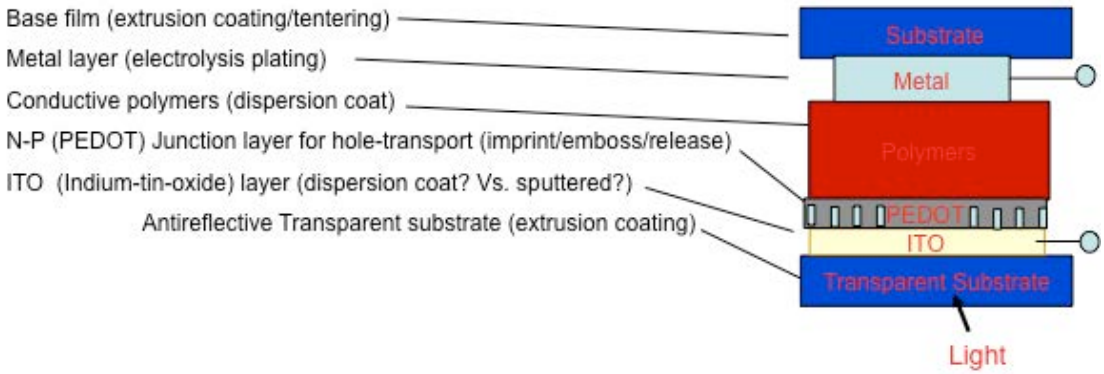

Figure 1: Schematic of an organic-photovoltaic (OPV) device

High-throughput production can be achieved in a number of ways. Broadly categorized, thin nanomaterials of the sort we focus on in this work can be made in "bottom-up" fashion, with nanopariticle building blocks or "top-down" fashion with a master template imprinting or embossing process (e.g. Gates and Whitesides 2003). Both of these approaches can conceivably be configured in a roll-to-roll setup, which would greatly improve throughput. Roll-to-roll can be configured for thin-film coating nanoparticle dispersions or imprinting (nano- or micro-gravure). Thin liquid film coating processes have been advanced for more than a century for many applications (cf. Cohen and Gutoff 1992) and are a subset of what is known in manufacturing circles as *polymer processing*, which includes traditional processes of extrusion, encapsulation and mold filling. The industry has evolved with more recent interest in esoteric processes of self-assembly of nanoparticles and micro/nano-imprinting and embossing. In fact, the diversity of coating and polymer processing operations ranges from precision, lab-scale techniques for delicate applications like molecular sensing or surface treatment with monolayers of molecules, to high-speed roll-to-roll operations with line speeds exceeding 10 m/s in the production of thin (less than 10 micron) coatings for use in the printing and adhesive tape industries. However, little has been done to scale-up methods for deliberately controlling structure at the 10-100 nanometer scale to high-throughput roll-to-roll configurations.

Advancing the underpinning science of patterning films mechanically (imprinting/embossing) or chemically/thermodynamically (polymerization, phase-change, self-assembly) at high-throughput is a major goal of this effort. Because roll-to-roll processing as pictured in Figure 2 is the best configuration to achieve throughputs necessary for large volume products, our work will focus on detailed multiphysics model research and development of imprinting or embossing mechanics in a roller-nip configuration, which typically includes a metering element for thinning the film (blade, knife, or another roll) and a substrate/soft-backing roll interaction. The metering element in this case will be patterned at the nanoscale, much as it is in mature batch technologies like the the Jet-and-Flash Imprint Lithography (J-FIL^{TM}) process (see Section 1.2.1). Our model R&D will focus on the fundamental mechanics problems of fluid-lubrication, capillary action, high-speed wetting, and solidification in such a configuration. As a companion to this effort, we will also initiate a concerted effort to scale-up self-assembly techniques to higher speed. Interestingly, roll-to-roll liquid film coating is ideal to put down films of nanoparticle dispersions and even solidifying them by solvent removal. However, beyond bench scale activities no effort has ever been made to speed up the assembly process with hydrodynamic forces, viz. blade

metering, etc. We will examine with modeling and simulation the physical barriers to achieving higher throughput as a part of this effort.

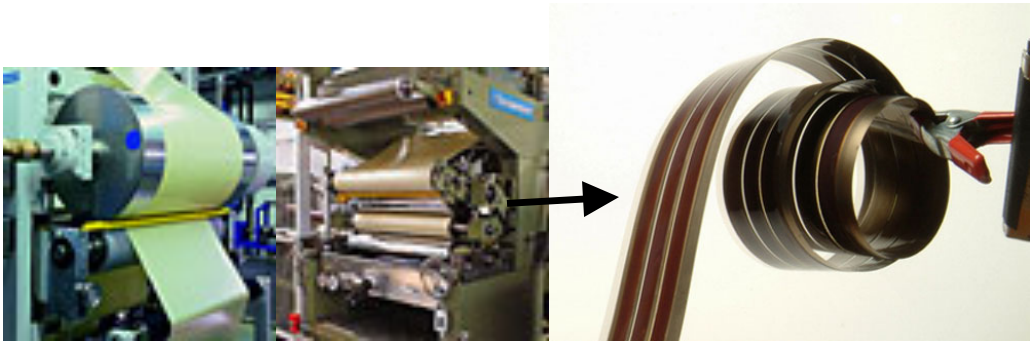

Figure 2: A typical roll-to-roll configurations for web-handeling and coating application (left) and a flexible photovoltaic device (printed with permission from Konarka Inc.).

The prototype process we use to define and motivate a sequence of interacting modeling capabilities is actually a step-wise batch process. However, most all of the physical elements which one would encounter in a roll-to-roll operation are addressed in this research and development, including deformable (wind-able) substrates and commensurate elasto-hydrodynamics, roll-on pressing, peel-off separation/release, and solidification. Ultimately what limits the industry is efficient production of integrated systems. Layer-by-layer registration like that which has been achieved with modern photolithography of electronic devices remains a challenge for many applications. Roll-to-roll bi-layer PV devices are an exception, as the interconnecting wires and parallel-cell construction has been achieved in a wind-unwind process as pictured in Figure 2.

1.2. Role of Modeling and Simulation in Scale-Up

Modeling and simulation at all scales (from quantum to continuum to system-level scales) has impacted discovery, design and even product/process qualification throughout the manufacturing industry. Examples are legion, including forming and casting, thin film coatings (liquids, vapor phase), joining (welding, soldering, brazing), integrated circuit and surface micro-machine manufacturing (crystal growth, chemical and wet processes), polymer processing (mold filling, extrusion, etc.), and so on. The impact modeling and simulation on the production of coated and printed products has been particularly significant and in fact has been integrated with process design ubiquitously for decades in industries such as those producing photographic, magnetic, adhesive, and related film applications. These products are clearly produced in large quantities and at relatively low cost per unit area, which is often the show-stopper in achieving significant market share.

Moving from continuous coating and drying to discrete coating, or printing in the liquid state, via an ink-jet, gravure or flexographic printing, etc. is significantly more challenging for modeling at the machine/product scale, as there is no frame-of-reference which keeps the process steady, except at the largest scales where the pattern is modeled as an effective medium. The same goes for imprinting and embossing processes. While many models have been useful at the feature scale (single or a few cells as pictured in Figure 3), little in the way of production capability has

been developed to account for the effects of a pattern on the machine scale. The challenge is one of multi-scale analysis, which is in essence the research we take up in this program.

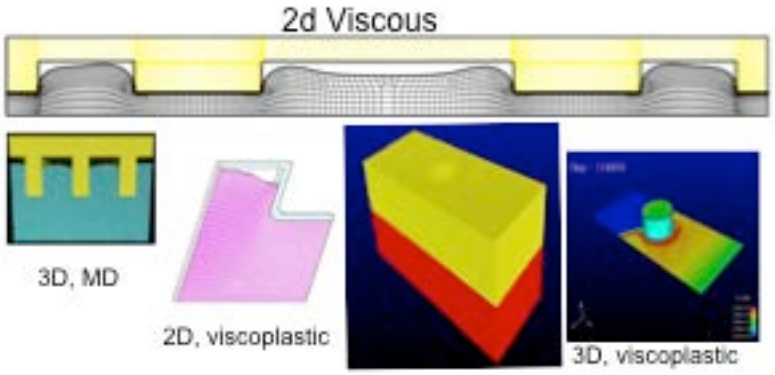

Figure 3: Molecular-level and continuum level analysis of imprinting and embossing processes at the single and multiple feature scale. All sample results here were obtained as a part of the scale-up problem of this LDRD research. Upper-most figure is a two-dimensional GOMA model of a hot-embossing process. Left, bottom is a molecular-level model (LAMMPS) of imprinting a polymer above TG. The bottom-right three figures are continuum results using PRESTO of embossing a single feature with a rigid mold.

Most successful nano-manufacturing processes derive from these age-old coating, printing and drying techniques that all have been highly advanced in a high-speed, high-throughput continuous roll-to-roll operation. However, in nano-materials many of these have not been migrated to flexible substrates which would enable roll-to-roll scale up.

Relevant modeling and simulation work addressing imprinting and embossing at micro- and nano-scales has been reported in the literature. Because this LDRD is largely focused on modeling and simulation approaches, we confine our literature review to efforts which develop or bring such tools to bear on process understanding and design.

Numerous efforts have been aimed at understanding the physics of fluid and plastic-solid molding at the feature scale. Essentially, embossing or imprinting is a small scale molding process in which a polymer (low- or high-molecular weight) is managed to fill small cavities in a substrate/template typically by "squeezing" the mold against a substrate on which the polymer is placed. Typical features sizes of interest to micro and nanotechnology are of course from tens of microns to tens of nanometers in width and depth. If the process is dominated by capillarity, viz. the polymer is drawn into the template because of its affinity to the surface and its low viscosity, it is termed "imprinting". If the process requires high pressures to force polymer into the features, it is typically termed "embossing". Of course there are many variations on these simple molding arrangements which involve thermal softening, in-situ polymerization/crosslinking, etc. In the imprinting regime, Chauhan et al. (2009), Reddy et al. (2005), and Stoyanov et al. (2011) have all posed two-dimensional models of pressure and capillary-induced filling of a single feature in a low-viscosity printing process. The features sizes ranged from 500 nm to 1 micron. Reddy et al. using a finite element model found that feature fills are characterized by a very rapid (ballistic) time scale due to wetting (solid-liquid

surface tension) which in turn leads to short regimes dominated by viscosity and inertia. That is, the process is anything but one which is dominated by capillary hydrostatics or by squeeze pressure. This mechanism is in stark contrast to the important underpinning physics of "embossing".

In polymer melt embossing, considering equipment costs, stamp durability and production rate, it is desirable to process the part at the lowest possible pressures and with the shortest possible cycle times. This involves several technical challenges, which have been comprehensively reviewed by Schift and Heyderman (2004). In the embossing regime, Rowland et al. (2005, 2008, 2009) presented a series of studies using a Lagrangian/Eulerian finite-element and free surface models to study single and multiple feature filling of a nanoimprint process known as nano-imprint lithography (or NIL), which is actually embossing. His models included effects of template heating, polymer/solid surface tension, template flexibility, and variable feature sizes. Burns et al. (2004) examined residual stress development in a single feature as the imprint polymer solidified through polymerization, using Lagrangian finite elements. Reedy et al. (2010) examined serveral elastoviscoplastic models at the feature scale, together with the effects of atomistic friction (cf. Chapter 2). These models together with numerous others are invaluable in the scale-up process as they lead to fundamental understanding of the controlling factors of feature shapes after mold/template release as well as the importance of long-range molecular forces (e.g. atomistic friction) and surface adhesion on the process. In fact, Chapter 2 of this report delves into these details with sophisticated finite element models and representative polymer constitutive equations at the feature scale.

Although we do not address feature-scale models in the imprinting regime any further in this work, it is important to mention that we build off of the work by Reddy et al. (2005) as we upscale to machine/wafer scales. In so doing we take on the unique aspect of accounting for the fate of the displaced gas in the process not only from fluid displacement but from dissolution (cf. work by Liang et al., 2007). In Chapter 3 we address our meso-scale and machine/wafer scale models of the nanoimprint lithography process with a unique blend of numerical algorithms designed to accommodate the governing physics. The goal of that work is a true coarse grain model that not only captures the dynamics of the process but also allows defects at the feature scale to be detected. Our work does have precedence, albeit sparse and only in the nano-embossing regime..

The NanoImprint Simulation Software (NSS) marketed by COGNOSCENS (2010) actually simulates at the wafer scale an embossing process using lubrication theory (similar to our approach), but in a unique, localized way which we believe is not applicable to the lower-viscosity imprinting case. Nonetheless their expedients allow them to model at a larger scale. Taylor et al. (2009) also advanced and tested a reduced-order model approach to simulating the microembossing of thermoplastic layers. Their model is again similar to the one we pose in Chapter 2, but stops short of a true generalization to the wafer scale and does not accommodate the flexure of the template or substrate which we found to be essential at such high pressures in embossing. Reddy and Bonnecaze (2005) did upscale here single feature model (Reddy et al. 2005) to scale which included a mix of holes and trenches in a substrate with a multiphase flow model. This work actually motivated our starting point in Chapter 3.

In this work we will focus on the fundamental processes of coating and printing, imprinting, solidification and release of patterned templates at scales ranging from molecular to continuum, or so-called "engineering scales". This breadth is in fact the challenge. The hope is that our predictive tools account for the complex relationship between the nano-scale features and physics (surface features, molecular forces, particle microstructures, etc) and controllable or measureable material properties and process parameters (coating speed, imprinting speed, material properties, etc.). We will not be addressing directly any continuous processing systems. Our models are all formulated in the batch sense, but we have included some of the key physical features of a flexible roll configuration, like flexible substrates and roll-on stamping dynamics. To guide our models and ground them in actual processing conditions, we have chosen the Jet-and-Flash Imprint Lithography process which is introduced in section 1.2.1.

1.2.1 Nanomanufacturing Prototype: Jet and Flash™ Imprint Lithography (J-FIL™)

Figure 4 illustrates the essential steps of the J-FIL™ process developed by researchers at the University of Texas at Austin (cf. Sreenivasan 2008) and commercialized by Molecular Imprints Inc. (MII, www.molecularimprints.com). MII actually makes highly sophisticated machines which manage the imprinting as a batch stepper process. These machines control the various electrical and mechanical (fluid and solid) steps of the process to exceedingly small tolerances and under environmentally controlled conditions.

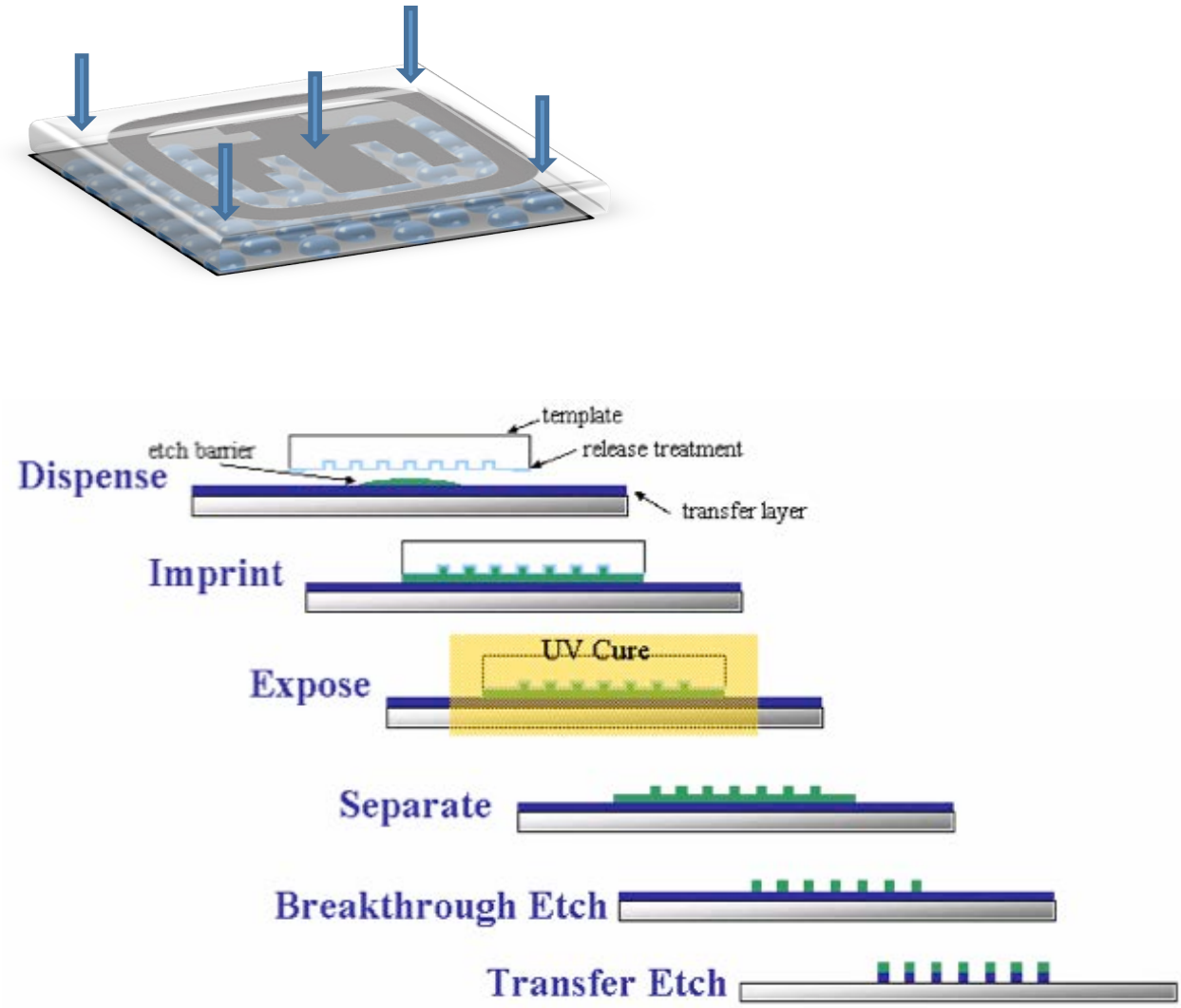

Figure 4: Pictorial (top) and individual steps (bottom) of the Jet-and-Flash™ Imprint Lithography process.

The machines are designed to maximize speed and minimize defects of producing surface structures controlled to the tens of nm-scale. Machine design improvement always faces major technological challenges (as the high-cost of these machines attests), especially for low defect tolerances required by the hard disk drive and semiconductor industries. Our work here aims to aid in surmounting several of the underpinning physical and material science barriers with simulation-based R&D connecting nm- to machine-scales. Our models described in later chapters of this report will be tested and validated with some of the diagnostics and visualizations of this process.

As shown in Figure 4, J-FIL™ deploys the generic sub-processes of imprinting/embossing, coating, and drying. Our algorithm R&D, model development, and experiments under this LDRD are aimed at answering the key unknown materials and physical science issues which lead to defects at the feature scale. Information at this scale will then be deployed in novel

manufacturing-scale simulations. The steps of the process (referring to Figure 4) are discussed first. Our research is focused on Steps 2, 4, and 5 as they represent the largest source of defects and the largest barrier to *throughput*. We have developed computational technology which can be applied to step 1 which too is described.

In step 1 a photo-curable polymer coat (photoresist) with 3-5 picoliter droplets is dispensed over the wafer surface in a pattern related to that of the template. This dispensing step is basically accomplished with a novel ink-jet technology which receives pattern information from the digital design. In step 2, a pre-fabricated flexible master /template is pressed (imprinted) into the liquid layer. The underlying physics of this step involves fluid-structure interaction, multiphase flow with drop coalescence, wetting/dewetting, and flow into nm-scale features. This step is most prone to defects under current applications. In step 3 the photoresist is cured with UV light. In this step residual stress develops and influences step 4. In step 4, the master is peeled (released) from the solidified polymer. Fracture and adhesion are common defects in this step. Finally, in step 5 et seq. further processing can be undertaken depending on the application, including coating a suspension of nanoparticless with direction to imprinted features.

With the photocurable polymers typically used in J-FIL, curing takes only milliseconds. Imprinting and release rates are of the order of 5-10s. Hence, *throughput* is best increased with faster imprinting and release. Note that every process here could be carried out in a roll-to-roll fashion using a master roll and subsequent pre-metered dispensing and embossing of coatings.

To achieve a higher-throughput process beyond the step-and-print batch configuration, it is important to understand some of the distinguishing physical aspects of imprinting 10-30 nm features over large areas. First off, the substrate is not flat at some level larger than the atomic scale and smaller than what is known as "surface roughness". Current applications deploy highly polished silicon wafers, which still exhibit a roughness known as 'nano-topography'. This is a long-range roughness characterized by up to 5 nm in height variation over lateral distances of one mm to one cm. The presence of this scale of "non-flatness" of the substrates clearly necessitates a flexible template, as a rigid one would come into solid-solid contact before the imprinting process is complete. Clearly, the process must also be carried out in a very clean environment. A speck of dust of the order of 1 micron would lead to defects far greater than the size scale of the features (order 10-30 nm). Finally, the imprint media is a low-viscosity liquid. A higher viscosity would lead to very large pressures and hence lead to other mechanical challenges. Although these features and the challenges they present have been largely surmounted in the batch-step process, they pose serious challenges for scale-up to a roll-to-roll configuration. Achieving such scale-up would be the subject of further engineering research. Luckily, a flexible substrate as well as template may alleviate some of these problems.

1.2 2 Specialized capability for modeling and scale-up

A process such as J-FIL^{TM} has distinguishing physical features which require modeling and simulation capabilities beyond which current commercial and in-house codes (viz. COMSOL, SIERRA Mechanics or GOMA) support. As a result, we had to undertake the requisite R&D to accommodate these features with algorithm additions and improvements. Throughout this report we detail these code extensions and the underpinning R&D (see for instance Section 3.2.2). In this section we give the reader a broad overview and underpinning drivers for each development.

The main features which are either handled inefficiently with typical mechanics software or are just plain unavailable are

- High aspect ratio regions
- Multiple scales (feature to template to machine)
- Fluid-structural interactions
- Multiphase (liquid-gas interactions)
- Surface forces are significant in the process (adhesion, capillary wetting, stiction, etc.)

We should point out that often our go-to mechanics codes can accommodate many of these features in bulk, 2D or 3D continuum elements, but rarely are they able to handle them in combination and efficiently enough for large-aspect-ratio regions. In some cases, such as the ability to accommodate multiple scales, the improvements are a matter of developing the underpinning equations which either allow for coarse-grained averages or effective-medium theories, or fine-grained, sub-grid-scale physics. In other cases the improvements are a matter of algorithm upgrades and the addition of boundary conditions and couplings. We introduce each of these in turn at this point, and give more detailed descriptions in later chapters.

High-Aspect-Ratio Regions

- Shell Element Technology: Shell-Elements are reduced-order continuum finite elements integrated with presumed mechanical response in one direction. They are particularly useful for modeling mechanics in thin regions, or regions of very high aspect ratios where continuum elements are known to lead to inaccuracies and are expensive. Examples we use or develop in this research are membrane, inextensible shell, lubrication, porous shells. Numerically, shell elements posses three spatial dimensional coordinates but only two integration coordinates. We have developed and integrated true curvilinear shell capability for lubrication (first of its kind to our knowledge integrated with continuum codes), porous penetration, and integrated structure.
- Coupled shell elements and continuum elements compatible with parallel solvers.
- Boundary condition coupling between shell physics and continuum physics: porous penetration, fluid-structure interaction, etc.

Multiscale analysis (effective medium theory for template filling)

As indicated in Figure 5, there are six orders-of-magnitude in length scale separating an individual feature and the entire wafer of a current JFIL operation. At each scale we can capture specific underpinning features. Specifically, for imprinting processes, the numerical/algorithmic developments we undertook in this regard are:

- Pore-level porous penetration models based on presumed hole size, surface-interaction (contact angle), dynamic effects (dynamic contact angle), and gas compression.
- Pore-level models were coarsed-grained into wafer-scale saturation models with the shell-element equation framework outlined above.
- Gas-dissolution model.
- Open-pore model for different template microstructures integrated into shell equations.

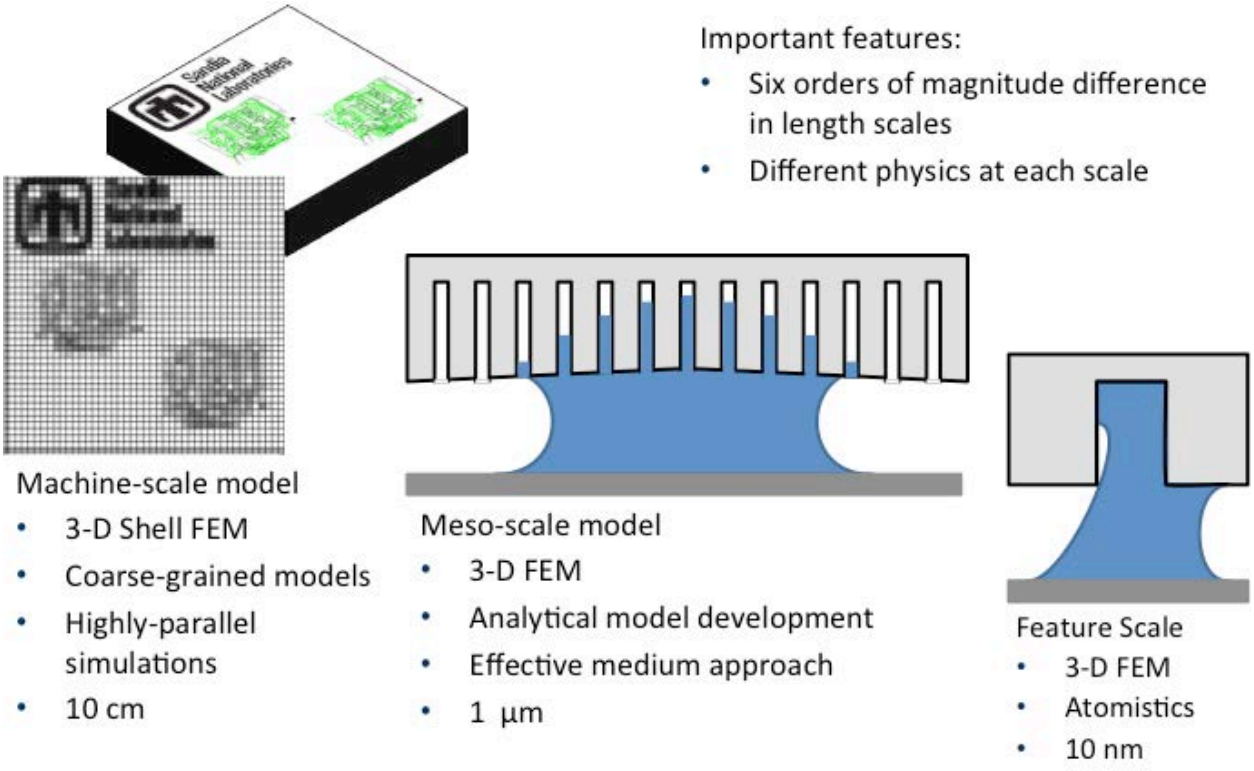

Figure 5: Multiple scales and suggested/taken approaches to modeling of the J-FIL™ process.

Multiscale analysis of release process (effective toughness models for atomistic friction and adhesion)

Novel developments for models of this portion of the process focused on effective adhesion/de-adhesion of corrugated/patterned layers as they are pulled away from the template. Up-scaling from the unit-sell model to the course-grained machine model is described in Chapter 2.

- Effective pattern T-U relationship is defined as the total applied normal force/nominal initially bonded interfacial area vs the edge displacement.

Fluid-structural interactions.

Structural compliance of the template and/or substrate is an essential aspect of nano-imprinting. Because substrates cannot me fabricated perfectly flat, the template must conform to the substrate in order to achieve the feature pattern with minimal residual layer thickness. Several forces are at play in the interaction of the imprint fluid and solid.

- Overpressure due to deliberate flexure of the template on application. This required specific boundary conditions.
- Capillary pressure and lubrication pressure interaction with template flexure. This effect required a specialized fluid-structural boundary condition.

Multiphase (liquid-gas-solid interactions)

Efficient filling of the imprint template is best accomplished with discrete patterned coating using ink-jet printing technology which generates a pattern in line with the template to be filled. As such, the imprinting process involves multiphase (gas and liquid) flow. At the droplet level

this requires a method to track the drop boundary as it spreads and is compressed by the capillary action/suction of the flexible template. To accommodate these events, and deal with the trapped gas, we advanced the following models/algorithms.

- Integrated a level-set front tracking algorithm with the lubrication shell equation.
- Reformulated the surface forces term of the lubrication equation to account for surface pressure jump due to capillarity (unique).
- Used a novel front sharpening approach to more accurately account for the capillary pressure jump in the surface forces term.

Differential Wetting and Spreading

Distributing imprint photoresist in a pattern prior to the imprint step can be accomplished in a number of ways. Although the current JFIL process uses ink-jet like technology, another way to achieve a patterned liquid coating is to coat a hydrophyllic-patterned substrate. To this end, we developed the requisite numerical technology to model such events (see Chapter 4).

- Developed and implemented thin-film lubrication equations. Novel additions include a particle convection-diffusion equation for nanoparticle films, and drying.
- Developed and implemented a conjoining-disjoining pressure forces in the thin film equations through which we can specify the pattern of wettability on a substrate (using the pattern to mesh tool described in Chapter 3).
-

Additional surface forces and subscale phenomena

- Atomistic studies were undertaken to determine contributions to adhesion due to molecular forces, cohesive failure, atomistic friction. (see section 2.1).
- Development and implementation of a gas-dissolution model (see section 3.2)

In addition to physical models and algorithms, there are several additional requirements on supporting software which required further development.

- To accommodate general feature patterns (holes, lines, etc.) we undertook the development of a generalized pixel-image to mesh mapping capability that deployed least-squares fitting. Effectively, the capability requires the solution of an over-determined system of equations (more pixels than mesh), which necessitates the solution of the normal equations equivalent. Further discussion of this is giving in section 3.3. We used this capability for the imprint steps (Section 3.3) and the patterned coating steps (Section 4.1).
- Re-wrote domain decomposition capability to accommodate the distribution of a problem which contains both shell elements and continuum elements.

1.3 Report Organization

Over the course of this three-year LDRD project, we have managed to maintain a connection between the individual projects and the overall goal. While not perfect, we can claim that all aspects and all scales of top-down nanomanufacturing have been assessed in this work. We have even crossed over to the use of nanoparticles (a bottom-up building block) coupled with top-down patterning. While we discuss little of our experimental effort in this introduction chapter, this project does have one component which could have future impact on imprinting.

Chapter 4 examines the influence of imprint pressure on imprint fluid laden with nanoparticles, and furthermore shows an interesting directed-assembly affect. Moreover, our partners at Molecular Imprints Incorporated, University of Texas at Austin, and Advanced Materials Laboratory at the University of New Mexico have all provided motivating experiments and in one case validation experiments (cf. Section 3.3). The table below is intended to give the reader and the LDRD program a snapshot of the activities funded under this LDRD project and their relationship to the test-bed process (JFIL) and at what scale they address. Those activities with a number reference are given a more detailed description below the table, together with a guide to the chapter in this report which addresses it.

Projects/Activities ***Scale***	Approach/Modeling			
	Atomistic/Molecular	***Feature***	***Machine***	***Experimental***
"Solid State" emboss/Release	Chandross/Grest 1	Reedy 2	Reedy 2	UT/MII 3
"Liquid State" imprint/solidify	Extract prior work, 1, 5	Extract prior work, 5	Schunk, Roberts, et al. 6,7	UT 4
Dispersion/Particulate	LAMMPS MD 8 -->	LAMMPS Colloid Package 8	Goma 10	Fan et al. 12

1 Traction/separation law derived with aid from MD/atomistics – Chapter 2.
2 Traction/separation model from coarse graining. Effective toughness. Chapter 2.
3 Experimental confirmation/validation from Molecular Imprints/UT.
4 Experimental validation from UT/Molecular imprints. Chapter 3.
5 Use work previously funded at UT and literature (wetting, fill/no-fill) - Chapter 3.
6 Feature and repeat-unit level models with Goma (Lubrication, continuum, 3D). Chapter 3.
7 Machine scale models with generalized shell Elements (Goma) – Chapter 3
8 Nanoparticle directed assembly by drying. Chapter 2 and 4.
10 Reynolds film flow with nanoparticles at continuum scale – Chapter 4.
11 Ongoing work by H. Y. Fan et al. -- Microstructure of nanoparticles during embossing-Multiple features FY11.

In summary, significant progress according to the planned milestones has been made and is demonstrated in this report. We are left with significant new capability that can be used to

generate new partnerships and new business. Those capabilities are largely embodied in computer software (GOMA, PRESTO, LAMMPS). Significant impacts have already been realized. We have interest from several companies (3M, P&G and others) for future CRADA work based on our developments. An NSF Engineering Research Center which involves Sandia and the University of New Mexico is likely going to be awarded to the UT Austin. Our involvement in this ERC stemmed from this project. Research grants to study the manufacture of patterned media have been received from 3M and P&G at the Advanced Materials Laboratory. Significant intellectual property has been developed and conveyed to the research community through four open literature publications and more than ten presentations at scientific/engineering conferences including MRS, AIP, AIChE, NanoTech 2009, 2010, and others. Finally, unexpectedly the capabilities researched and developed in Chapter 3 of this report can be directly credited for 3+ years of additional funding from an important WFO project. In that project the lubrication models coupled with fluid-structure interaction and thermal shell effects have been pushed into the turbulent regime. That together with the pattern-to-mesh tool has enabled Sandia to become the leading contributor to the understanding of high-speed, melt-lubricated contacts.

2. EMBOSSING AND RELEASE

2.1 Embossing and Release Model at the Molecular Scale

Introduction

Several alternative approaches towards nanostructure fabrication have been developed recently. These techniques include micro-contact printing or soft lithography (e.g. Zhao et al. 1997) nanoimprint lithography (e.g. Chao 1995) and dip-pen lithography (Piner 1999). A good overview of several of these various techniques can be found in Gates et al. (2005). Here we are interested in modeling nanoimprint lithography in which hardening of the polymer is achieved either by cooling a thermoplastic polymer melt below T_g or crosslinking the polymer using UV light. The former is often referred to as hot embossing while the later is known as step-flash imprint lithography (SFIL) (Ruchhoeft et al. 1999). Nanoimprint lithograph can achieve feature sizes in the sub-50 nm range in polymer films that are generally much thicker than the desired imprint height.

SFIL and hot embossing are both multi-step processes in which a liquid based polymer solution is dispensed onto a substrate, the solid mold/template pressed into the liquid and filled, the polymer is cured and the template removed. The main difference between the two is in the curing process. For hot embossing, a thermoplastic polymer such as poly(methyl methacrylate) which has a glass transition temperature T_g above room temperature is first heated above T_g prior to the mold being pressed into the polymer. The temperature is then reduced below T_g. For SFIL, the polymer is a UV-curable resin and the mold chosen so that it is transparent to ultraviolet light. One advantage of the SFIL process is that it can be carried out at room temperature. While the SFIL process is quite cost effective ($10^{\wedge 9}$ dots of liquid can currently be dispensed for less than \$1.00) the two barriers to commercialization beyond a few niche applications are elusive long-range order without defects, as discussed above, and the rate-limiting steps of spreading the UV-curable resin and the curing process, which can take between 3-40 s per imprint/release process depending on the template type (Sreenivasan et al. 2008).

While a number of corporations have commercial machines that perform these types of nanolithographic processes, there has been little in the way of modeling. One exception is the recent work of Carrillo and Dobrynin (2009) who modeled nanoimprinting of hemispherical particles. They found the quality of the replication process is an optimization of the surface energy of the mold-liquid interface and the elastic energy of the polymeric mold. In this paper we will discuss the results of large-scale molecular dynamics (MD) simulations aimed at understanding the imprint and release steps, with particular emphasis on feature retention. First we investigate the nanoscale details of the SFIL process with fully 3D models that can access a much wider phase space than experimental studies. Our work centers on rigid stamps impressed into a melt of entangled polymer chains which is then cured (crosslinked) in order to study the basic dynamics of the process and to understand the complicated release process.

In the next section, we provide a brief description of the model used for the polymer matrix and the stamp, together with a description of the simulation methodology. In Sec. III, we present our

results for the stamp insertion process. In Sec. IV we present simulations for the SFIL process, while in Sec. IV we present results for hot embossing. In Sec. V, we summarize our results.

Simulation Details

We use a bead-spring model to simulate the polymer melt (Kremer and Grest 1990). The polymers are treated as freely jointed bead-spring chains of N monomers, or beads, of diameter σ and mass *m* which interact through the standard Lennard-Jones 6-12 potential cutoff at r_c=2.5 σ,

$$U(r) = 4\,\varepsilon_{11}\,\left((\sigma/r)^{12} - (\sigma/r)^{6} \right). \qquad (1)$$

Here $\varepsilon = \varepsilon_{11}$ is the interaction strength between polymer monomers. Beads in a chain are connected by an additional finite extensible nonlinear elastic (FENE) potential (Grest and Kremer 1986) with a spring constant $k = 30\varepsilon/\sigma^2$ and maximum extent $R_0 = 1.5\,\sigma$. The polymer films were constructed following the methodology of Auhl *et al*. (2003). The polymer films were initially equilibrated between two repulsive featureless walls in which the interaction between a polymer monomer and the wall is modeled as

$$U_{wall}(z) = \varepsilon_w\,\left(2/15(\sigma/z)^{9} - (\sigma/z)^{3} \right), \qquad (2)$$

where z is the distance of a polymer monomer normal to the wall. Periodic boundary conditions were applied in the x- and y-directions with L_x=180 σ and L_y=40 σ. The top wall was then removed and allowed to equilibrate prior to the introduction of the stamp. The interaction of the polymer with the lower wall was increased to ε_w=4.0ε and the range of the interaction extended to z_c=2.5 σ to avoid debonding of the polymer from the substrate when the stamp was removed. For weaker ε_w failure occurred at the substrate which is not of interest here.

The equations of motion were integrated using a velocity-Verlet algorithm with a time step $\delta t = 0.01\tau$, where $\tau = \sigma(m/\varepsilon\}^{1/2}$. The temperature was held constant at the desired temperature by a Langevin thermostat (Grest and Kremer 1990) with damping constant $\Gamma = 0.5\tau^{-1}$. For SFIL, random-crosslinking (Grest and Kremer 1990) is carried out by instantaneously adding FENE bonds between randomly chosen pairs of beads separated by less than the reaction distance of 1.3*σ*. For hot embossing, after imprinting the polymer we lowered the temperature below the glass transition, which for a polymer melt of long chains for this model is $T_g \sim 0.5\,\varepsilon/k_B$, where k_B is the Boltzmann constant (Baljon and Robbins 2001).

The stamp was made of a rigid fcc block of atoms of the same diameter σ. The polymer monomers and atoms in the stamp also interacted with a Lennard-Jones interaction, eq. (1), with an interaction strength ε_{12}. The polymer chain length of N=500 is above the entanglement length $N_e =85 +- 7 (Hoy et al. 2009). The number of chains for all simulations was 1200 while the number of atoms in the stamp varied from 298925 to 379250 depending on the number of stamps. In all cases, the stamps were continuous across the periodic boundary conditions in the y-direction, i.e. perpendicular to both the features as well as the insertion/removal directions. This results in stamps that are effectively infinitely long in one dimension, and reduces the size of the phase space from fully three-dimensional stamps.

As the interaction strength ε_{12} between the polymer and the stamp is typically known only indirectly through the contact angle between a polymer and the stamp, we carried out a series of simulations in which a solid stamp is inserted into bulk polymer solution and equilibrated at fixed temperature. Results for the contact angle as a function of polymer-stamp interaction for $T=0.7\varepsilon/k_B$ are shown in Fig. 6. In the simulations presented here we set $\varepsilon_{12} = 0.3$ or $0.6\ \varepsilon$, to model systems in which the stamp walls are either weakly interacting (coated) or strongly interacting (uncoated). While, crosslinking the polymer for SFIL has little effect on the contact angle, the change in temperature for hot embossing has a strong effect on the contact angle as shown in Fig. 7. Here we show a snapshot for the single stamp after cooling from T=0.7 to $T=0.3\ \varepsilon/k_B$ or about 0.6*Tg. The contact angle, which was initially ~90^o is now much lower and the polymer partially wets the stamp. This is likely a real effect that occurs in the manufacturing process and should be considered when making a choice of monomer solutions.

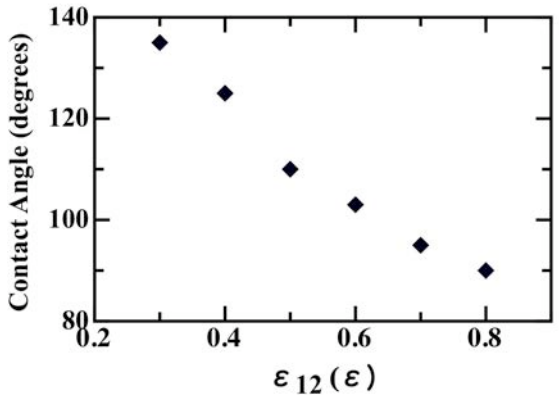

Figure 6 Contact angle between polymer and rigid stamp for $T=0.7\varepsilon/k_B$ as a function of polymer-stamp interaction ε_{12}.

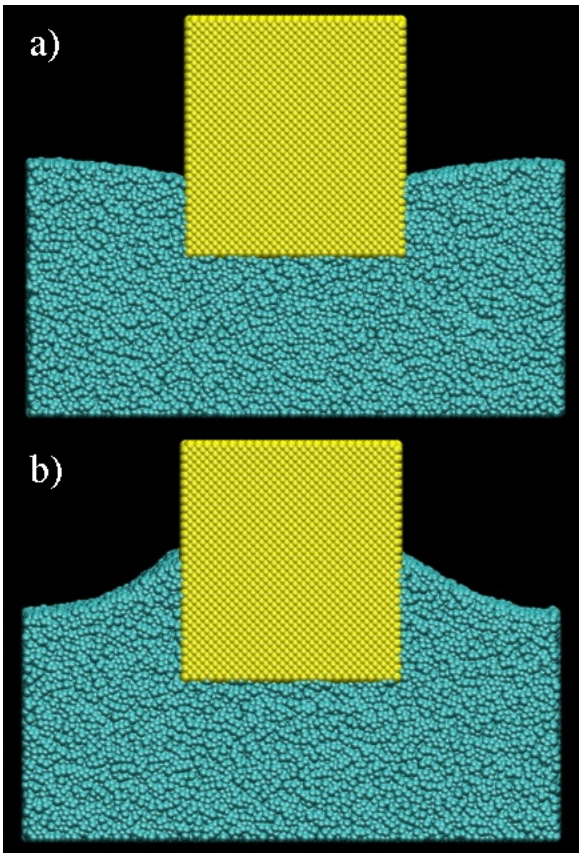

Figure 7 Snapshot of simulation after insertion of stamp (yellow) into polymer (blue). The system has been equilibrated at T= 0.7 ε/k_B in (a) and then cooled to T=0.3 ε/k_B in (b). The interaction strength between the stamp and polymer monomers is ε_{12}= 0.5 ε.

Stamp Insertion

The stamp is inserted into the polymer melt at $T=0.7\varepsilon/k_B$ or $1.4xT_g$, at a fixed velocity $v_z=0.005$ σ/τ until the mold is completely filled. In order to determine when the mold is completely filled, it is necessary to monitor the density of the polymer film deep below the stamp during the insertion process. It is also important to know at what density the process should be stopped. For SFIL we stopped the compression when there was a slight over pressure and the density of the polymer $\rho=1.0\sigma^{-3}$. However we also performed simulations in which the molds were compressed to densities as high as $\rho=1.3\sigma^{-3}$ and found little effect on the final structures. For the hot emboss process, it is important to consider that the polymer density increasing upon cooling. Figure 8 shows the density of a bulk polymer melt from a separate simulation of 500 chains of length 500 in a periodic simulation cell as a function of temperature with the initial (T_i) and final (T_f) temperature of the hot embossing studies indicated. The system is cooled in an NPT ensemble at rate of
10^{-4} $\varepsilon/k\_B/\tau$. Therefore for this case we use the density of the polymer at $T = 0.3$ ε/k_B, $\rho=1.064\sigma^{-3}$ as the target density, so that upon cooling the polymer does not pull away from the stamp. Note that that the SFIL simulations are all performed at T_i, only the hot emboss simulations are cooled to T_f.

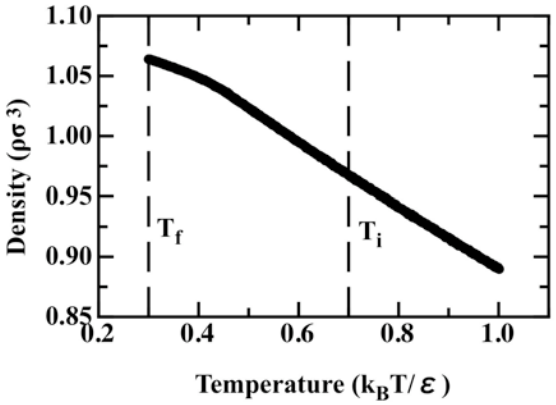

Figure 8: Density of the polymer melt as a function of temperature. Initial and final simulation temperatures are labeled on the plot.

We chose systems with three, four, or five total stamps in the simulation box, although, as discussed above, periodic boundary conditions effectively make these all infinitely long stamps. Snapshots during a simulation showing insertion of a system with three stamps are shown during filling (Fig. 9a) and when the mold is filled (Fig. 9c). The peaks in the polymer melt between the posts in Fig. 9a are likely due to the high insertion speed in our simulations, and relax to the appropriate contact angle after equilibration as shown in Fig. 9b. These snapshots are representative of the setup of a typical simulation. The size of the stamp posts themselves are not varied, so that by using more stamps the pitch of the remaining features (i.e. after stamp removal) will be changed. Using $\sigma \sim 1$ nm for the bead size, the stamps are approximately 18 nm across, leading to resulting feature sizes of 42 nm, 27 nm, and 18 nm for the three, four, and five stamp systems, respectively.

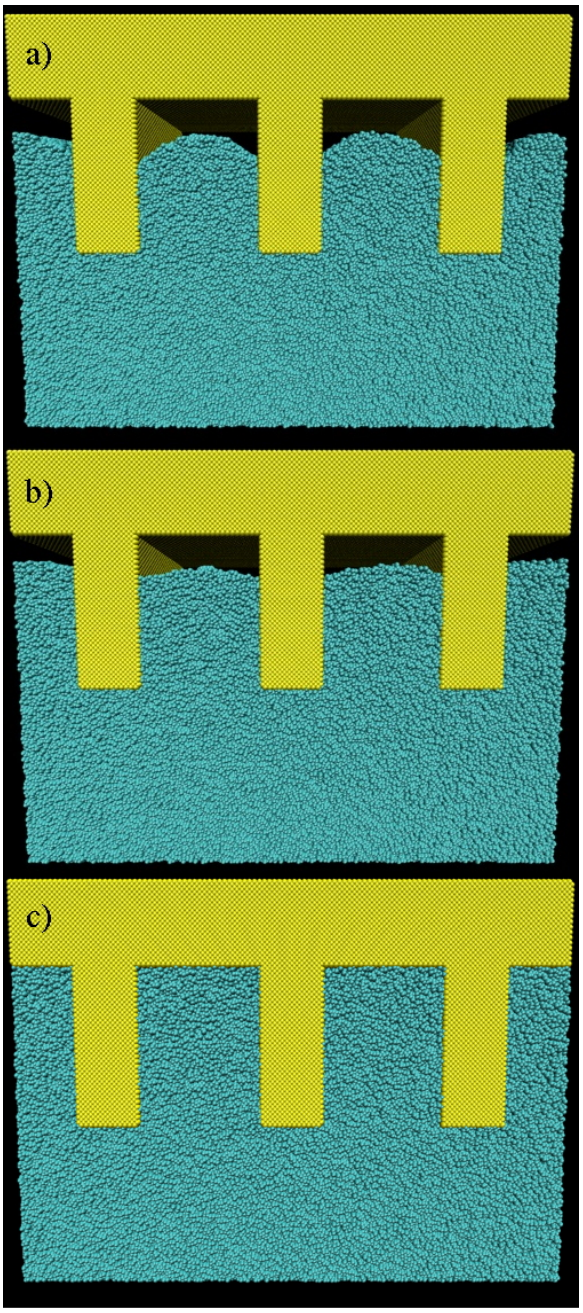

Figure 9: Snapshots of simulations with three stamps (a) during insertion (b) after 30,000τ of equilibration and (c) after full insertion. Polymer atoms are colored turquoise and stamp atoms are yellow.

The height of the stamp posts is set to be approximately half the height of the polymer melt. This allows us to insert the stamp fully while still monitoring the pressure and density of the polymer melt far from the tops of the posts. The density in the region between the tops of the posts and the bottom plate during insertion is shown in Figure 10 for the three systems. As the posts insert into the melt, there is a slight linear increase in density, but the melt is able to accommodate the posts. When the melt reaches the top plate of the stamps, there is an abrupt increase in density as indicated by the knees in the density curves. At this point the density

increases slightly sublinearly. We have examined the density in the polymer as a function of the strength of the polymer/stamp interactions and found that there is no effect, as expected.

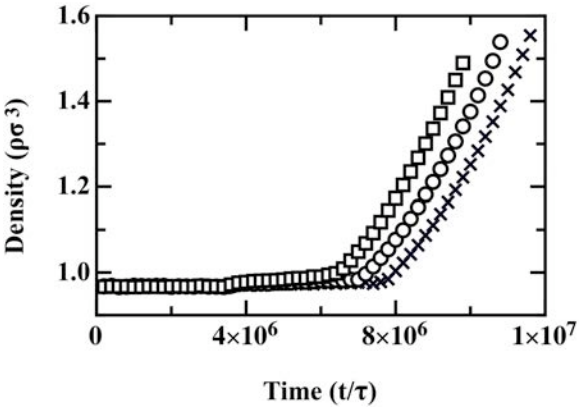

Figure 10: Density in polymer melt during insertion of stamps with three (x), four (O), and five (□) posts. The stamp/polymer interaction strength is $\varepsilon_{12}=0.3\varepsilon$.

Step-Flash Imprint Lithography

For the SFIL process, after filling the mold, the polymer is crosslinked, then equilibrated for 4,000τ in an NVT ensemble before the process is reversed and the stamp removed from remove from the polymer film.Two methods to remove the stamp were examined. In the first, the stamp is removed instantaneously by deleting all stamp atoms from the simulation cell. This is effecitvely a zero-stress removal of the stamp, as it does not lead to any fricitonal or adhesive forces being placed on the hardened polymer, as would occur during a forced pull-out. We have performed such zero-stress stamp removals for systems after crosslinking with 100,000, 200,000 or 300,000 crosslinks, corresponding to one crosslink for every 6, 4 or 2 monomers. After the stamp atoms were removed, the remaining polymer was equilibrated for 20,000 τ. Snapshots of the resulting systems, which are stable and do not change with time, are shown in Fig. 11.With 6 crosslinks/monomer (Fig. 11a), feature retention is poor, with visible curvature at the tops of the features, and weak definition of the remaining channels between them. Increasing the number of crosslinks to 1 crosslink per 4 monomers (Fig. 11b)results in very good feature retention, with only slight curvature at the sharpest corners. Some improvement is still seen upon increasing to one crosslink every 2 mononers in Fig. 11c.

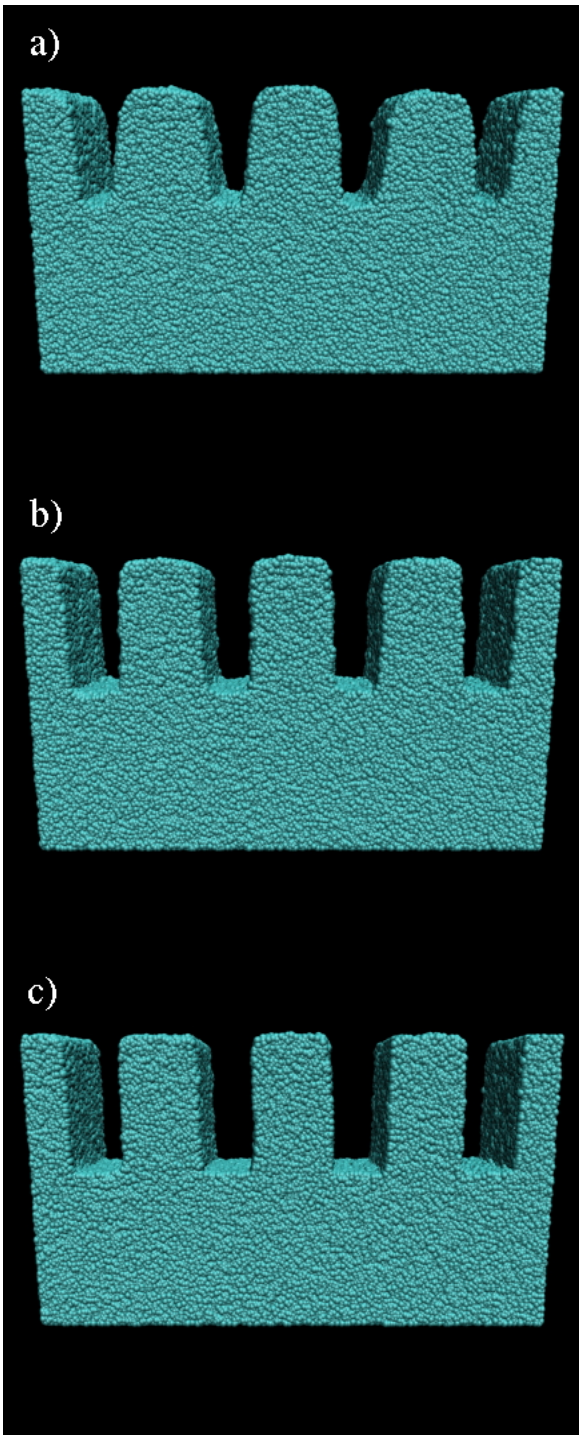

Figure 11: Snapshots of simulations showing equilibrated features after zero-stress stamp removal for systems with (a) 6 (b) 4 and (c) 2 monomers/crosslink.

For a more accurate depiction of the actual SFIL stamp removal process, we removed the stamp from the polymer at a fixed normal velocity and investigated the effects of the adhesive polymer/stamp interactions on the features. For a weak polymer/wall interaction (equal to the polymer/stamp interaction of $\varepsilon_{12}=0.6\varepsilon$), we find complete detachment of the polymer from the lower flat wall upon "removal" of the stamp. This effect can be mitigated, however, by

increasing the strength of the wall-polymer interaction. An increase of this interaction by a factor of more than three (such that ε_{1w}=2.0) does not prevent adhesive failure at the wall in our simulations, but we find that an additional factor of two (i.e. ε_{1w} = 4.0) is nearly effective. As shown in Fig. 12b, upon removal of the stamp there is a small section of polymer that undergoes adhesive failure directly under the second stamp from the left. This, however, is not enough to prevent removal of the stamp from the polymer as is clear from the figure. The features above this area of wall-stamp failure, however, are slightly raised relative to the remaining features, where no failure has occurred.

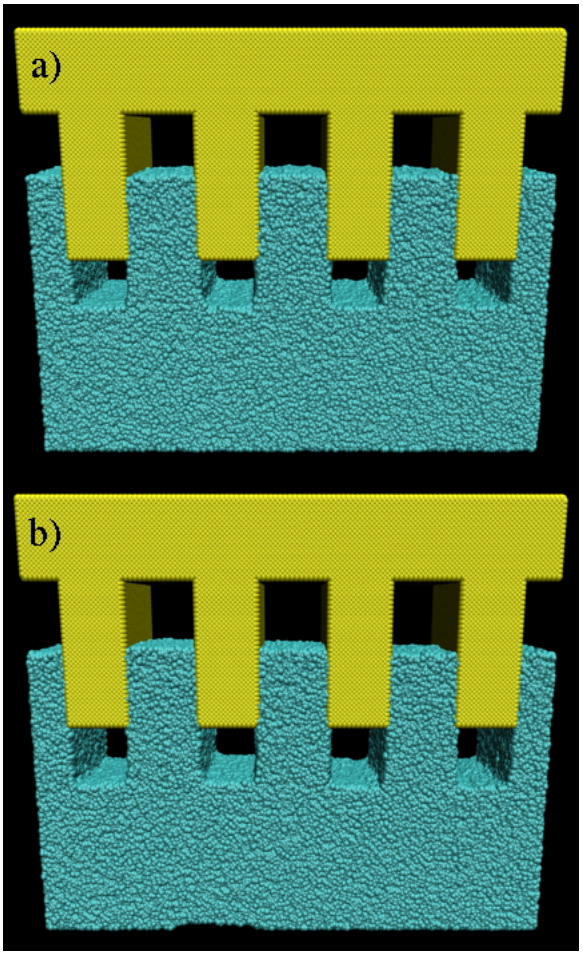

Figure 12: Snapshots of simulations showing removal of stamp with interaction strength of (a) ε_{12}=0.3 ε or (b) ε_{12}=0.6 ε for 1 crosslink for every 2 monomers.

Experimental SFIL systems generally coat the stamps with an anti-adhesion coating to lower the adhesion (Jung et al. 2005). We mimic these coatings by reducing the polymer/stamp interactions to $\varepsilon_{12}=0.3\varepsilon$. Upon such reduction we find that the stamps removes cleanly from the polymer melt with no failures and excellent feature retention. An example of such a system after partial stamp removal is shown in Fig. 12a.

Hot Embossing

Hot embossing is a nanomanufacturing technique that shares many steps with SFIL. In the hot embossing method, a rigid stamp is pressed into a polymer melt that is held above the glass transition temperature of the polymer, T_g. The entire system is then cooled below T_g to harden the polymer, and the stamp is then removed.

As with the SFIL simulations, we begin with a zero-stress stamp removal in which we delete the stamp atoms from the simulation box, and equilibrate the remaining polymer atoms at the lower temperature. In these cases we see excellent feature retention in all cases, and have determined that stress from stamp removal is the dominant cause of defects in the hot emboss process. We therefore proceed to simulations in which the rigid stamps are removed from the cooled polymer at fixed velocity.

For a weak polymer/wall interaction ($\varepsilon_{1w}=0.6\varepsilon$), we find complete detachment of the polymer from the wall upon "removal" of the stamp. With an increased interaction ($\varepsilon_{1w}=12.0\varepsilon$), we find failure within the polymer itself. The failure mode of the polymer is interesting to study in more detail. In all cases, separation occurs at the tops of the posts first, since the stress is concentrated at the sharp corners. The failure proceeds with alternating regions of lower density (i.e. the polymer pulls away from the stamp completely) and higher density (i.e. where the polymer is compressed agains the posts). The compressed regions remain in contact with the stamp, introducing frictional interactions during the removal process. We show examples of the defects generated for the three and four stamp systems in Fig. 13a and 13b respectively, where these alternating regions of higher and lower density can be seen.

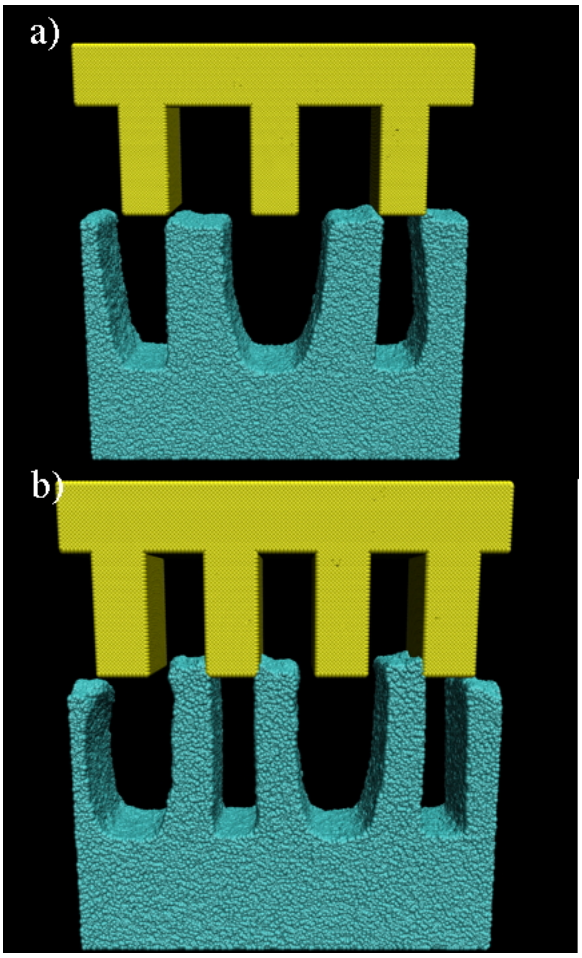

Figure 13: Snapshots of simulations of (a) three and (b) four stamps showing failures during removal after cooling to T=$0.3\varepsilon/k_B \sim 0.6T_g$.

We again mimic coated stamps by reducing the polymer/stamp interactions to $\varepsilon_{12}=0.3\varepsilon$. Upon such reduction we find that the stamps removes cleanly from the polymer melt with no failures and excellent feature retention.

In Fig. 14 we show the calculated pressure in the polymer during removal for both a coated ($\varepsilon_{12}=0.3\varepsilon$) and an uncoated ($\varepsilon_{12}=0.6\varepsilon$) stamp**.** During the initial phase of the removal process, the pressure increases sharply to a value of approximately -0.1 σ^3/ε where it reaches a plateau value. The pressure in the system with the coated stamp increases slightly linearly as the stamp slides smoothly out of the glassy polymer. In the uncoated system, however, there is no initial change in the pressure in the polymer until failure begins to occur at approximately 3 x 10^5 τ, where the pressure jumps sharply to a positive value before increasing linearly with time. The jump in the pressure in the uncoated system is coincident with the failure in the removal process, indicating that the remaining changes in the presure are due to the post-failure re-equilbration process.

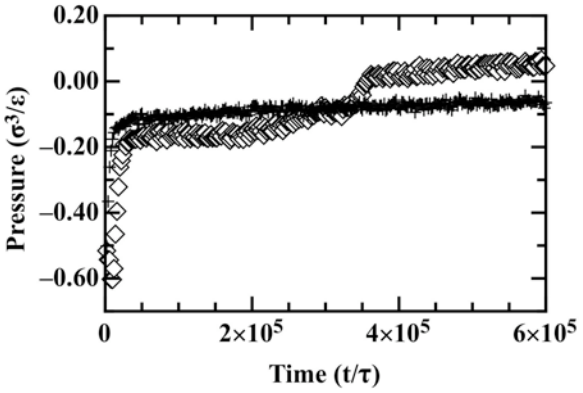

Figure 14: Pressure in the polymer during stamp removal for both a coated (+) and an uncoated (diamonds) stamp. The failure can be seen in the uncoated stamp beginning at approximately $3x10^5$ τ.

Discussion

During the insertion phase of both the SFIL and hot embossing processes we little evidence that this phase leads to defects, as long as the stamps are completely filled. However, unlike a large scale manufacturing process, it is quite easy for the stamps to be completely filled in our simulations because they are all of exactly equal heights, widths, and have no existing gas pressure to cause filling resistance. These are all features that are likely barriers to filling in commerical systems, and can be treated in a statistical fashion in larger-scale simulations to determine the ultimate effects. The fluid flow of the liquid polymer solution, including the frictional interactions with the stamp walls, could also be a major factor.

Here we have focused predominantly on the release step for our simulations.
In the SFIL simulations we find that the biggest barrier to defect-free removal is the interaction strength of the polymer with the bottom surface. If this is not large enough, the polymer debonds from the wall, leading to adhesive failure rather than stamp removal. With an increased interaction strength, we find that the stamp is generally pulled free without a major effect on the resulting features.

However, this is due in part to the excessive number of crosslinks we found were necessary to mainatin feature stability. With fewer crosslinks we found that features became rounded rather than retaining sharp corners on the time-scale simulated. It is indeed possible that lower numbers of crosslinks could lead to failures in the stamp removal process as well. It is important to note that the feature sizes we are investigating, while somewhat variable due to our coarse-grained simulation technique, tend to be on the smaller size scale of experimental features. It is conceivable, then, that lower numbers of crosslinks will lead to good feature retention for larger features, as curvature of sharp corners is less pronounced with larger surface areas.

We found removal of the stamp from the hot emboss simulations, in which the polymer was cooled below T_g to be much more defect-prone. While the zero-stress removal led to excellent feature retention, the simulations in which the stamp was physically pulled from the polymer led to much more difficulty. With a stronger interaction between the stamp and the polymer (e.g. a

contact angle near 90^{o}), we found that, assuming the interaction with the bottom wall is strong enough to prevent adhesive failure, the polymer fails through stamp adhesion. Only by reducing the polymer-stamp interaction to mimic a friction-reducing coating were we able to remove the stamp cleanly

The simulations we have presented are in essence two-dimensional due to the periodic boundary condition in one direction. In this sense, our simulations are most applicable to systems in which features with high aspect ratios are necessary, such as for creating wiring-like electrical contacts in microprocessors. We note that while the third dimension adds complexity to the phase space of the potential simulations, this is primarily through the introduction of more corners where stresses can concentrate. The effects of these corners can already be seen in the work we have presented, above. Other future directions to this work include variations in the feature heights, both at the tops and bottoms of the stamps.

Finally, we mention that in both SFIL and hot emboss experiments, rather than pulling with a force that is purely normal to the surface, stamp removal is generally achieved by a peeling process. This has the benefit of introducing a crack tip to avoid certain stress propagation through the polymer, but likely also introduces additional stress patterns to the removal that we have not considered here. Our work, then, can be considered a first approach to understanding the defects introduced by the removal of the stamp. The peeling process is another interesting area of future work, where both the angle and velocity of the mold removal could be investigated to determine their effects on defect propagation.

2.2 Embossing and Release model at continuum and machine scales

Our work has successfully addressed two of the main challenges faced when attempting a finite element analysis of key nano-scale manufacturing processing steps. First, we developed an approach for including adhesion and atomistic friction effects in detailed, feature-scale simulations. This is essential when feature size is on the scale of 10's to 100's of nanometers. This was accomplished by employing a novel adhesion/atomistic friction surface interaction model that is applicable when there is relatively weak bonding (i.e. van der Waals) between a polymer and the mold material (i.e., silicon). The formulation of this surface interaction model was motivated by friction force microscopy data for polymer surfaces. It is implemented within Sandia's Sierra/SM explicit finite element code via the code's contact algorithm. Secondly, we developed a hierarchical analysis technique that uses results from detailed, feature-scale, unit cell simulations. This was done by defining an effective "pattern traction-separation" relationship that is then used in simulations where the interface is modeled as flat (i.e., the pattern is not modeled explicitly). This type of hierarchical analysis should enable machine scale simulations aimed at determining tool performance. Furthermore, the hierarchical analysis drastically reduces CPU run time (e.g., by two orders of magnitude in our calculations).

The adhesion/atomistic friction surface interaction model will be discussed first. The application of this model to the embossing of a rubbery polymer (i.e., when above the polymer's glass transition temperature) and to the release of the glassy polymer (i.e., when below the polymer's

glass transition temperature) is discussed next. This is followed by a description of the hierarchical analysis technique. A brief summary concludes this section.

Adhesion/Atomistic Friction Surface Interaction Model

Adhesion and atomistic friction are expected to impact both embossing and release steps in a nanomanufacturing process when feature size is on the order of 10's to 100's of nanometers. Typically a relatively stiff mold (e.g., silicon, quartz) is used to imprint or hot emboss a polymer (e.g., photoresist etch barrier). Since the mold must be released from the hardened polymer without damaging the molded pattern, some means to weaken the adhesion between the mold and polymer is normally employed. Consequently, a surface interaction model that is applicable to relatively weak, van der Waals bonding between the polymer and the mold materials is required in nanomanufacturing simulations. The adhesion/atomistic friction surface interaction model used in this study was motivated by friction force microscopy measurements. In these scanning probe tests, friction (lateral) force is measured as a function of the applied normal force. Published work suggests that in at least some cases, a load-independent interfacial shear strength can be used to describe molecular-level friction (Burns, Houston et al. 1999; Carpick, Flater et al. 2004). Specifically,

$$F = \tau^* A(L) \tag{1}$$

where F is friction force, τ^* is a constant interfacial shear strength, and A is the contact area, which depends on applied normal load L. Data measured in several friction force microscopy studies of polymer coatings on hard substrates has been found to be consistent with Eq. 1. This includes friction data for a glass tip interacting with model lubricant silane and alkanethiol self-assembled monolayers (Burns, Houston et al. 1999), a silicon AFM tip sliding over an OTS (octadecyltrichlorosilane) self-assembled monolayer-coated silicon substrate (Reedy, Starr et al. 2005), and an AFM tip coated with a variety of self-assembled aromatic compounds sliding along a similarly coated substrate (Yang and Ruths 2009). These results suggest that the friction response defined by Eq. 1 is generally applicable to thin nanometer-scale polymer coatings. Such coatings can be formulated to perform as anti-adhesion coatings. It is also possible that Eq. 1 is generally applicable to typical polymer/mold interactions since atomistic frictional interaction is a surface, not bulk property.

The adhesion/atomistic friction (Ad/AF) surface interaction model used in this study is based on atomistic frictional behavior as described by Eq. 1. This model has two elements. Adhesion is defined by a traction–separation (*T-U*) relationship, where σ is the normal traction and δ_n is the normal interfacial separation (Fig. 15a). The two key parameters defining this *T-U* relationship are the interfacial strength σ^* and the work of adhesion Γ. This study uses a simple triangular *T-U* relationship with a steep initial portion (defined by λ, with a typical value of 0.05) and a finite cutoff distance for the adhesive force δ_n^c (typical value of one-nm). For a triangular *T-U* relationship, the work of adhesion Γ, which equals the area under the *T-U* curve, has a value of $\sigma^* \delta_n^c/2$. The work of adhesion for a weakly bonded interface (i.e., no chemical bonding, only van der Waals forces) can be relatively low. For example, Γ for an epoxy/OTS interface has been measured to be ~0.05 J/m^2 (Kent, Yim et al. 2001). Accordingly, if Γ = 0.05 J/m^2 and δ_n^c = 1 nm,

the interfacial strength σ^* = 100 MPa for a triangular *T-U* relationship. A more complicated *T-U* relationship could be used if needed, but that was not thought to be necessary in the present study. Since the *T-U* relationship includes a length scale, calculated results are mesh-independent provided that the mesh is fine enough to resolve the open gap across which adhesion forces act. Note that the finite elements contract algorithm is used to prevent normal interpenetration.

The second element of the Ad/AF model defines the nature of interfacial shear stress τ in a way that is consistent with Eq. 1 (Fig. 15b). Here it is assumed that there is no frictional interaction between opposing materials when $\delta_n > \lambda\delta_n^c$ (in this study the typical value of $\lambda\delta_n^c$ is 0.05 nm, a length scale consistent with atomistic roughness). In other words, friction does not act across an open gap with $\delta_n > \lambda\delta_n^c$, and consequently $\tau = 0$ when this condition applies. Friction acts only when $\delta_n < \lambda\delta_n^c$. When friction acts, the opposing materials are tied together if $|\tau| < \tau^*$, while slip occurs when $|\tau| = \tau^*$, with τ^* opposing interfacial slip (note, τ^* is a pressure independent material constant). One virtue of the Ad/AF model is that the most important of the parameters defining the model (Γ and τ^*) can be deduced from friction force microscopy measurements.

The analysis was performed using Sandia National Laboratories' Sierra/SM explicit, transient dynamics finite element code. In brief, an explicit dynamics finite element analysis uses a central difference time integrator to advance the solution from an initial state using time steps that satisfy a stability criterion. Explicit dynamics finite element codes are well suited for analyzing large deformations with complex contact conditions, discontinuous crack growth, etc. The Ad/AF model is implemented in the Sierra/SM explicit finite element code via an extension to its contact algorithm. As implemented, the Ad/AF finite element analysis implicitly assumes that the interface is locally flat as compared to the range of the adhesive force with gap distance defined by the normal distance between a node and the opposing surface. Note that the adhesion forces are calculated in the current, deformed geometry. Thus, opposing materials can undergo large relative translations and still interact if they are within the range of adhesion forces. For example, the Ad/AF model allows separation and reattachment after large relative tangential displacements. In all calculations reported here, the external loads are applied sufficiently slowly that the external loading is quasistatic. Nevertheless, an interfacial separation can still propagate dynamically once initiated if the energy release rate exceeds the interfacial resistance to separation. As reported previously, the accuracy of the adhesion portion of Ad/AF model has been verified by simulating a problem where JKR adhesion analysis should apply (Reedy 2006).

Embossing

A series of illustrative simulations was performed to explore the effect of adhesion and atomistic friction on nano-embossing. To avoid geometric complexity, a 2-D, plane strain geometry that corresponds to a pattern composed of identical, parallel channels (or conversely teeth) was analyzed. The polymer material is heated well above its glass transition temperature and is in a rubbery state while it is embossed. Hence, the polymer is modeled as a compressible, Moody-Rivlin rubber (Aklonis and MacKnight 1983; Scherzinger and Hammerand 2007) with a nominal, small strain Young's modulus of one MPa and a Poisson's ratio of 0.499 (used Moony-Rivlin model parameters C_{10}=0.1333 MPa and C_{01}=0.0333 MPa). A unit cell analysis is

applicable to the parallel-channel geometry. Figure 16 shows the geometry of the embossing problem that was analyzed (the calculations take advantage of translational symmetry). Since the mold material is much stiffer than the rubbery polymer, it can be considered rigid. For this reason only elements that define the mold contour (interface) are included in the mesh. The mold cavity is nominally 100 nm wide by 50 nm high with a ~12^o wall-taper and 5-nm radii at wall transition points. The bottom edge of the polymer layer is fixed to model attachment to a relatively rigid substrate.

Calculations were performed for three cases: a) simple contact (Γ=0.0 J/m^2 and τ*=0.0 MPa), b) adhesion only (Γ=0.05 J/m^2 and τ*=0.0 MPa), and c) adhesion and atomistic friction (Γ=0.05 J/m^2 and τ*=10.0 MPa). The range of the adhesion force in these calculations is δ_n^c = 1 nm. Figure 17a-c shows the calculated deformed geometry at first contact of the polymer with the top surface of the mold. The downward mold displacement *U* and the applied compression *C* to fill the mold (defined as the applied compressive load at the time when the mold cavity is completely filled/base area) are displayed on each of the figures. The addition of adhesion causes the polymer to jump into contact once it is within range of the adhesion force and helps pull the polymer into the corner. This yields a 30% lower calculated value of *C* at the same value of *U* (compare cases a and b). The further addition of atomistic friction results in an even greater effect on the polymer deformation (compare cases b and c). While adhesion pulls the polymer towards the mold, atomistic friction retards fill by preventing slip. The further addition of atomistic friction increases the calculated *C* from 1.1 MPa to 3.8 MPa, an increase of 350%.

The sensitivity of the embossing simulations to the values of the parameters Γ and τ* that govern the strength of polymer/mold interactions was also investigated. The adhesion only analysis was rerun but with Γ reduced from 0.05 to 0.005 J/m^2 (i.e., σ* =10 instead of 100 MPa, while maintaining δ_c=1 nm). There was no discernable difference generated by reducing Γ. The rubbery polymer is so compliant and the polymer stresses are so low prior to the time when the mold is completely filled that even an interfacial strength of 10 MPa will cause the polymer to jump into contact. The adhesion with atomistic friction simulations were also rerun with varying values of τ*. Figure 18 shows that the applied compression to fill the mold is altered even when τ* = 1 MPa. Results for τ* = 5 and 10 MPa are essentially identical indicating that the polymer is now completely stuck to the mold surface (i.e., no slip) and further increase in τ* will not affect the calculated response. Note that the applied compressive load increases rapidly once the mold is completely filled since the deformation is then determined by the polymer's much higher bulk modulus.

The illustrative results presented here clearly show that adhesion and atomistic friction can have a significant effect on the nano-embossing. The polymer deformation pattern is altered and a significantly higher load is required to push the last portion of polymer material into the corner of the mold. These results suggest that atomistic friction may make it increasingly difficult to push a rubbery polymer into the top corner of feature as feature height increases. These results also suggest that high accuracy measurements of τ* may not be necessary. Even a small value of τ* sticks a rubbery polymer to the mold wall, and increasing that value has no effect.

Release

The key factors affecting the release of the polymer from a mold were investigated by performing a series of illustrative calculations where variations from a baseline configuration were examined. The baseline configuration has a 2-D, plane strain geometry that is similar to that used in the embossing study. As before, the pattern is composed of identical, parallel channels (or conversely teeth) and a unit cell analysis is applicable. Figure 19 shows the unit cell geometry used in release calculations (the calculations take advantage of translational symmetry). The mold cavity is nominally 100 nm wide by 100 nm high with a ~12^o wall-taper and 5-nm radii at wall transition points. The true-to-nominal interfacial area A_r equals 1.76 (i.e., the ratio of the actual interfacial area to the base area). The bottom edge of the polymer layer is fixed to model attachment to a relatively rigid substrate. The characteristic length of the finite elements along the interface is 2.5 nm.

The polymer is cooled below its glass transition temperature T_g after embossing and is in a glassy state prior to release. The glassy polymer is modeled as a linear elastic material with a Young's modulus E of 1.0 GPa, a Poisson's ratio ν of 0.4, and a mass density ρ of 1.0 g/cm^3. Furthermore, a linear shrinkage ε_o of 1% is assumed to occur prior to release (e.g., shrinkage generated by cooling below the polymer's T_g after embossing). The mold is also modeled as a linear elastic material with properties similar to silicon (E=160 GPa, ν=0.23, and ρ of 2.3 g/cm^3). Even though the glassy polymer's modulus is 1000 times greater than that of the polymer's small strain rubbery Young's modulus, the glassy polymer's modulus is still only ~0.6% of that of the mold. One anticipates that the mold can be considered rigid and that its presence simply defines the polymer/mold interface (this will be shown to be true below). Note that the actual mold would actually be much thicker (mm's) and pattern would be quite small compare to mold thickness. Since the mold is essentially rigid, its thickness can be truncated to minimize the size of the problem analyzed.

The goal of this effort is to simulate the entire separation process using the Ad/AF surface interaction model for the polymer-mold interface. For the baseline configuration, the values of the key interface properties are Γ= 0.05 J/m^2 and $\sigma^*= 2\tau^*$= 100 MPa with λ= 0.05 and δ_c=1 nm. In the baseline calculation, the polymer first undergoes a 1% linear shrinkage followed by the uniform displacement of the upper mold boundary to effect mold release. The calculations included a relatively low level of mass proportional damping (Clough and Penzien 1975) to damp out vibrations (stress waves) generated by dynamic separation (used a mass proportional Rayleigh damping coefficient m_d = 10 ns^{-1}). This level of damping has no appreciable effect on the applied loads and the loading can be considered to be quasistatic (top edge of mold is displaced with a velocity of 0.1 nm/ns).

The baseline simulation (BL) revealed a complex release process that includes multiple dynamic separation and arrest events as well as adhesive reattachment. In the following description refer to the positions labeled in Fig. 20, and note that mold displacement U is the applied mold displacement; it does not include mold displacement induced by the initial polymer shrinkage. The mold is not restrained during the initial 1% linear polymer shrinkage step. Consequently, a residual compression is generated in the thinnest, most highly constrained portion of the polymer (i.e., under the silicon tooth). The mold is then displaced upward until U=1.94 nm. At this

displacement, dynamic interfacial separation initiates at the location of highest polymer constraint (pt. 1) and then arrests once turning the corner (pt. 2). After a further mold displacement (U=2.59 nm), dynamic interfacial separation re-initiates and the entire interface separates (separation grows from pt. 2 to pt. 3). A gap immediately opens between the top of the mold and the top of the polymer feature and the feature translates several nanometers downward relative to the mold. The gap at point 2 is now within the range of the adhesion forces and the polymer reattaches to the mold and adhesion closes up the gap between polymer and mold from point 2 to point 4 (U=2.68 nm). At this time, only the tapered edges of the mold and polymer are attached. As the mold continues to displace upward, the parallel, tapered walls will tend to separate, and final dynamic separation imitates at point 4 (U=4.94 nm).

An effective traction-separation relationship for the patterned interface (Pattern T-U relationship) can be defined where the traction is the total applied normal force/nominal bonded interfacial area (i.e., mold's base area) and the displacement is the mold's applied edge displacement. The Pattern T-U describes the overall effect of the patterned polymer layer and provides a reduced representation of the separation process. Additionally, an effective interfacial toughness Γ_e can be defined as the area under the Pattern T-U curve. Figure 21 plots the Pattern T-U relationship for the BL calculation. Also plotted is the intrinsic T-U relationship that defines the adhesion relationship used in the unit cell calculation. The complex interfacial separation process translates the intrinsic T-U into a Pattern T-U with a significantly different shape. The vertical load drops correspond to the labeled dynamic separation events. Note that even though the applied loading is quasistatic, the interfaces can separate dynamically to create kinetic energy (the kinetic energy is dissipated by mass proportional damping in the calculations). If Γ_e depended solely on the pattern's real interfacial area, then its value would equal $A_r\Gamma$, where A_r is the real-to-nominal interfacial area. However, $\Gamma_e/(A_r\Gamma)$ equals one only if separation occurs quasistatically and simply involves opening a normal gap greater than the range of adhesive forces between all surfaces (i.e., adhesion forces are the only forces resisting opening). This further assumes that there is no frictional dissipation during separation and that there are no initial residual stresses present since such stresses can affect the energy released during separation. Noting these restrictions, $\Gamma_e/(A_r\Gamma)$ is still a useful nondimensionalization for comparing results . For the BL calculation, $\Gamma_e/(A_r\Gamma) = 1.92$. If one neglects reattachment, $\Gamma_e/(A_r\Gamma) = 1.27$.

Convergence of the BL calculation with element size was assessed by repeating the calculation using a refined mesh. The characteristic length of elements along the interface was reduced from 2.5 nn to 1.25 nm. Figure 22 shows that even though the failure process is quite complex, the calculated Pattern T-U relationship is unchanged with mesh refinement. A calculation was also performed to assess if mold geometry affects the calculated Pattern T-U. In this calculation, the thickness of the top of the mold was increased from the BL value of 25 nm to 50 nm (Fig. 19). This change in the thickness of the thinnest portion of the mold has no affect on the calculated Pattern T-U (Fig. 22). The mold is essentially rigid and its deformations do not influence polymer response and interfacial separation.

The Pattern T-U relationship will depend on feature geometry, interface and bulk material properties, polymer shrinkage, etc. These dependencies can be expressed in terms of nondimensional parameters. The primary parameters that define the BL problem include

interfacial properties σ^*, Γ, λ, and τ^*, polymer properties ρ, E, ν, ε_o, geometric parameters that will be referred to generically as L_i's with L_1 taken to equal the feature height, and mass damping m_d (units of ns^{-1}). Mold properties are not considered since the mold is essentially rigid. The nondimensional parameters will be expressed in terms of Γ, σ^*, and ρ (other choices are possible, this is simply a convenient choice). With this choice, length ~ Γ/σ^*, force ~ Γ^2/σ^*, and time ~ $(\Gamma/\sigma^*)/(E/\rho)^{1/2}$. Accordingly, the effective toughness can be expressed as

$$\Gamma_e/\Gamma = f\left(\varepsilon_o, \frac{\tau^*}{\sigma^*}, \frac{\sigma^*}{E}, \frac{m_d\Gamma}{\sigma^*(E/\rho)^{1/2}}, \frac{L_1}{(\Gamma/\sigma^*)}, \frac{L_i}{L_1}, \nu_m, \lambda\right) \tag{2}$$

The dependence of Γ_e/Γ on the nondimensional parameters defined in Eq. 2 will be investigated through variations the BL problem (i.e., selectively vary one parameter in the baseline problem while keeping all others fixed).

First consider the affect of polymer shrinkage ε_o on the Pattern *T-U* relationship. Figure 23 contrasts results for ε_o = 0.00, 0.01 (BL), and 0.02. The level of polymer shrinkage has a significant effect. The initial residual compressive stress in the most highly constrained portion of the polymer (i.e., under the silicon tooth) increases with e_o. Consequently, the applied traction required to initiate interfacial separation, which occurs where the polymer is most highly constrained, also increases with e_o (i.e., a higher applied tensile load must be applied when the residual compression is higher). When e_o=0.02, interfacial separation is rapid and complete once it is initiated (no arrest) and there is little reattachment. As the traction at initiation increases, the energy available to dynamically separate the interface also increases. Furthermore, a higher value of e_o results in a larger gap between the mold and polymer feature after separation, reducing the likelihood of adhesion-induced reattachment. When there is no polymer shrinkage (e_o=0.0), a significantly large mold displacement is required to ultimately release the polymer form the mold. Calculated values of $\Gamma_e/(A_r\Gamma)$ equal 3.4, 1.9, and 1.4 for ε_o = 0.00, 0.01 (BL), and 0.02, respectively.

Next consider how the Pattern *T-U* relationship depends on τ^*/σ^*. In these calculations τ^* was varied while keeping σ^* fixed at 100 MPa. Figure 24 shows that the initial portion of the calculated Pattern *T-U* relationship is quite similar for all $\tau^*/\sigma^* > 0.0$, and differs markedly only after adhesion-induce reattachment. This suggests that interfacial slippage plays a limited role during the separation process prior to reattachment. Furthermore, the Pattern *T-U* relationships are essentially identical when $\tau^*/\sigma^* \geq 0.5$. A τ^*/σ^* value of 0.5 is sufficiently high to prevent slipping after reattachment and any further increase in τ^*/σ^* has no additional effect. The relative insensitivity of results to the value of τ^*/σ^* is encouraging since its value is not easily determined. Calculated values of $\Gamma_e/(A_r\Gamma)$ equal 1.7, 1.9, 2.0, 1.9 and 1.9 for τ^*/σ^* = 0.00, 0.10, 0.25, 0.50 (BL), and 1.00, respectively.

The parameter σ^*/E also has a significant effect on the calculated pattern *T-U* relationship (Fig. 25). In these calculations the polymer Young's modulus E was varied while keeping σ^* fixed at 100 MPa. As σ^*/E increases (i.e., E decreases), the polymer becomes more compliant and the

shrinkage induced residual compression in the thinnest, most highly constrained portion of the polymer (i.e., under the silicon tooth) is decreased. Consequently, the applied traction required to overcome the initial residual compression and initiate interfacial separation also decreases with increasing σ^*/E. When $\sigma^*/E = 0.20$ there is no adhesion-induced reattachment; once fully separated, the gap between the mold and polymer increases with polymer compliance and can become large compared to the range of adhesion forces. Calculated values of $\Gamma_e/(A_r\Gamma)$ equal 1.4, 1.9, and 2.0 for $\sigma^*/E = 0.05$, 0.10 (BL), and 0.20, respectively.

The same level of mass proportional mass damping was applied in all calculations discussed to this point (used a mass proportional Rayleigh damping coefficient $m_d = 10\ \text{ns}^{-1}$). A relatively low level of mass damping was included in the calculations to damp out vibrations (stress waves) generated by dynamic separation. In reality, such vibrations will be damped out by energy dissipation mechanism such as polymer viscoelasticity. Since the present analysis assumes fully elastic response, such dissipation is not included. Mass proportional damping is simply a convenient computational approach for applying damping. Unlike the other BL parameters, m_d is not a simple material or geometric parameter, but rather a structural parameter that influences calculated response. Figure 26a compares the calculated Pattern *T*-*U* relationship for the BL level of mass proportional damping with that when there is no damping. When there is no damping, the calculated *T*-*U* curve exhibits high frequency oscillations after dynamic interfacial separation (vertical drops in the *T*-*U* relationship). Nevertheless, the no-damping and BL cases have the same basic form and differ most significantly only at final separation after reattachment. Figure 26b compares results for normalized m_d values that are half and double the BL value. Mass proportional damping mostly influences how rapidly the final separation process occurs and only has a modest effect on the calculated Pattern *T*-*U*. The calculated values of $\Gamma_e/(A_r\Gamma)$ equal 1.90, 1.92 (BL), and 2.02 for $(m_d\Gamma/\sigma^*)/(E/\rho)^{1/2} = 0.0025$, 0.005, and 0.0100.

Finally, the effect of intrinsic toughness Γ and length scale L_1 was considered through variations in the parameter $L_1/(\Gamma/\sigma^*)$. First consider the BL problem, but vary Γ by varying δ_n^c with σ^* fixed (Fig. 15a). Note that L_1 is equal to the BL feature height (i.e., 100 nm, Fig. 19). Figure 27 show that as the toughness increases from Γ=0.025 0 to 0.100 J/m^2 (when $L_1/(\Gamma/\sigma^*)$decrease from 400 to 100), the effective toughness increases. The range of the surface interaction increases with Γ, and consequently the degree of dissipation due to adhesion-induced reattachment increases. Note that $(m_d\Gamma/\sigma^*)/(E/\rho)^{1/2}$ was not held constant in these calculations, but varied from 0.0025 to 0.0100; the same range of values that was shown to have only a modest effect on the calculated Pattern *T*-*U* relationship (Fig. 26b). The normalized effective toughness does not vary as much as one might expect. $\Gamma_e/(A_r\Gamma)$ equal 1.91, 1.92 (BL), and 2.32 for $L_1/(\Gamma/\sigma^*)$ equal 400, 200 (BL), and 100, respectively. Instead of varying Γ in the nondimensional parameter $L_1/(\Gamma/\sigma^*)$, one could also vary L_1 (keeping the all other geometric parameters L_i/L fixed). For instance, the patterned *T*-*U* relationship (with *U* normalized by δ_n^c) should be identical to the BL problem when both L_1 and Γ are doubled. Figure 28 shows this to be true for both the standard and a refined mesh where the characteristic length of elements along the interface was reduced from 2.50 nn to 1.25 nm. In these calculations $(m_d\Gamma/\sigma^*)/(E/\rho)^{1/2}$ was held fixed with a value of 0.005.

Hierarchical Analysis

The potential use of the Pattern *T-U* relationship in a hierarchical analysis was investigated. The proposed approach uses an effective Pattern *T-U* relationship, which is determined by a unit cell analysis, in a higher level model with a geometrically smooth interface. It is postulated that the Pattern *T-U* relationship provides a sufficiently complete representation of the effect of nm-scale geometry on interfacial separation to fully define the release process at a higher length scale. Such an approach would enable finite element analysis on the wafer scale and could include the release of large areas containing many different types and sizes of molded features. A hierarchical analysis of this type should be applicable when unit cell deformations do not depend on mold deformations and wafer-wide displacement gradients are small over distances comparable to the unit cell length scale. Fortunately, these requirements are likely met in typical nanomanufacturing release processes.

The feasibility of the proposed hierarchical analysis methodology was assessed by comparing results from an analysis that explicitly models the pattern with those from an analysis that replaces the pattern with a Pattern *T-U* relationship. A simple, mold geometry that has parallel channels with a rectangular cross-section was analyzed. Figure 29a shows the mesh used in the calculation that explicitly models a 1000-nm high mold with 60 channels, while Figure29b shows the pattern's unit cell geometry (a relatively simple pattern geometry with a coarse mesh is used to facilitate the 60-feature simulations). The channels are 50 nm wide by 50 nm high with a 25 nm base layer. The glassy polymer is modeled as a linear elastic material with an E = 1.0 GPa, $\nu = 0.4$, $\rho = 1.0$ g/cm^3, and an ε_o of 0.01 prior to release. The mold is also modeled as a linear elastic material with properties similar to silicon (E=160 GPa, ν=0.23, and $\rho = 2.3$ g/cm^3). The Ad/AF model parameters are $\Gamma = 0.05$ J/m^2, $\sigma^* = 100$ MPa, τ^*=0.0 (τ^* was set to zero since the side-walls are vertical and do not separate with increasing mold displacement as would a mold with tapered walls). Figure 30 plots the calculated Pattern *T-U* relationship as determined from the unit cell analysis. There are two dynamic separation events; first the polymer separations where the polymer is most highly confined followed by separation along the top edge of the feature.

On the wafer-scale, one would not expect that all features will separate simultaneously (there will be some long wavelength variations in the wafer surface and the mold edge displacement will not be absolutely uniform). Rather one would expect a separation front to run across the mold in a crack-like manner. For this reason, the explicitly modeled, 60-channel mold was subjected to a very small, peel-like loading perturbation by slightly rotating the mold's upper edge before pulling upwards. Specifically, the polymer was first subjected to a 1% linear shrinkage. Next a displacement gradient ΔU was established by rotating mold's 6000 nm top edge such that the left-had-side (LHS) of the mold was displaced 0.8 nm upward while the right-hand-side (RHS) remained fixed. The top edge was then uniformly displaced while maintaining ΔU =0.8 nm (i.e., gave edge nodes a constant upward velocity).

The finite element results for the explicitly modeled pattern indicate that the separation process propagates from left to right in two stages. Initially only interfacial segments at the tip of the silicon teeth separate (see picture 2 in Fig.30) while the interfacial segments at the top of the polymer feature remain intact. One after another, teeth-tip interfacial separations initiate, forming

a system of collinear interfacial segments that propagate towards the mold's RHS. However, prior to reaching the mold's RHS, complete interfacial separation at the mold's LHS initiates. This final separation front propagates steadily from left to right as interfacial segments along the top of the feature separate from the mold (see picture 3 in Fig. 30). A hierarchical analysis using the Pattern T-U relationship shown in Fig. 30 was also performed. In this analysis, the interface was modeled as flat and the characteristic element size was 10 times larger than that used in the analysis where the pattern was modeled explicitly. As consequence of the smaller number of elements and the larger stable time step, the flat interface hierarchical analysis runs 300 times faster. Figure 31 plots the calculated average applied traction vs. the average applied displacement for both the explicitly modeled pattern and hierarchical analyses. The feasibility of the proposed hierarchical analysis is clearly demonstrated. Obviously more work is needed to establish the limits of this approach.

Although results reported here are focused on 2-D, parallel channel geometries, the applicability of the hierarchical approach to more complex, 3-D pillar geometries was also considered. The 3-D analyses use the same Ad/AF model and parameters, and use similar geometric features (such as the polymer base thickness and surface feature dimensions) and material properties as the 2-D parallel channel hierarchical analysis. An array of cubic pillars was analyzed, where the ratio of the actual interfacial area to base area (A_r) equals 2 (Fig.32). For the applied loadings considered here, symmetry conditions can be applied to reduce the problem to a single row of the pillar cells (Fig. 33). Displacements normal to the surface of the base layer's sides and bottom are constrained to zero.

As noted in the 2-D analyses the mold is extremely stiff relative to the polymer. For the case of a uniform displacement applied to the top of the mold, the mold experiences uniform uniaxial strain except near the patterned interface. To minimize the run time of the calculations, a smaller mold thickness was used in the 3D calculations (275 nm) as compared to that used in the 2D calculations (950 nm). Furthermore, to simplify model construction, the basic repeated unit of the 20 feature model was used as the unit cell geometry (Figure 34a). The drawback of using this unit cell geometry is that the compliance of the relatively thick mold does have a small effect on the overall calculated displacement (though the interfacial separation process is unaffected). This additional mold displacement must be "subtracted" from the specimen response since the effective Pattern *T-U* relationship includes only the displacement generated by the patterned polymer and the interfacial separation process (the mold in the unit cell used in the 2D analysis was sufficiently thin that its deformation had no noticeable effect on calculated displacements, Fig. 22). This correction is in the same spirit as was done by Cox and Yu (Cox and Yu 1999).

Figure 35 shows the calculated *T-U* relationship as based on the average traction and the prescribed displacement on the top of the unit cell (labeled as unit cell *T-U*). This is the response that is to be replicated using the Pattern *T-U* relationship in conjunction with a model with a flat interface (Fig. 34b). The flat interface model is composed of a 275 nm-thick block corresponding to the silicon mold and a 25 nm-thick silicon base representing the essentially rigid substrate to which the relatively compliant polymer is attached. The mold deformation u_{mold} in the flat interface model can be simply determined by noting that a condition of uniaxial strain applies

$$u_{mold} = (L / E_u)T \quad \text{where } E_u = \frac{E(1-\nu)}{(1-2\nu)(1+\nu)} \tag{3}$$

where E_u is the uniaxial strain modulus, L ~ specimen thickness (300 nm), and T is the average applied traction. Consequently,

$$u_{pattern} = u_{applied} - u_{mold} \tag{4}$$

Figure 35 plots the raw unit cell *T-U* relationship (which includes the mold displacement) as well as the Pattern *T-U* relationship as determined using Eq. 4 (labeled as "inferred interface T-U"). Figure 36 shows the *T-U* relationship as determined by the unit cell analysis (inferred interface response), a piece-wise linear representation, which will be taken to be the Pattern *T-U* relationship, and the intrinsic *T-U* response used in the unit cell analysis. Note that the noisy transitional response from u ~ 1.3 nm to 1.5 nm, is a numerical artifact that can be eliminated by mesh refinement, and as such is not included in the effective Pattern *T-U* interface model. As was the case for the 2-D analyses, the Pattern *T-U* relationship for the flat interface model differs significantly with the intrinsic *T-U* relationship used in the unit cell analysis.

The Pattern T-U model had an equivalent fracture energy (Γ_e) of 0.063 J/m^2, and the value of $\Gamma_e/(A_r\Gamma)$ is 0.63. For most cases with tapered sidewalls, this ratio is expected to be greater than one, but here the sidewalls of the cubic pillar are not tapered. As such the sidewalls do not separate in a way that dissipates energy by creating new surfaces (i.e., sidewalls do not separate by overcoming adhesion forces). The area that does undergo normal separation is equal to the base area, so in this case Γ_e/Γ is a useful measure for gauging the relative contribution of dynamic separation events. The value of Γ_e/Γ is 1.26, which indicates that dynamic separation increases the effective energy of separation.* Applying the Pattern T-U in conjunction with the flat interface unit cell model reproduces the unit cell analysis that explicitly modeled the patterned interface (Fig. 38).

Returning to the 20-pillar strip model, we consider a loading similar to that used in the 2-D hierarchical analysis. After shrinkage, the mold is lifted at one end followed by uniform displacement of the whole mold. As before, the motivation is to provide a slight displacement gradient so that a crack-like separation front propagates from one end to the other. To accomplish this, a displacement gradient ΔU was established over the top edge of the 20-pillar strip (Fig. 23a) by rotating mold's 2000 nm top edge such that the LHS of the mold was displaced 1.0 nm upward while the RHS remained fixed. The top edge was then uniformly displaced while maintaining ΔU =1.0 nm. As in the 2-D case, initially only those interfacial regions where the polymer is most highly constrained separate, however, prior to reaching the mold's RHS, complete interfacial separation at the mold's LHS initiates and this final separation front propagates steadily from left to right. Figure 39 shows the calculated average traction versus average mold displacement for the analysis that explicitly models the pattern as well as

* The dynamic separation effect was observed in preliminary 3-D analyses that used a different unit cell geometry (cylindrical pillar) and interface model. In one case the analysis was conducted using Sierra/SM with explicit integration of the dynamic response, while in the other case the analysis was conducted as a quasi-static problem with an arc-length method that adjusts the traction to follow the snap-back behavior. Figure 23 compares the two analyses. The quasi-static analysis reflects a smaller effective energy of separation because it does not include the kinetic energy loss, but in reality this dynamic response cannot be avoided, and thus it must be included in the effective energy of separation.

that for the flat interface hierarchical analysis that uses the Pattern T-U relationship. The hierarchical analysis reproduces the response determined by the analysis with the explicitly modeled patterned interface.

One further extension of the hierarchical analysis is envisioned. In the illustrative problem presented here, solid elements were used in the flat interface analysis. That is probably impractical in a wafer-scale analysis. Instead, one could replace the solid elements by shell elements. An analysis similar to that previously used to model discrete delaminations within thin composite structures could be used (Reedy, Mello et al. 1997). In that analysis a DLAM element constrains two stacked shell elements to act as a single shell element until the stacked elements separate (delaminate) with separation defined by a *T-U* relationship. The top shell would correspond to the mold while the bottom shell would correspond to the substrate to which the molded polymer is bonded. The Pattern *T-U* would connect the two shell elements and define how they separate. If a wafer contains multiple sectors, each with a different type of pattern, each sector would use the Pattern *T-U* relationship that is appropriate for that sector.

Finally note that while all of the results presented here have been for the case where the pattern is composed of a single repeated feature, more complex patterns could be analyzed. For example, a pattern might be composed of repeated blocks, where each block contains multiple features (e.g., pillars of different heights, spacing, etc.). This case could be treated by performing an analysis where the unit cell is defined by the repeated block. Alternately, the effective T-U relationship for each feature in the block could be determined and the area-weighted average of these individual *T-U* relationships would then define the Pattern *T-U* relationship.

Summary

The present study focused on developing finite element-based techniques for nanoscale simulations of the embossing of a rubbery polymer (i.e., when above the polymer's glass transition temperature) and the subsequent release of the glassy polymer (i.e., when below the polymer's glass transition temperature). A novel adhesion/atomistic friction surface interaction model, motivated by friction force microscopy data, was used to perform the simulations. Our finite element simulations indicate that even low levels of adhesion and atomistic friction have a significant effect on these key nano-manufacturing processes. As the mold is pushed into a rubbery polymer during embossing, adhesion pulls the polymer towards the mold while atomistic friction retards fill by preventing slip. Simulations of the release step show that the interface between the mold and the now hardened, glassy polymer does not unzip in a continuous, quasistatic manner. Instead, there is a complex failure sequence that can include multiple dynamic separation and arrest events as well as adhesive reattachment. Finally, the feasibility of a hierarchical analysis that represents the nm-scale pattern by an effective Pattern *T-U* relationship is demonstrated. The Pattern *T-U* relationship is determined by analyzing a representative unit cell of the pattern. Although results reported here are focused on 2-D, parallel channel geometries, a limited number of simulations for pillar geometries showed similar behavior.

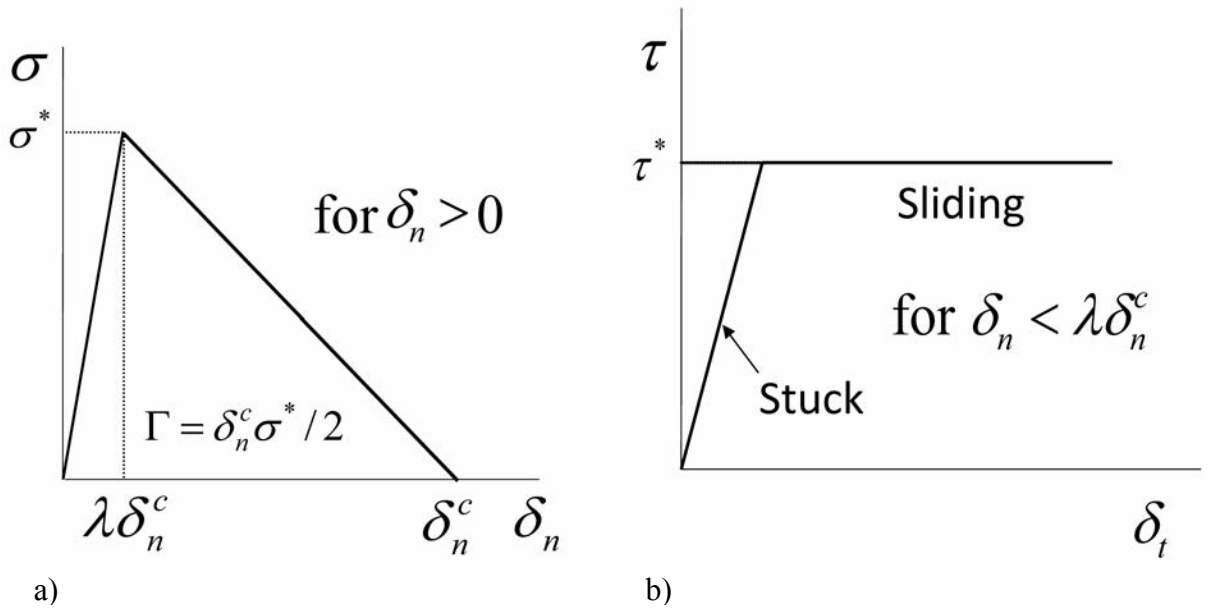

Figure 15. a) adhesion and b) atomisitc friciton portions of Ad/AF surface interaction model.

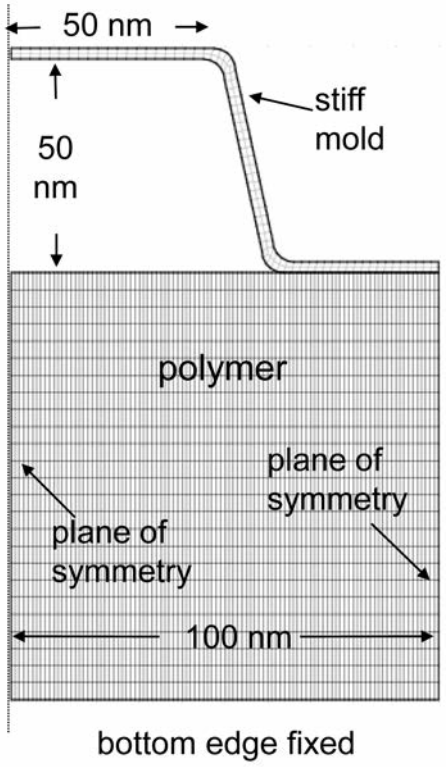

Figure 16. Unit cell geometry used in the embossing simulations.

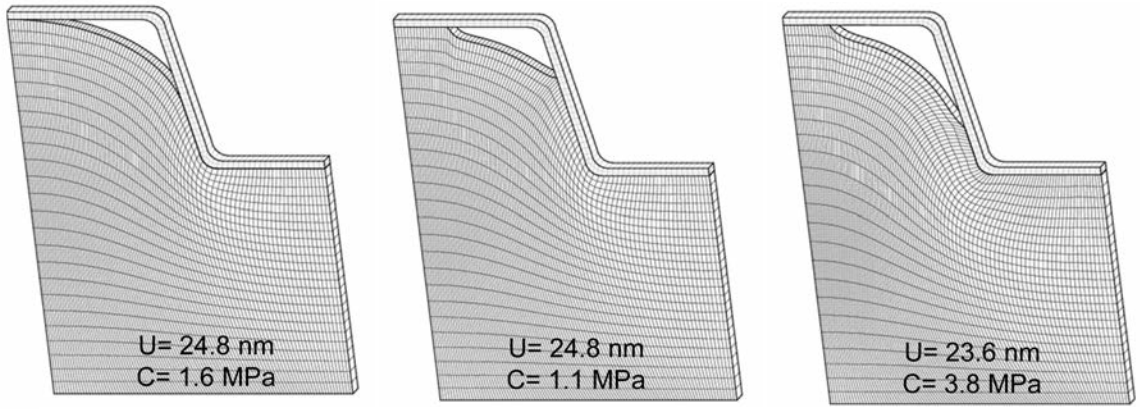

Figure 17. Calculated deformed geometry at first contact of the polymer with the top surface of the mold. a) no adhesion or atomistic friction, b) adhesion but no atomistic friction, and c) adhesion and atomistic friction.

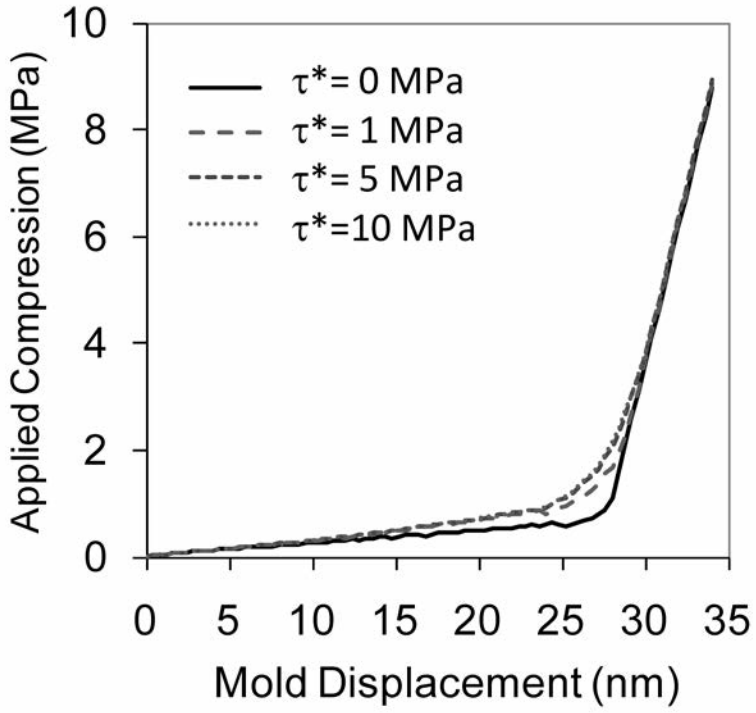

Figure 18. Applied compression versus mold displacement for different levels of atomistic friction.

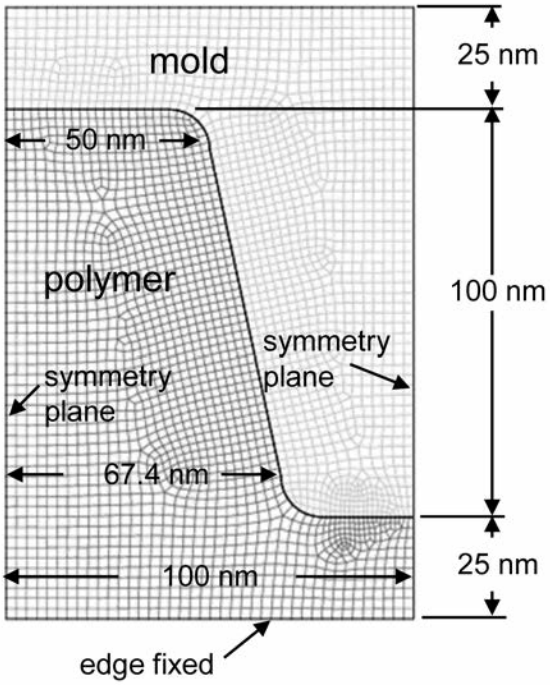

Figure 19. Unit cell geometry used in the release calculations.

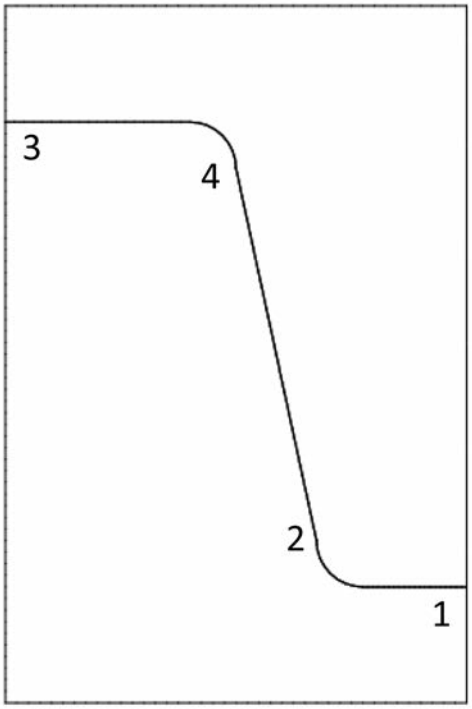

Figure 20. Release process includes multiple dynamic separation and arrest events as well as adhesive reattachment: 1-2, 2-3, reattach 2-4, 4-2.

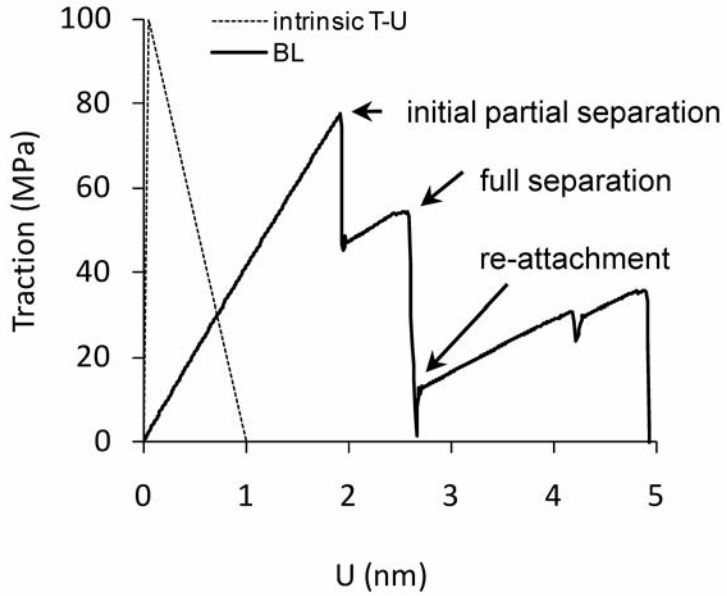

Figure 21. Pattern *T-U* relationship for the baseline (BL) calculation.

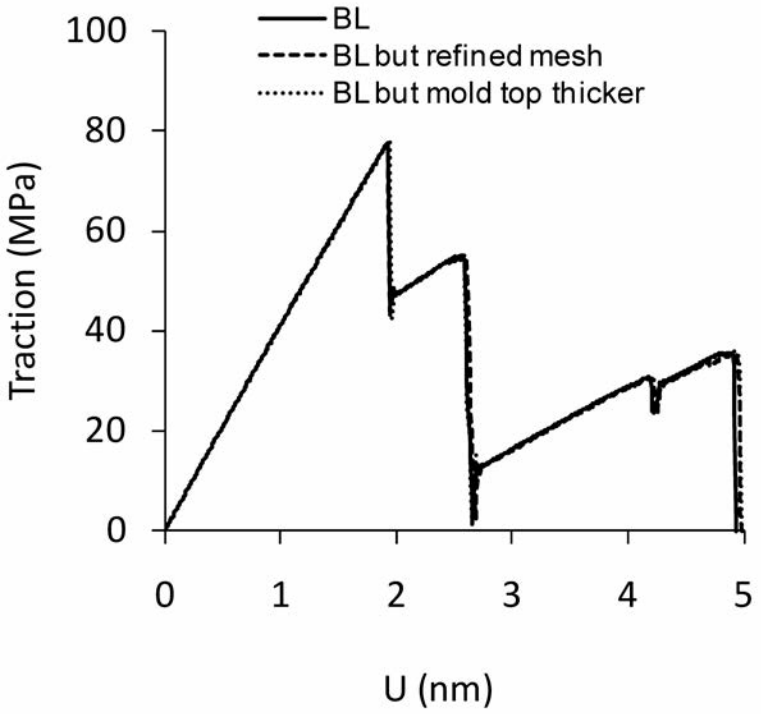

Figure 22. Effect of mesh refinement and an increase in mold thickness on calculated Pattern *T-U* relationship.

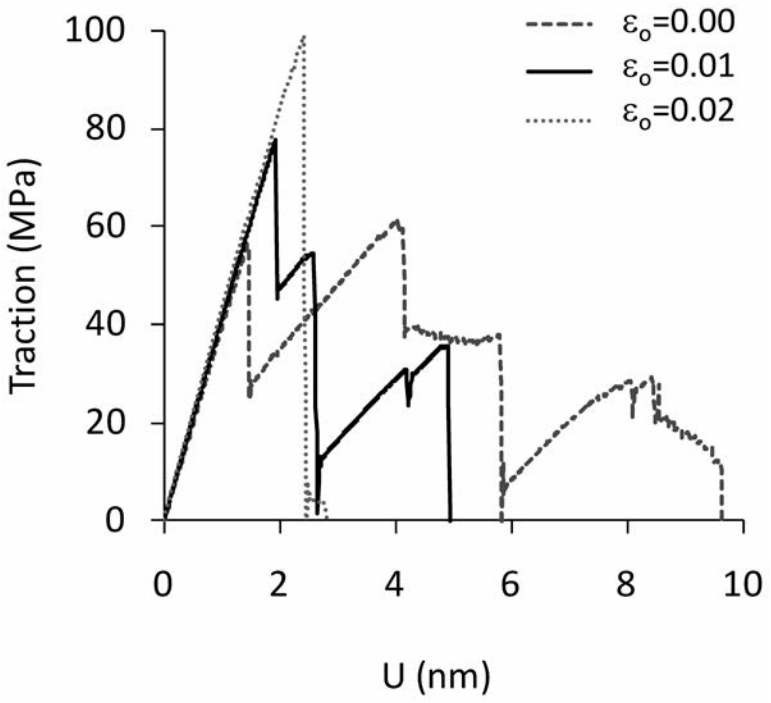

Figure 23. Affect of polymer shrinkage ε_o on the Pattern *T-U* relationship.

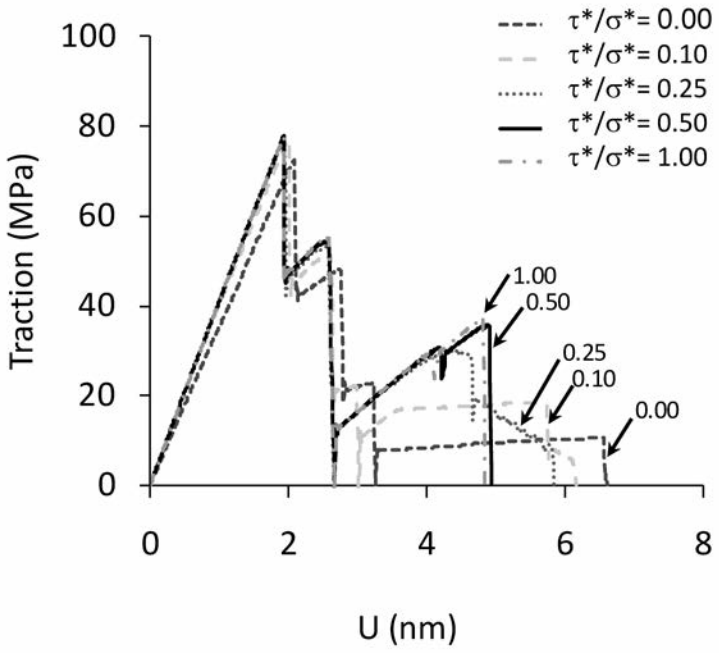

Figure 24. Affect of τ^*/σ^* on the Pattern *T-U* relationship.

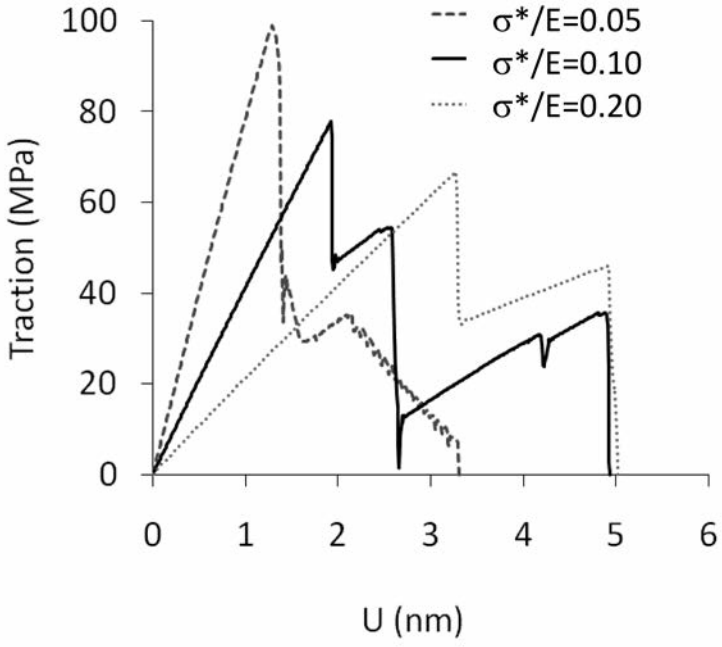

Figure 25. Affect of *σ*/E* on the Pattern *T-U* relationship.

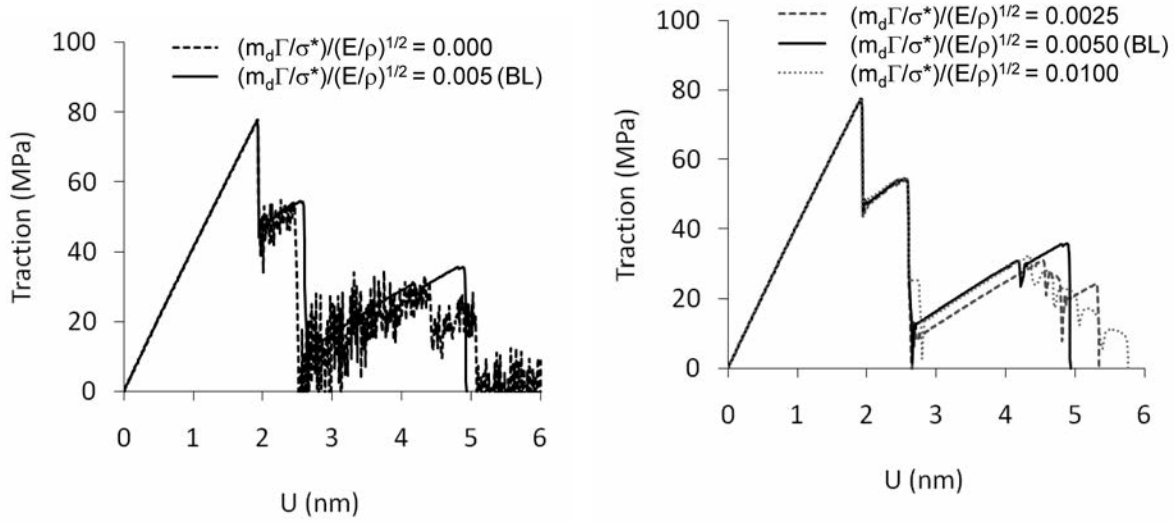

a) b)

Figure 26. Affect of mass proportional damping on the Pattern *T-U* relationship, a) no damping, and b) $(m_d\Gamma/\sigma^*)/(E/\rho)^{1/2}$ varied.

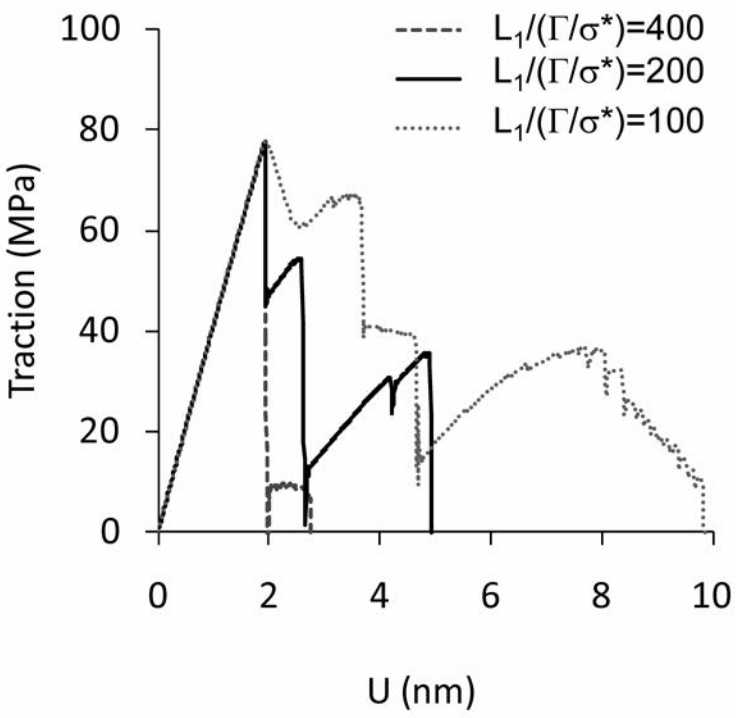

Figure 27. Affect of $L_1/(\Gamma/\sigma^*)$ on the Pattern *T-U* relationship (Γvaried in calculation) .

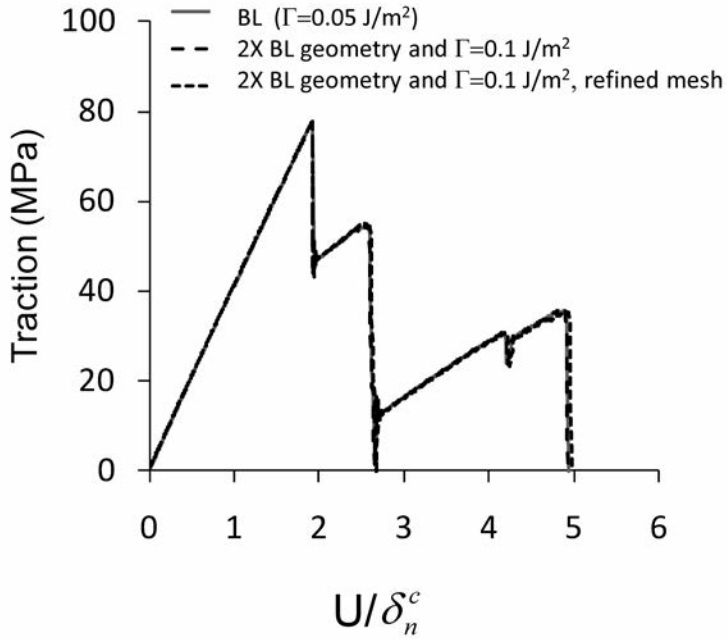

Figure 28. Affect of $L_1/(\Gamma/\sigma^*)$ on the Pattern *T-U* relationship (L_1 and Γ varied in calculation).

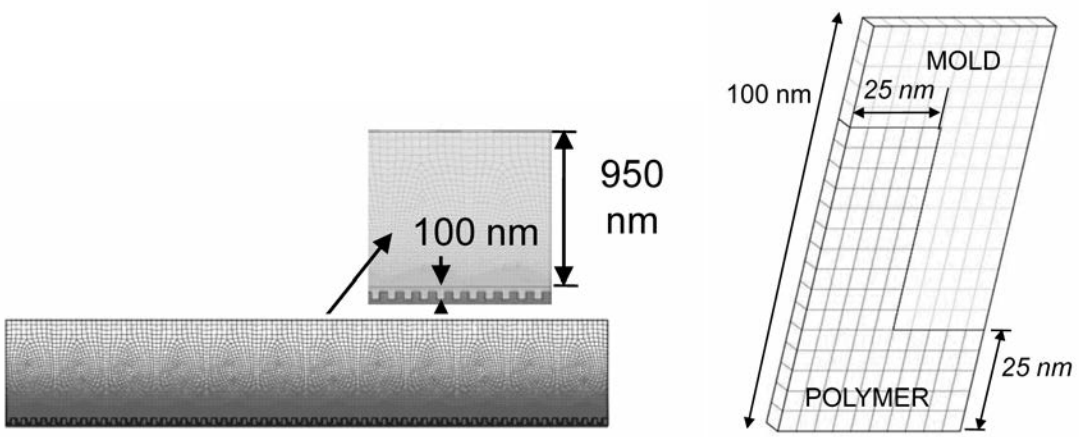

a) b)

Figure 29. Models used in hierarchical analysis. a) 60-channel model, and b) unit cell model.

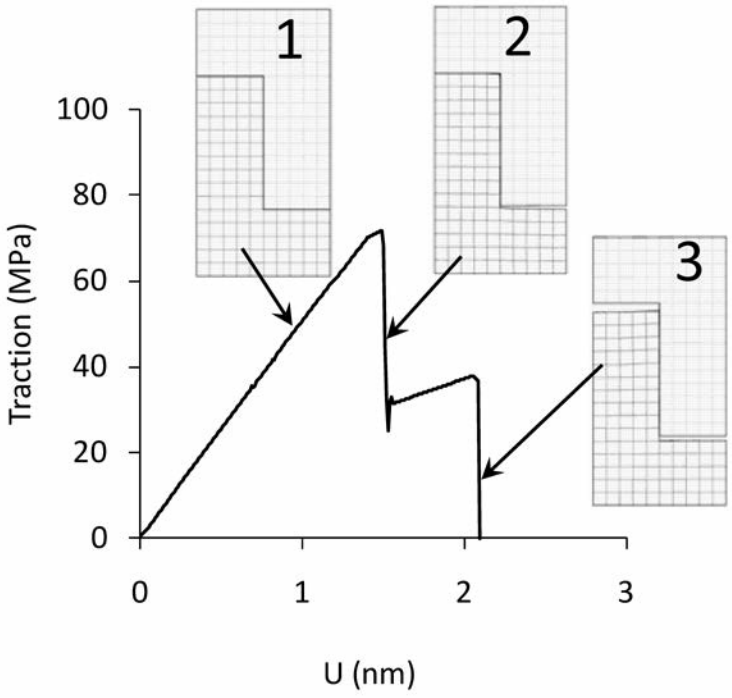

Figure 30. Calculated Pattern *T-U* relationship as determined from the unit cell analysis.

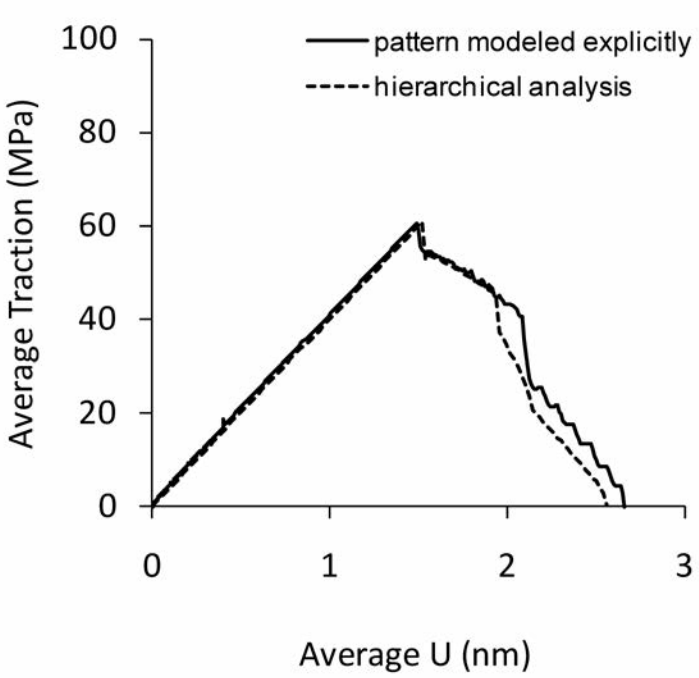

Figure 31. Calculated average applied traction vs. the average applied displacement as determined by an analysis that explicitly models the 60-channel pattern is compared to hierarchical analysis result.

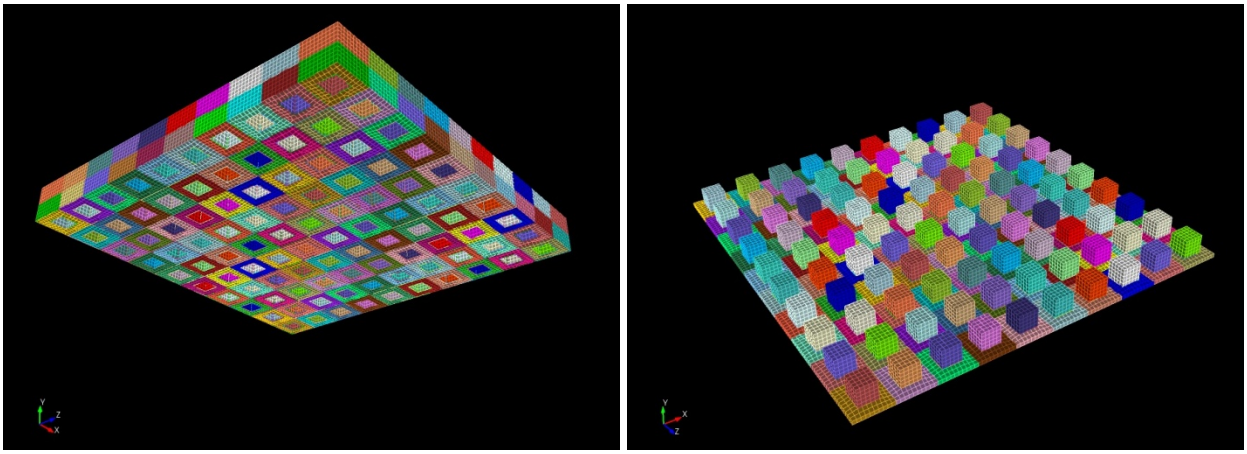

a) b)

Figure 32. Example model of a 10x10 grid of cells with cube-shaped pillars, where a) denotes the mold, and b) denotes the polymer pattern.

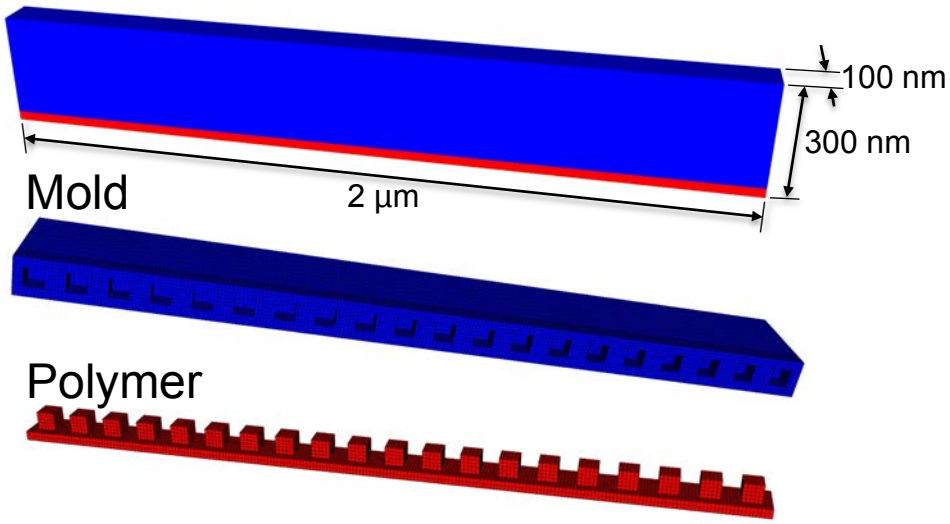

Figure 33. A 20-pillar strip model to which back and front surface symmetry conditions are applied so as to represents an array of parallel strips.

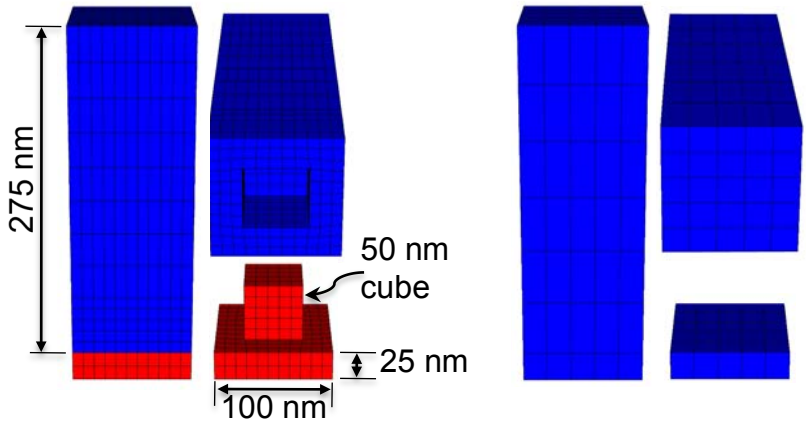

a) b)

Figure 34. Unit cell models with (a) patterned interface and (b) smooth interface.

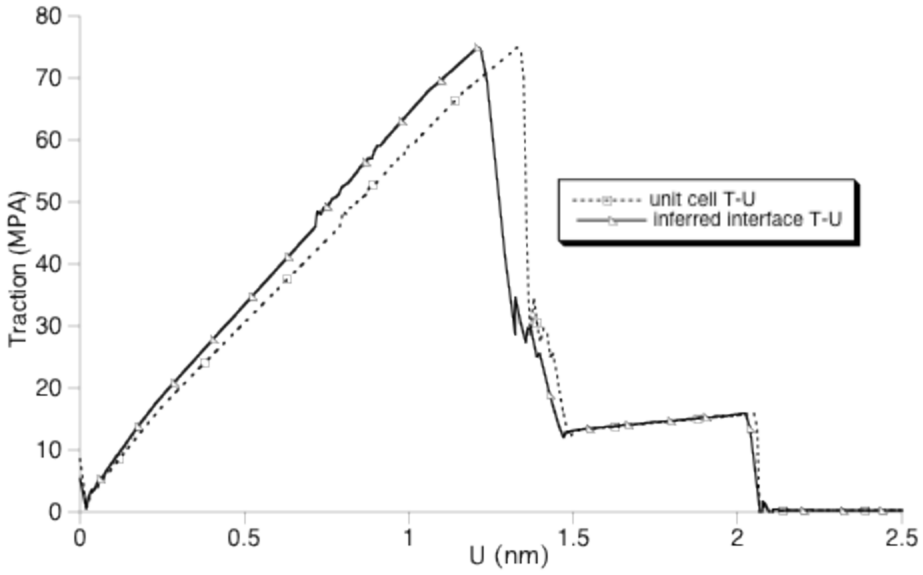

Figure 35. Pattern *T-U* response as determined by unit cell analysis.

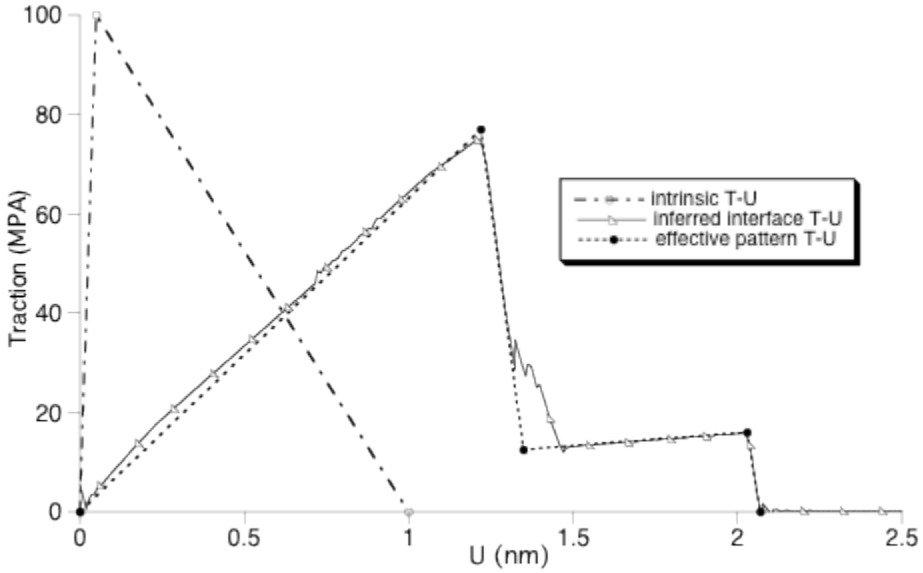

Figure 36. Intrinsic *T-U* used in unit cell analysis, inferred interface *T-U*, and Pattern *T-U (a* piece-wise linear representation).

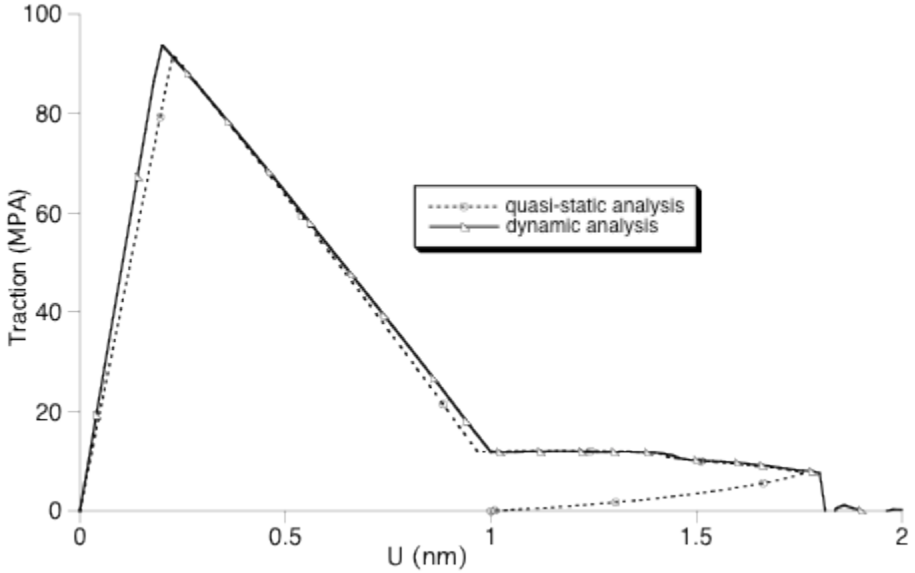

Figure 37. *T-U* responses for quasi-static and dynamic analysis showing snap-back behavior ands energy loss due to dynamic response (a different unit cell configuration was used in this exploratory calculation).

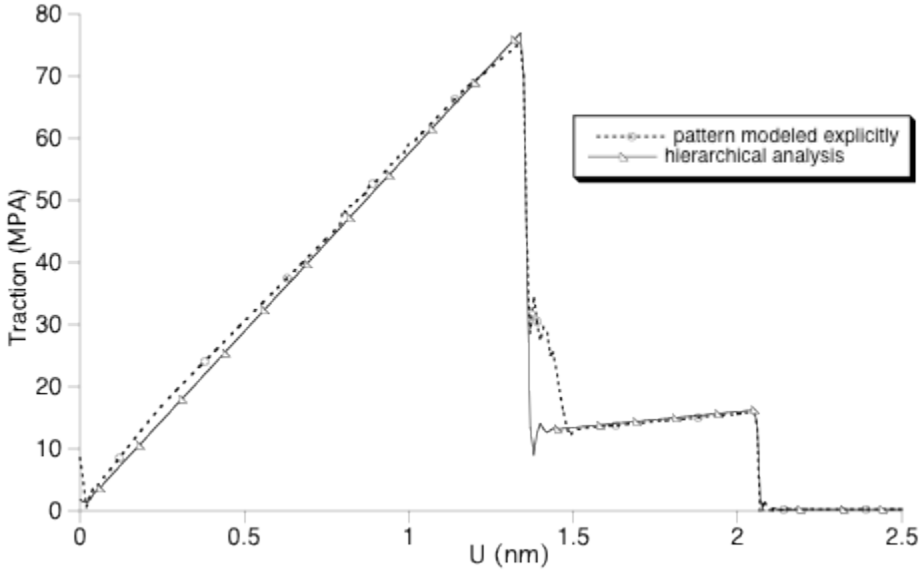

Figure 38. *T-U* responses for the unit cell specimen with pattern modeled explicitly and with a hierarchical analysis incorporating the effective Pattern *T-U* model.

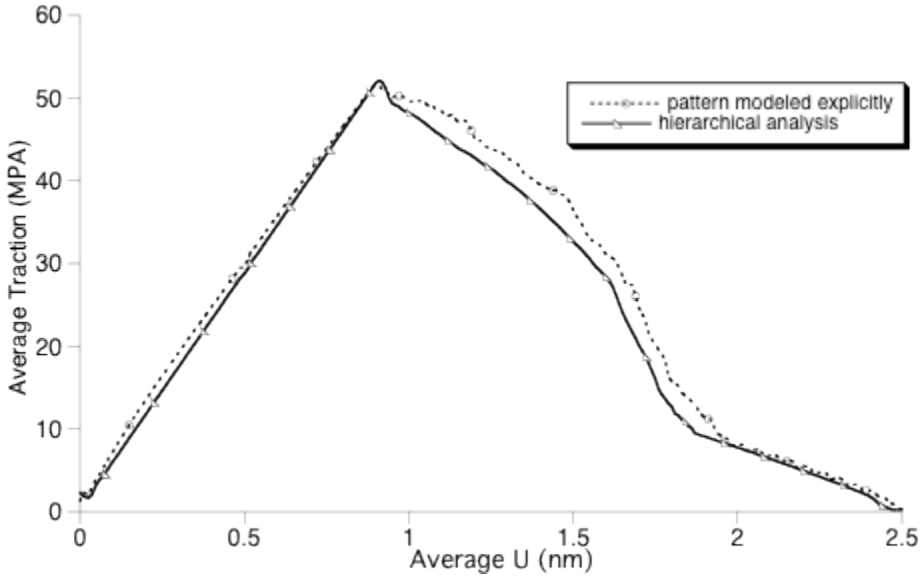

Figure 39.Calculated average applied traction vs. the average applied displacement as determined by an analysis that explicitly models the 20-pillar pattern is compared to hierarchical analysis result.

3 IMPRINTING

3.1 Single feature scale

Nano-imprinting typically implies a process which imprints simultaneously a large number of small (nano-scale) features over a wafer or portion of a wafer. The J-FIL epitomizes nano-imprinting, as it is currently used to produce trillions of features over a square inch. In contrast, what is often termed *nano-indenting* generally involves the process of impressing or molding one feature at a time. Of course understanding the physics at the single feature scale is imperative in building predictive models at meso- and machine-scales. This is the purpose of work presented in Section 2.1 and 2.2 of this report, from a solid-state standpoint. In those studies a clear understanding of the governing physics underpinning nano-indentation of a single or several features at a time are laid plain. In the liquid state, the process is really akin to mold-filling. That is to say the features are filled either an overpressure of liquid and/or through the affinity of liquid to the solid (capillary wetting forces). Actually, in J-FIL and related processes which employ relatively low viscosity liquids, the process is dominated by capillary wetting forces.

Reddy et al. (2005) used numerical models to determine the key physics of a single feature fill under the conditions of a typical imprinting process. Somewhat surprisingly, a wetting liquid was found to fill a feature with a sweeping motion characterized by a process in which inertia and viscosity far-dominate surface tension in the meniscus. This means the meniscus is highly non-spherical during the event, as shown in the Figure 40 below, even at these tiny length scales. Equilibrium capillary hydrostatics cannot explain the process.

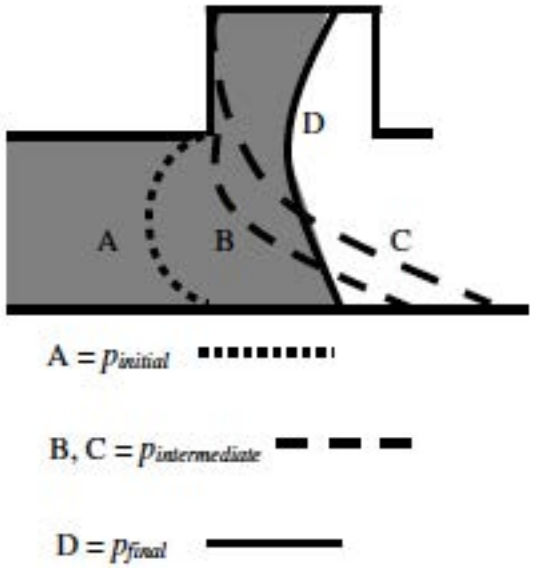

Figure 40: Cartoon of the meniscus shape during a single feature fill as determined from finite element simulations. Reprinted with permission from Reddy and Bonnecaze (2005)

Several other efforts to study the underpinning physics of single and multiple feature filling are noteworthy. Morihara et al. (2009) in work similar to Reedy et al. examined in detail the effect of equilibrium contact angle on the substrate and template, and of course discovered the more hydrophobic the template, the greater the likelihood for trapped gas and incomplete fills. Reddy

and Bonnecaze (2005) proposed a criteria for filling based on the liquid phase pressure as a menisci approached the a feature, and the resulting pressure in equilibrium as the menisci wets the upper part of the notch (Figure 40, state D). They used this heuristic in a planform model (see figure 41 below) to gauge whether a feature would fill given the local conditions. In that model thin-film lubrication theory was deployed coupled with a volume-of-fluid front capturing scheme. This work is the only close precedent that we know of to our approach presented in Section 3.2.

Rowland et al. (2005) used finite element modeling to examine the filling of micron-sized features of various aspect ratios. Their conditions corresponded to what we term the "embossing" regime, with the embossed material being a soft solid which is locally melted with applied thermal resistance heating. Their work led to an operating map which related an embossing pressure to the propensity of the final feature shapes to exhibit near-net-shape patterns or exhibit undesirable defects.

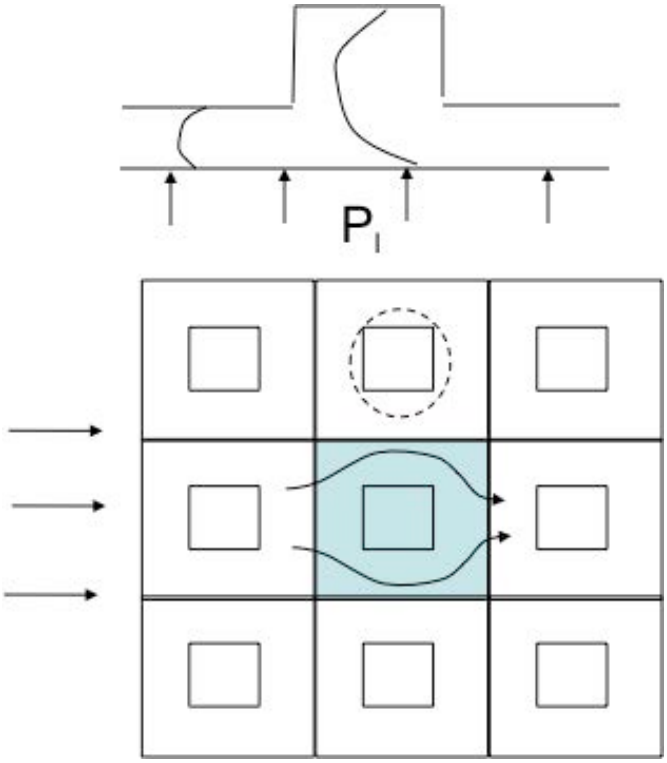

Figure 41: Planform model of multiple feature filling. Features are simply locations of height-function variations in a Reynold's lubrication model. (Reddy and Bonnecaze (2005)).

In the early stages of this effort we undertook single-feature filling models in two- and three-dimensions using ARIA (Notz et al. 2007) and GOMA (Schunk et al. 2006). Although successful, too many resources were being consumed to determine quantitatively a feature filling criteria that would be useful at larger scales. Because the overall goal or our research was to achieve machine-scale modeling we elected to put more resources in that area.

At the wafer/machine scale, 100s of millions over a trillion features are filled in a single step. Clearly it would be next to impossible to resolve such features in a finite element model at that scale. Modeling at this scale requires some form of coarse graining, or in other words implementing sub-grid scale physics. This is the subject of section 3.2 and 3.3, in which we describe an effective-porous medium approach to the problem. That said, incomplete filling defects persist and hence there is still an outstanding need for a stochastic probability model of filling events that could possibly be derived from feature-level analytical or numerical models. We know that imprint pressure, substrate and template contact angle, imprint material rheology, template flexibility, feature shape and feature density all play a role in whether a feature fills. Building a probabilistic model for a subscale is probably the best route here, based of first-principle simulations in 3D at the feature-resolved mesoscale. We will leave this as an item of future research.

3.2 Machine/wafer scale methods and models

Before we describe our methods and model development we deploy at the wafer scale, we summarize the numerical machinery required to accomplish the goal. This is the subject of 3.2.1, in which we summarize the specific code development activities that were necessary. In Section 3.2.2 and Section 3.3 we address the model of JFIL itself in stages.

3.2.1 Computational capabilities required for the machine scale.

The imprinting stage of J-FIL is best described as a mechanical process involving a substrate, imprinting fluid (photoresist), and a featured template which is flexible at the machine scale. The mechanics of imprinting is made up of multiphase fluid flow with capillary free surfaces and wetting, fluid-structural interaction, and an effective medium impregnation in which a liquid is transferred from a continuous gap to a medium which can hold some significant inventory of liquid (the remaining liquid on the substrate and in the gap being termed the "residual layer"). The single most important distinguishing feature of this process from a computational standpoint is that it involves extremely thin structures and fluid regions (viz. regions of very large aspect ratios, of order 1 million or more). Another important characteristic of the process that drives our selection of computational approaches is the hole/feature pattern at the wafer scale which dictates which portion of the processing area that can take up photoresist. The final complication is that the whole system is structurally compliant, by design. Our computational approach must accommodate these physics in a manner that is expedient enough to be practical. When dealing with such large aspect ratios and millions if not trillions of features, reduced-order modeling approaches are the only practical recourse.

These distinguishing features drove our model development. Underpinning that development, code-infrastructure activities had to be carried out. Specifically, we added to the finite element code Goma an infrastructure to handle shell elements together with a variety of shell equations described in subsequent sections. We also developed a unique pattern-to-mesh capability which enables surface structural patterns of imprint templates to be mapped onto a finite element meshes without the need to mesh-in the features. We discuss in this section the development of this mapping tool. Much of the shell-capability is discussed in Sections 3.2 and 3.3. It is important to point out here, however, that our implementation in GOMA allows for generalized shells in three-dimensional space which can be structurally deformed (curved) and mated to bulk continuum regions, viz. these elements can interact with neighboring continuum elements for

structures, fluids, or porous regions, which in particular makes the capability unique. Surveying available commercial and in-house FEM codes we found no equivalent capability outside of traditional structural shells. This survey includes codes like COMSOL, FLUENT and many of the SIERRA applications. Section 3.2.2 and Section 3.3 review our capability and demonstrate its use on several standard test problems.

3.2.1.1 Pattern-to-Mesh Template Mapping

Complex shapes and structures are often difficult to resolve in finite element models. Oftentimes such sub-structure in a model represents a second phase with different thermophysical properties, or a geometric discontinuity that could be an impediment or barrier to flow, as in a fracture/gap which has opened up in a porous material. The sub-structure could be confined to a surface, such as surface roughness or small-scale features on a wall, or a chemical heterogeneity on a surface that leads to rapidly varying surface energies.

Successful models in computational mechanics often have to deal with these complexities, either through direct simulation (truly representing the geometric region with the correct physical equations) or through coarse-graining, in which a model requires representative physics at a coarser grid level which relate to some finer scale phenomena.

The new pixel-to-mesh-image (PTMI) capability in Goma greatly facilitates these sorts of complexities. The obvious, "rich-man's" solution to the problem would be to construct a body-fitted mesh to various and sundry finer-scale features of a model, thereby creating clear mesh boundaries between which different physics in different materials can be specified or prescribed. Unfortunately, if the structure is somewhat complicated, the meshing can get onerous and impractical. A much more expedient approach would be to represent the substructure with a smooth finite-element representation of the varying physics or thermophysical property. The following example helps demonstrate the benefit of this approach.

Shown in Figure 42 (left-and-side) is a body-fitted finite element mesh of a portion of a micro-fluidic device surface structure. The magenta regions represent holes and trenches that are by design etched into the surface to accommodate further processing needs in assembly. Those regions actually represent shallow holes, and the problem at hand is to predict the flow through this surface structure with an opposing flat plate wall. This mesh contains 3000 elements and solving the thin film lubrication equations (cf. Schunk et al. 2011) within this mesh requires to time-marching of a problem with 3000+ unknowns. Moreover, it is desired that the holes and trenches have rounded corners, but in this model such features using lubrication are hard to prescribe in the model.

On the right of Figure 42 is a pixelated representation of the very simlar pattern. The pixels are colored with a gray scale, meaning they vary between white and black. Where there are no pixels, the color is defined as pure white. This image was created with the GNU IMage creation Program, GIMP. Note that the features are actually smooth, showing a darker core and a gradual lightening (lower pixel value/density) towards the edge. This may in fact be desirable for the application at hand. This GIMP figure could have easily been generated so that we have pure black features with sharp edges and no gradual transition.

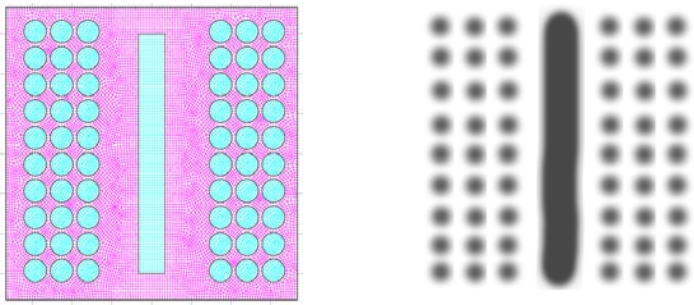

Figure 42: Body-fitted finite element mesh of an arbitrary surface device structure (left) and a pixel representation of the same structure (right).

The pixel image can be further manipulated, of course, using various and sundry filters and image processing procedures which could be useful for coarse-graining an image for multiscale processing, etc. In any case, as you may already be thinking, if this image could only be imprinted onto the finite element mesh, a plethora of time-saving capabilities with regard to the following applications could be realized:

- -Bringing in experimental images of microstructure into a model
- -Scaling variable thermophysical properties in a model off the intensity of an image
- -Multiscale coarse-graining for multiphase flow models
- -Experimental model fitting (optimization) where discrete measurement points are far fewer than the resolution of the grid

Of course for these benefits to be realized, the host finite element code must provide the hooks to scale parameters and properties of the model off of image fields. Well, in Goma this benefit is now available using its external field capability and a new on-board pixel-to-mesh image mapping capability.

Basic Algorithm

The idea pursued in this work is to map the pixel field into a finite-element representation of some user-specified interpolation. In this way the field can be evaluated (interpolated) at any point in the domain. A related capability already exists in GOMA which enables external field variables to be read in as an ExodusII nodal field, which can further be accessed as an interpolated field variable (cf. `External Field` card).

If we take p^h as the functional representation of a pixel field, which is comprised of point positions x_j, y_j, z_i, and an associated magnitude p^*_j, where the index j runs over all the pixel points, then we desire to represent the coordinates and the magnitude of that pixel value in the following form:

$$\underline{x}^h \equiv \sum_i \underline{x}_i \phi_i(\underline{\xi})$$
$$p^h \equiv \sum_i p_i \phi_i(\underline{\xi}) \qquad (1)$$

Here x_i and p_i are the nodal values of the coordinates and the pixel field on the finite element mesh, and ϕ_i are finite element interpolation functions (low-order polynomials defined at each node *i* in the mesh and nonzero locally only over elements containing node *i*). $\underline{\xi}$ is a vector of isoparametric (local) coordinates of each element in mapped space. To achieve that mapping onto a regular unit cube (or square in 2D space), a Jacobian is of course defined:

$$\frac{\partial \underline{x}}{\partial \underline{\xi}} = \sum_i \underline{x}_i \frac{\partial \phi_i}{\partial \underline{\xi}} \tag{2}$$

Clearly, the unknowns in this problem are the nodal values of the pixel-field, $p_{i,,}$ which need to be obtained from the arbitrary locations and magnitudes of the individual pixels. So to map one field we will be solving a system of equations for *N* values of $p_{j,}$ where *N* is the number of nodes in the mesh. Specifically, we need to solve the following set of algebraic equations:

$$p_j^* - \sum_i p_i \phi_i(\underline{x}_j) = 0 \text{ for all } j = 0, 1, \ldots M\text{-}1 \tag{3}$$

Here *M* is the number of pixel points to be mapped, p_j* as mentioned above is the pixel value, and $\underline{x}_j$ are the associated pixel location, a coordinate vector. Comparing this set of equations with the finite element representation of p^h above, you will notice that in this case the basis functions are expressed in terms of physical coordinates and not isoparametric coordinates. In GOMA, basis (or interpolation) functions are programed in terms of isoparametric coordinates $\underline{\xi}$. Thus, evaluating Equation 3 requires us to determine the local isoparametric coordinates from the physical coordinates $\underline{x}_j$ of each pixel by solving the second half of Equation 1 for the corresponding $\underline{\xi}$. This is a nonlinear problem which starts by locating the element in which each pixel is located (a search algorithm) followed by solving the inverse map.

In any case, examining Eq. 3 we see that the system of linear equations is in general non-square. That is there will be either fewer unknowns than equations if the number of nodes in the acceptor mesh is less then the number of pixels (which is likely going to be the case), or vice versa. Actually the latter case may arise in solving optimization problems where the number of discrete measurement points is much less than the number of nodes.

Solving Eq. 3 in general is not trivial. Searching the web we found that only LAPACK can solve a non-square matrix system of equations (over-determined system with more equations than unknowns). Specifically the *dgels* routine in LAPACK deploys a linear least-squares method based on "Householder transformations". Our initial implementation deployed *dgels* successfully, but the performance was disappointing, with solutions often taking 10-20 minutes on a modern workstation for small images mapped on two-dimensional meshes with on the order of 100 nodal points.

Fortunately, another approach to solving Eq. 3 has thus far proved to be much more efficient. We can rewrite Eq. 3 as:

$$\underline{\underline{A}}\,\underline{p} = \underline{p}^{*} \qquad (4)$$

where $\underline{p}$ is the vector of nodal values of the pixel fields (the unknowns), $\underline{p}^*$ is the vector of pixel values from the image, and $\underline{A}$ is the matrix $\sum_i \phi_i(\underline{x}_j)$ for all $j=1$ to M pixel points. That is to say $\underline{A}$ is an MxN matrix, $\underline{p}$ is a vector of length N (nodal points) and $\underline{p}^*$ is a vector of length M pixel points. We now multiply Eq. 4 with the transpose of A, denoted as A^T:

$$\underline{\underline{A}}^T\,\underline{\underline{A}}\,\underline{p} = \underline{\underline{A}}^T\,\underline{p}^{*}$$

This system of linear equations is now of full rank and can be solved with any standard direct or iterative method. We implemented this approach in GOMA using the Trilinos 10.2 library. Within Trilinos we deployed the Epetra matrix objects to form the set of linear equations and Aztec00 to solve the system. Specifically we use simple Bi-Conjugate gradient iterative scheme with a Neumann preconditioner. The solution performance in our early testing is far superior to using the least-squares method in LAPACK.

3.2.2 Methods development – Lubrication, multiphase flow, and fluid-structure interaction.

3.2.2.1 Introduction

The theory of lubrication flow has been in use for well over a century, beginning with Tower's 1883 experiments of a rolling bearing [Tower (1883)] and the landmark mathematical formulation of Reynolds in 1886 [Reynolds (1886)]. Since then, countless studies have used Reynolds' theory to analyze lubricating flows for numerous scientific and practical manufacturing applications, including journal bearings, coating beads, and hard-drive read heads [Wada1971,Wada1971a,Booker and Huebner (1972), Christensen (1972), Higgins and Scriven (1980), Anturkar et al. (1990), Heil and Pedley (1995), Bhagavat et al. (2000), Kothmann and Stefani (2001), Hori (2006), Szeri (2010)]. Many extensions of this basic theory exist, including elastohydrodynamic lubrication [Greenwood (1972), Taylor and O'Callaghan (1972), Oh and Huebner (1973), LaBouff and Booker (1985), Jones (1993), Brodsky and Kanamori (2001), Zhang and Wen (2002), Nair and Nair (2004)], thermohydrodynamic lubrication [Cheng (1965), Huebner (1974), Ferron et al. (1983), Yang et al. (2001), Guo et al. (2001)], turbulent hydrodynamic lubrication [Constantinescu (1959), Ng (1964), Elrod and Ng (1967), Hirs (1973)], and lubrication of non-Newtonian fluids [Ng and Saibel (1962), Swamy et al. (1977), Johnson1993,Bhattacharjee and Das (1996), Hryniewicz et al. (2001), Nair et al. (2007), Mongkolwongrojn and Aiumpronsin (2010)], among others [Christensen (1971), Eringen and Okada (1995), Feng and Weinbaum (2000), Stone (2005), Jang and Khonsari (2005), Bujurke and Kudenatti (2007), Rojas et al. (2010)]. Recent books by Hori [Hori (2006)] and Szeri [Szeri (2010)] thoroughly review the history and applications of lubrication theory and derive the governing equations.

In practice, lubrication theory is commonly used to study problems where the geometry is either simple, such as in slider bearings, or regular, as in journal bearings. These types of problems often lend themselves to elegant analytical solutions [Reynolds (1886), Stone (2005)] or simple numerical solutions involving finite difference or finite element techniques [Wada1971,Booker and Huebner (1972)]. When these techniques are used, the equation is often specifically adapted to the given geometry, and a custom computer code is written for solving the specific problem. Flows in complex geometries are typically studied using full three-dimensional simulations in a large-scale, unstructured finite element code, such as GOMA [Schunk et al. (2006)]. Yet, problems involving thin fluid layers, such as coating flows with tensioned webs [Feng (1998), Nam and Carvalho (2010)] and imprint lithography [Bailey et al. (2001), Liang et al. (2007), Sreenivasan (2008), Chauhan et al. (2009)], may benefit significantly from the mathematical order reduction provided by lubrication theory using shell-type elements within a larger 3-D code. Shell elements have been used for decades in the solid mechanics community for modeling thin materials [Bathe and Dvorkin (1986), Bischoff and Ramm (1997), Nguyen-Thanh2008], but their use in fluid dynamics has been relatively rare [Heil and Pedley (1995)]. However, the coupling of curvilinear shell elements for fluid flows with 3-D elements for solid deformations would allow the study of elastohydrodynamic lubrication in complex geometries via a direct coupling with continuum solid element regions. Few studies have used these fluid-structure interactions (FSI) to couple lubrication shell elements with 3-D solid deformation [Nair and Nair (2004), Nair et al. (2007)].

In all of the previously cited studies, the lubrication layer was a single liquid phase confined between two substrates, either rigid or deformable. While there have been considerable work on unconfined or multilayer lubrication flows, modeled by the thin film equations [Oron et al. (1997)], there have been no computational treatments of confined multiphase lubricating flows together with a free interface across the thin film. Such flows may arise in nanomanufacturing processes [Liang et al. (2007), Chauhan et al. (2009)], problems involving capillary rise [Taylor (1712), Hauksbee (1712), Higuera2008], and in air entrainment in coating flows [Kistler and Scriven (1984), Coyle et al. (1986)]. In continuum, 3-D fluid calculations, the level-set method is commonly used for tracking fluid-fluid interfaces and incorporating the effect of surface tension [Brackbill et al. (1992), Kang et al. (2000), Sussman (2003), Sussman et al. (2007)]. More recent extensions of this method exploit a balanced-force approach to the level-set method, allowing the use of a sharp interface without requiring an embedded boundary [Francois et al. (2006), Herrmann (2008)]. Implementation of the balanced-force level-set method alongside a modified Reynolds' equation allows the solution of multiphase lubrication problems using the finite element method.

In this paper, we develop a model for multiphase lubrication flow inside of a 3-D finite element framework. Reynolds' lubrication equation and the level-set equations are solved with curvilinear shell elements, while solid boundaries are modeled with unstructured 3-D continuum elements. In Sec. 3.2.2.2 we present the governing equations implemented in this model, and in Sec. 3.2.2.3 we lay out the numerical implementation. This method is demonstrated through example problems in Sec. 3.2.2.4 and compared with analytical solutions and experiments. Finally, we summarize our model and suggest future extensions in Sec. 3.2.2.5.

3.2.2.2 Governing equations

In this section, we present the governing equations for multiphase lubrication flows and deformable solids. We begin with the Reynolds' equation for lubrication flows (Sec. 3.2.2.2.1), then generalize it to include free interfaces (Sec. 3.2.2.2.2). Next, we describe the classic equations for nonlinear elastic materials (Sec. 3.2.2.2.3), concluding with a discussion of the fluid-structural interactions coupling the multiphase lubrication flow with the motion of the elastic solid (Sec. 3.2.2.2.4).

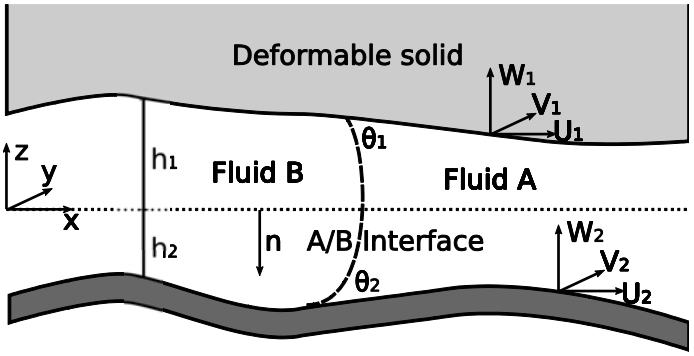

Figure 43: Illustration of the geometry used in this model.

The geometry used in the development of this model is illustrated in Fig. 43. Two fluids (A and B) are shown, both confined between two walls (1 and 2). The two fluids are separated by an interface, illustrated by the dashed line. Fluid A has contact angle θ_1 with the top wall and angle θ_2 with the bottom wall. In this diagram, the bottom wall is taken as rigid and the top wall as deformable. The height of these walls can vary spatially and with time, and their positions relative to the base location (which is shown with the dotted line) are denoted by h_1 and h_2. The height h_2 is defined with respect to the coordinate reference plane such that $h = h_1 - h_2$ and $h_2 < 0$ as shown in Fig. 43. Arbitrary height models may be included in the form of $h_i = f(x, y, t)$ to obtain complicated topology. Both walls can move normal and tangential to the fluid, with the velocity vectors $\mathbf{B}_i = [U_i, V_i, W_i]$.

It is important to note that although the base lubrication location (dotted line) is shown in Fig. 3.2.2.1 aligned in the $x - y$ plane, it may in fact be oriented arbitrarily and curve within a single geometry. Therefore, the location and orientation of the fluid layer is determined by two factors. First, large scale variations are included by deviations to the base location (dotted line), which allows the study of complex shapes (by creating a computational mesh which conforms to that shape). Second, smaller length-scale variations, such as fine patterns, are included through deviations in the heights h_1 and h_2, which are always normal to the base location.

3.2.2.2.1 Reynolds' lubrication theory

Reynolds' lubrication theory is a simplification of the Navier-Stokes equations under a number of assumptions [Hori (2006), Szeri (2010)]. For our model, the four key assumptions used to simplify the Navier-Stokes equations are:

1. The flow is laminar
2. The fluid pressure is constant across the film thickness,
3. There is no slip between the fluid(s) and solid walls,
4. The rate of change of the velocity in the flow direction is very small compared with the rate of change in the direction normal to the flow.

Many models exist for relaxing assumption 1 to study turbulent flows [Constantinescu (1959), Ng (1964), Elrod and Ng (1967), Hirs (1973)]. These models have been easily be incorporated into our formulation, but have been omitted here for simplicity of the presentation. Detailed derivation and discussion of these governing equations can be found elsewhere [Hori (2006), Szeri (2010)], so we begin our discussion with the simplified mass and momentum conservation equations.

We begin with a form of the momentum and mass conservation equations consistent with the assumptions of the lubrication approximation,

$$\begin{aligned} \frac{\partial p}{\partial x} &= \mu \frac{\partial^2 u}{\partial z^2}, \\ \frac{\partial p}{\partial y} &= \mu \frac{\partial^2 v}{\partial z^2}, \\ \frac{\partial p}{\partial z} &= 0, \\ 0 &= \frac{\partial u}{\partial x} + \frac{\partial v}{\partial y} + \frac{\partial w}{\partial z}. \end{aligned} \tag{1}$$

Here, p is the pressure, $\mathbf{u} = [u, v, w]$ is the velocity, and μ is the Newtonian viscosity. This formulation is consistent with a flow aligned in the $x - y$ plane and with the film thickness aligned with the z coordinate. These equations can be solved with no-slip boundary conditions at the top, $\mathbf{u}|_{h_1} = \mathbf{B}_1 = [U_1, V_1, W_1]$, and bottom, $\mathbf{u}|_{h_2} = \mathbf{B}_2 = [U_2, V_2, W_2]$, walls to obtain the equation

$$\begin{aligned} &\frac{\partial}{\partial x}\left(\frac{h^3}{12\mu}\frac{\partial p}{\partial x}\right) + \frac{\partial}{\partial y}\left(\frac{h^3}{12\mu}\frac{\partial p}{\partial y}\right) \\ &+ \frac{1}{2}(U_1 - U_2)\left(\frac{\partial h_1}{\partial x} + \frac{\partial h_2}{\partial x}\right) + \frac{1}{2}(V_1 - V_2)\left(\frac{\partial h_1}{\partial y} + \frac{\partial h_2}{\partial y}\right) \\ &= \frac{h}{2}\left(\frac{\partial U_1}{\partial x} + \frac{\partial U_2}{\partial x} + \frac{\partial V_1}{\partial y} + \frac{\partial V_2}{\partial y}\right) + W_1 - W_2, \end{aligned} \tag{2}$$

where the film thickness $h = h_1 - h_2$. The first two terms on the left-hand side of this equation account for flow due to pressure gradients, or Poiseuille flow, which may be generated by either an imposed pressure gradient or by the other body forces. The other two terms on the left-hand side account for forces due to relative shear motion of the boundaries when the channel is either converging or diverging, as in a slider bearing. Note that a pressure gradient is not generated from shear forces if both boundaries are parallel. On the right-hand side of the equation, the first

set of terms account for pressures generated from non-uniform movement of the boundaries, such as dilational or rolling motions. Finally, the last two terms account for the pressure from either squeezing flows, where the boundaries move in the normal direction, or from flow through the boundaries, as in porous flows.

Equation (2) can be put into vector notation by creating a surface gradient operator, $\nabla_{\text{II}} = [\partial/\partial x, \partial/\partial y, 0]$. This gives the formulation

$$\nabla_{\text{II}} \cdot \left(\frac{h^3}{12\mu} \nabla_{\text{II}} p \right) + \frac{1}{2} (\mathbf{B}_{1,\text{II}} - \mathbf{B}_{2,\text{II}}) \cdot \nabla_{\text{II}} (h_1 + h_2) = \frac{h}{2} \nabla_{\text{II}} \cdot (\mathbf{B}_1 + \mathbf{B}_2) + \mathbf{n} \cdot (\mathbf{B}_{1,\text{n}} - \mathbf{B}_{2,\text{n}}) \tag{3}$$

Here, $\mathbf{B}_{i,\text{II}} = [U_i, V_i, 0]$ is the portion of that velocity in flow direction, $\mathbf{B}_{i,\text{n}} = [0, 0, W_i]$ is the portion normal to the flow, and $\mathbf{n} = [0, 0, 1]$ is the vector normal to the flow.

As we do not want to restrict ourselves to flows aligned in the $x - y$ plane, we can generalize this equation simply by modifying the operators in (3) so that vectors and operators denoted by a subscript $_{\text{II}}$ are directed tangential to the flow and those denoted by a subscript n are normal to the flow. This is accomplished by redefining the surface gradient operator as a rotation of the full gradient operator, $\nabla_{\text{II}} = (\text{I} - \mathbf{nn}) \cdot \nabla$, where I is the identity tensor and $\mathbf{n}$ is the vector normal to the flow orientation. Correspondingly the velocity vectors $\mathbf{B}_{i,\text{II}} = (\text{I} - \mathbf{nn}) \cdot \mathbf{B}_i$ and $\mathbf{B}_{i,\text{n}} = \mathbf{nn} \cdot \mathbf{B}_i$.

Equation (3) can be expressed more compactly, and perhaps more intuitively, by defining a lubrication flow rate,

$$\mathbf{q} = -\frac{h^3}{12\mu} \nabla_{\text{II}} p + \frac{h}{2} (\mathbf{B}_{1,\text{II}} + \mathbf{B}_{2,\text{II}}). \tag{4}$$

The flow rate is directly related to the mean (thickness-averaged) velocity field, $\bar{\mathbf{u}}$, by the lubrication height:

$$\bar{\mathbf{u}} = \frac{1}{h} \mathbf{q}. \tag{5}$$

Note that the mean velocity field $\bar{\mathbf{u}}$ is not identical to the full velocity field, $\mathbf{u}$, which contains variations in the field through the film thickness. However, they are related by

$$\mathbf{q} = \int_{h_2}^{h_1} \mathbf{u} dh = h\bar{\mathbf{u}}. \tag{6}$$

This flow rate definition allows the flow terms in (3) to be written as a surface divergence of the flow rate, yielding the equation

$$-\nabla_{\text{II}} \mathbf{q} + \mathbf{B}_{1,\text{II}} \nabla_{\text{II}} h_1 - \mathbf{B}_{2,\text{II}} \nabla_{\text{II}} h_2 = \mathbf{n} (\mathbf{B}_{1,\text{n}} - \mathbf{B}_{2,\text{n}}). \tag{7}$$

While traditional lubrication theory ignores body forces, the effect of body forces along the flow direction may be easily included. For example, forces due to gravity can be posed as the gradient of a potential, and so can be integrated into the lubrication formulation in a similar manner as the hydrodynamic pressure gradient, viz.

$$\mathbf{q} = -\frac{h^3}{12\mu}\left(\nabla_{\mathrm{II}} p - \rho \mathbf{g}_{\mathrm{II}}\right) + \frac{h}{2}(\mathbf{B}_{1,\mathrm{II}} + \mathbf{B}_{2,\mathrm{II}}), \tag{8}$$

where ρ is the fluid density and $\mathbf{g}_{\mathrm{II}}$ is the gravitational force vector, rotated into the flow direction. Note that, consistent with the approximations of lubrication theory, gravity components and pressure gradients normal to the flow direction are assumed small and omitted.

3.2.2.2.2 Multiphase flow

The generalized lubrication equation (7) has been derived for a single fluid. However, it is possible to use lubrication analysis to study multiphase flows of two (or more) immiscible fluids. Each fluid may have different viscosities (μ_a, μ_b) and densities (ρ_a, ρ_b). In this situation, (7) applies for each fluid region separately, with the appropriate viscosity and density chosen.

At the interface between two fluids, a number of conditions apply. First, the velocity across the interface must be continuous, leading to the interfacial condition $\mathbf{u}^a = \mathbf{u}^b$. Second, a balance of normal stresses

$$p_a - p_b + \sigma \nabla \cdot \mathbf{n}_{ab} = \mathbf{n}_{ab} \cdot (\mathrm{T}_a - \mathrm{T}_b) \cdot \mathbf{n}_{ab} \tag{9}$$

and tangential stresses

$$-\nabla \cdot \sigma = \mathbf{n}_{ab} \cdot (\mathrm{T}_a - \mathrm{T}_b) \cdot \mathbf{t}_{ab} \tag{10}$$

must be enforced across the interface. Here, σ is the interfacial tension between the two fluids, $\kappa = \nabla \cdot \mathbf{n}_{ab}$ is the total curvature of the interface,

$$\mathrm{T}_i = \mu(\nabla_{\mathrm{II}} \mathbf{u} + (\nabla_{\mathrm{II}} \mathbf{u})^{\mathrm{T}}) \tag{11}$$

is the viscous stress (deviatoric part of the total stress) in fluid i, $\mathbf{n}_{ab}$ is the unit vector normal to the fluid interface, pointing into fluid b, and $\mathbf{t}_{ab}$ is the unit vector tangent to the interface. The present work only considers problems where surface tension is constant, so the first term in (10) is zero.

In this paper, we employ the continuum surface force method [Brackbill et al. (1992)] to incorporate (9)--(10) into the lubrication model. This method allows the automatic satisfaction of (10) through the use of weighted properties across the interface. The pressure jump arising from (9) is integrated into (8) through the addition of a surface tension body force, $\mathbf{F}_{\mathrm{CSF}}$:

$$\mathbf{q} = -\frac{h^3}{12\mu}\left(\nabla_{\mathrm{II}} p - \rho \mathbf{g}_{\mathrm{II}} + \mathbf{F}_{\mathrm{CSF}}\right) + \frac{h}{2}(\mathbf{B}_{1,\mathrm{II}} + \mathbf{B}_{2,\mathrm{II}}). \tag{12}$$

Details of the formulation of $\mathbf{F}_{\mathrm{CSF}}$ are shown in Sec. 3.2.2.3.2.

The total interface curvature, κ, must be adapted for use in a lubrication shell. The divergence of the normal vector can be decomposed into two principal radii of curvature, R_z and R_{II}. This yields the condition

$$\begin{aligned}\kappa &= \nabla \cdot \mathbf{n}_{ab} \\ &= \left(\frac{1}{R_z} + \frac{1}{R_{\text{II}}} \right) \\ &= \left(\kappa_z + \kappa_{\text{II}} \right)\end{aligned} \tag{13}$$

where κ_z is the curvature in the direction normal to the lubrication coordinate system and κ_{II} is the curvature in the surface direction.

Each curvature is calculated separately. As the lubrication equations do not resolve gradients in the normal direction, the normal curvature, κ_z, must be calculated from a model for the interface shape. We assume that the interface is an arc of a circle, intersecting the top and bottom boundaries with a static contact angle, θ_i. The normal curvature, therefore, can be expressed by

$$\kappa_z = \frac{1}{h}\left[\cos(\pi - \theta_1 - \text{atan}(S_1)) + \cos(\pi - \theta_2 - \text{atan}(S_2))\right], \tag{14}$$

where θ_i is the static contact angle at boundary i and S_i is the slope of boundary i in the direction normal to the interface, defined as $S_i = \mathbf{n}_{ab} \cdot \nabla_{\text{II}} h_i$. The curvature in the flow direction is calculated directly from the surface gradient of the normal vector of the interface,

$$\kappa_{\text{II}} = \nabla_{\text{II}} \cdot \mathbf{n}_{ab}. \tag{15}$$

3.2.2.2.3 Nonlinear elastic solids

The motion of an adjoining solid material is governed by the quasi-static momentum equation

$$\nabla \cdot \text{S} = \mathbf{0}, \tag{16}$$

where S is the Cauchy stress in the solid [Malvern (1969)]. The general compressible form of Hooke's law defines the Cauchy stress as

$$\text{S} = \lambda_s \varepsilon \text{I} + 2\mu_s \text{E}. \tag{17}$$

Here, λ_s and μ_s are the Lame parameters for the solid, ε is the volume strain, and E is the Green-Lagrangian strain tensor.

For this work we use the neo-Hookean constitutive model [Macosko (1994)] for the solid, which defines the volume strain as

$$\varepsilon = 3\left(\det(\text{F})^{1/3} - 1\right) \tag{18}$$

and the strain tensor as

$$\text{E} = \frac{1}{2}\left(\text{F} \cdot \text{F}^{\text{T}} - \text{I}\right), \tag{19}$$

in terms of the deformation gradient tensor F, where $\det(\text{F})$ is the determinant and F^{T} is the transpose of the tensor F. Under the assumption of small strain theory, the deformation gradient tensor is given by $\text{F} = (\text{I} - \nabla \mathbf{d})^{-1}$. Here, $\mathbf{d} = \mathbf{x} - \mathbf{X}$ is the material deformation, where $\mathbf{x}$ is the

current configuration and $\mathbf{X}$ is the original configuration. In this method, the material deformation $\mathbf{d}$ is the independent variable.

A number of boundary conditions can be applied to the solid motion. A common choice is a Dirichlet condition to either hold the solid in place or to move it with a specified displacement. Neumann conditions allow unrestricted movement at boundaries. Additionally, a force can be applied to any boundary, allowing transmittal of force from a lubrication layer through the solid, as is described in Sec. 3.2.2.2.4.

3.2.2.2.4 Fluid-structural interactions (FSI)

Closure of the equations of motion in both the structural and fluid-lubrication phase requires a kinematic condition that governs mass conservation across the interface and a vector condition that balances the local traction. The traction balance can be expressed by

$$\mathbf{n}\cdot(p\mathrm{I})+\mathbf{n}\cdot\mathrm{T}=\mathbf{n}\cdot\mathrm{S}, \tag{20}$$

where the fluid traction is given by (11). This condition is enforced as a boundary condition to (16), as is discussed further in Sec. 3.2.2.3.4.

To couple the solid deformation into the fluid mechanics to preserve mass conservation, we expand the normal component of the boundary velocity,

$$\mathbf{B}_{i,n}=\mathbf{n}\cdot\mathbf{u}|_{z=h_i}+\frac{\partial h_i^0}{\partial t}+\mathbf{n}\cdot\dot{\mathbf{d}}. \tag{21}$$

Here, the first term on the right represents flow through the boundary (for a porous boundary), the second term is any prescribed motion of the boundary, and the third term is the motion of the surface due to deformation of the adjoining solid, where $\dot{\mathbf{d}}$ is the time-derivative of the displacement vector of the solid. The height function used in the lubrication equations can also be expanded to

$$h=h_1-h_2-\mathbf{n}\cdot\mathbf{d}. \tag{22}$$

The application of (20) and (22) comprises the complete, two-way coupling necessary to study fluid-structural interactions.

3.2.2.3 Numerical formulation

The governing equations of Sec. 3.2.2.2 are implemented into the computer code GOMA [Schunk et al. (2006)], which utilizes the Galerkin finite element method (G/FEM) with fully-coupled Newton iterations to solve steady-state and transient problems. This implementation uses isoparametric, hexahedral continuum elements for the three-dimensional structural regions with tri-linear (Q1) Lagrange interpolation functions and isoparametric quadrilateral shell elements (described in Sec. 3.2.2.3.1) with bi-linear (Q1) Lagrange interpolation functions. Numerous linear solvers may be utilized, including direct (LU) and iterative (GMRES) algorithms deployed from a third party library [Heroux et al. (2003)]. Transient problems can be advanced in time with either the backward Euler method or the trapezoidal method.

In this section, we discuss the numerical implementation of our multiphase lubrication model. First, our implementation of a curvilinear shell coordinate system is discussed in Sec. 3.2.2.3.1. We then apply a balanced-force level-set method to track the fluid interface in Sec. 3.2.2.3.2. The implementation of the lubrication governing equations of Sec. 3.2.2.2 is discussed in Sec. 3.2.2.3.3. Finally, fluid-structural interactions are discussed in Sec. 3.2.2.3.4.

3.2.2.3.1 Curvilinear shell formulation

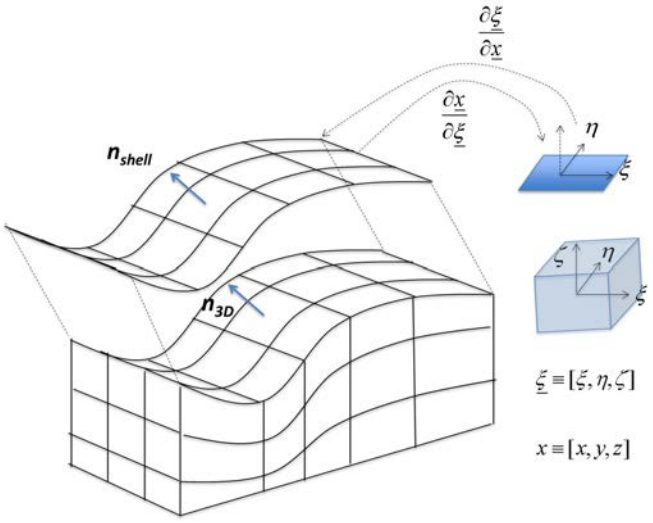

Figure 44: Cartoon of a continuum-element region and adjoining shell-element region, with the necessary isoparametric transformations.

Implementing generalized shell-element constructs in an existing finite element framework without prior forethought can be difficult. Curved shell elements in are in fact specialized (degenerate) continuum finite elements attributed with three spatial coordinates per node. However, integrations required in forming the discretized system of equations (such as (7)) are performed in generalized curvilinear coordinates with only two components (cf. Fig. 44). Integration is typically facilitated by mapping the three-dimensional, curved element into a two-dimensional unit square, as shown in the Fig. 44.

The Jacobian of the mapping, J, is defined as

$$\mathrm{J} = \frac{\partial \mathbf{x}}{\partial \boldsymbol{\xi}} = \begin{bmatrix} \frac{\partial x}{\partial \xi} & \frac{\partial x}{\partial \eta} & \frac{\partial x}{\partial \zeta} \\ \frac{\partial y}{\partial \xi} & \frac{\partial y}{\partial \eta} & \frac{\partial y}{\partial \zeta} \\ \frac{\partial z}{\partial \xi} & \frac{\partial z}{\partial \eta} & \frac{\partial z}{\partial \zeta} \end{bmatrix}. \tag{23}$$

This Jacobian is used for a plethora of tasks in finite element algorithms. First, the most common use is in transforming the integration space from physical coordinates to computational coordinates, or the isoparametric mapping. It is also used to transform gradient operators to physical space and to compute mesh motion sensitivities for our full-Newton-Raphson matrix solver implementation [Sackinger et al. (1996)].

Transforming gradient operators and computing mesh sensitivities require computation of the inverse of the Jacobian, J^{-1}, which is defined only if the Jacobian is of full-rank (not singular). Further explanation of how this is ensured for shell elements is warranted.

In the finite element method, weighted residuals are computed by integrating the equations over the entire domain, but weighted by basis functions. The integration procedure is facilitated most commonly in the isoparametric domain, which means that the Jacobian is computed by using the same interpolation function representation for the nodal coordinates as is used for the dependent variables. That is, all dependent variables and the mesh are computed at any integration point in the mesh as

$$\mathbf{x}^h \equiv \sum_i \mathbf{x}_i \phi_i(\xi) \tag{24}$$

$$p^h \equiv \sum_i p_i \phi_i(\xi) \tag{25}$$

Here, $\xi = [\xi, \eta, \zeta]$ represents the vector basis in the isoparametric domain (see Fig. 44), $\mathbf{x}_i$ are the nodal coordinates, p_i the nodal values of the lubrication pressure, and $\mathbf{x}^h$ and p^h are the finite-element representations of these quantities. These operations can be performed during integration in isoparametric space. The Jacobian J is simply computed as

$$\mathrm{J} = \frac{\partial \mathbf{x}}{\partial \xi} = \sum_i \mathbf{x}_i \frac{\partial \phi_i}{\partial \xi}. \tag{26}$$

Thus, computing quantities such as ∇_{II} follow the chain rule,

$$\nabla_{\mathrm{II}} = (\mathrm{I} - \mathbf{nn}) \cdot \nabla = (\mathrm{I} - \mathbf{nn}) \cdot \mathrm{J}^{-1} \cdot \nabla_{\xi}, \tag{27}$$

where ∇_{ξ} is the gradient in terms of the surface isoparametric coordinates.

If we arbitrarily define the isoparametric ζ-integration direction as that normal to the shell element, as shown in Fig. 44, then difficulties arise in computing the inverse of this matrix for shell elements as the third column of J is zero, viz. there are no sensitivities to ζ as the element is degenerate. In other words, J is singular, thus preventing its inversion and the computation of surface gradients and related quantities. In the structural mechanics community, shell elements are derived with a continuum-based approach that circumvents this problem by effectively defining a finite thickness to the element while accommodating some key structural responses to the shell [Belytschko et al. (2000)]. Because shell elements for lubrication only depend on the kinematics of the element and not the structural stresses, we are free to take a simpler approach.

When we assemble equations in the shell, we construct J (23) by arbitrarily choosing random finite numbers for the third-column components, $[\frac{\partial x}{\partial \zeta}, \frac{\partial y}{\partial \zeta}, \frac{\partial z}{\partial \zeta}]$. We found it best to choose floating point numbers of order unity. It is straight forward to show that the resultant projection

$\nabla_{II} = (\mathrm{I} - \mathbf{nn}) \cdot \mathrm{J}^{-1} \cdot \nabla_{\xi}$ is unaffected by this manipulation of J, so long as the chosen values do not in turn create a singular matrix.

Shell element implementations also lead to other non-standard challenges in computational geometry. As is evident in the equations and boundary conditions of Sec. 3.2.2.2, normal vectors to the shell element face are required. Similar to the pathologies with computing inverse mappings, we used the same tactics to compute normal vectors if the shell elements have no bounding (attached) three-dimensional regions. Normal vectors to shell elements which are attached to continuum element regions can be simply computed using standard approaches, calculating the surface normal of the attached continuum element.

3.2.2.3.2 Balanced-force level-set method

In order to track the location of the interface between two phases, we utilize a level-set algorithm based on a balanced-forces approach [Francois et al. (2006), Herrmann (2008)]. In this method, a distance function f is introduced, where $f = 0$ is the location of the interface between the two fluids, $f < 0$ represents fluid a, and $f > 0$ fluid b. The value of f at any point approximates the shortest distance from that point to the interface. The movement of f is governed by an advection equation,

$$\frac{\partial f}{\partial t} = -\bar{\mathbf{u}} \cdot \nabla_{II} f, \tag{28}$$

where $\mathbf{u}$ is the material velocity field. For lubrication problems, we advect the level-set field with the mean lubrication velocity field $\bar{\mathbf{u}}$, given by (5). For use in our G/FEM scheme, (28) is integrated to obtain the residual equation

$$\int_{\Omega} \phi_i \left[\frac{\partial f}{\partial t} + \bar{\mathbf{u}} \cdot \nabla_{II} f \right] d\Omega = 0. \tag{29}$$

In this, and other, residual equations, Ω is the computational domain and Γ represents a surface or boundary. Because (28) does not maintain f as a distance function as it is advected, f must be renormalized occasionally. This renormalization is done using a constrained Huygens method, which employs a Lagrange multiplier to enforce conservation of the liquid phase before and after renormalization. Renormalization occurs when $\nabla_{II} f$ differs significantly from unity at any time step, based on a specified tolerance.

With the distance function f, we can define a Heaviside function which is to be evaluated only at node points,

$$H_i = \begin{cases} 1 & f_i < 0 \\ 0 & f_i > 0 \end{cases}. \tag{30}$$

This Heaviside may be made continuous by interpolating using the standard G/FEM basis functions,

$$H = \sum_i \phi_i H_i, \tag{31}$$

which yields a function that is sharp, i.e. is only real (neither 0 or 1) within an element that contains the level-set interface, $f = 0$. For numerical ease, however, one may wish to adopt the approach used in traditional level-set methods of creating a smooth Heaviside function. Here, we can replace (30) with the smooth representation

$$H_i = \begin{cases} 0 & f_i < -\alpha \\ \frac{1}{2}\left(1 + \frac{f_i}{\alpha} + \frac{\sin(\pi f_i / \alpha)}{\pi}\right) & -\alpha \le f_i \le \alpha, \\ 1 & f_i > \alpha \end{cases} \tag{32}$$

where α is the width of the smooth level-set region. Physical properties, such as the viscosity and density, may now be expressed as a continuous value across phases by using the Heaviside function,

$$\beta = \beta_a + (\beta_b - \beta_a)H, \tag{33}$$

where β is a continuous physical property and β_i are the discrete properties in phase i.
As introduced in Sec. 3.2.2.2.2, the Young-Laplace equation [Batchelor (2000)] is included in the lubrication equations using the continuum surface force (CSF) method [Brackbill et al. (1992)], which defines the classic expression of the CSF vector

$$\mathbf{F}_{\text{CSF}} = \sigma\kappa\mathbf{n}_{ab}\delta. \tag{34}$$

In this expression, δ is the Dirac delta function representing the location of the interface. In the balanced-forces approach [Francois et al. (2006)], we want to represent pressure jump generated by (34) in the same vector space as the pressure appears in the equation, namely as the gradient of a function (pressure). Recognizing that $\nabla H(f(\mathbf{x})) \approx \delta(f(\mathbf{x}))\mathbf{n}$, we can follow the lead of Ref. [Francois et al. (2006)], reformulating the CSF tensor as

$$\mathbf{F}_{\text{CSF}} = \sigma\kappa\nabla_{\text{II}}H. \tag{35}$$

When this formulation is then integrated into the flow rate expression, (12) becomes

$$\mathbf{q} = -\frac{h^3}{12\mu}\left(\nabla_{\text{II}}p - \rho\mathbf{g} + \sigma\kappa\nabla_{\text{II}}H\right) + \frac{h}{2}(\mathbf{B}_{1,\text{II}} + \mathbf{B}_{2,\text{II}}). \tag{36}$$

This formulation illustrates how the pressure p and the level-set field (through H) enter the equation in the same manner and vector space. For this calculation, the smoothed Heaviside function (32) is used.

Calculation of the curvature κ shown in (36) is based on the formulation discussed in Sec. 3.2.2.2.2. While the curvature normal to the flow direction is calculated analytically with (14), the curvature in the flow direction must be calculated numerically. The normal vector for the interface is evaluated directly from the level-set field

$$\mathbf{n}_{ab} = \frac{\nabla_{\text{II}}f}{|\nabla_{\text{II}}f|}. \tag{37}$$

The curvature equation (15) is then integrated by parts to arrive at the residual formulation

$$\int_\Omega \phi_i \kappa_{\mathrm{II}} d\Omega + \int_\Omega \nabla_{\mathrm{II}} \phi_i \cdot \mathbf{n}_{ab} d\Omega = 0. \tag{38}$$

This finite element formulation, however, can suffer from numerical instability issues. To combat this, two approaches are taken. First, the curvature term is effectively mass-lumped, evaluating it only at the nodes. Secondly, artificial diffusion is added to smooth out small perturbations in the curvature field [Olsson et al. (2007)]. These modifications to (38) yields the final expression

$$\kappa_{\mathrm{II}} \int_\Omega \phi_i d\Omega + \int_\Omega \nabla_{\mathrm{II}} \phi_i \cdot \mathbf{n}_{ab} d\Omega + \int_\Omega h^2 \nabla_{\mathrm{II}} \phi_i \cdot \nabla_{\mathrm{II}} \kappa_{\mathrm{II}} d\Omega = 0, \tag{39}$$

where h^2 in this expression is a scaling factor representing the element area.

3.2.2.3.3 Lubrication flow implementation

Reynolds' lubrication equation is implemented in our FEM model by integrating (7) by parts, yielding the residual equation

$$\int_\Omega \phi_i \left[-\mathbf{B}_{1,\mathrm{II}} \cdot \nabla_{\mathrm{II}} h_1 + \mathbf{B}_{2,\mathrm{II}} \cdot \nabla_{\mathrm{II}} h_2 - \mathbf{n} \cdot (\mathbf{B}_{1,\mathrm{n}} - \mathbf{B}_{2,\mathrm{n}}) \right] d\Omega + \int_\Omega \nabla_{\mathrm{II}} \phi_i \cdot \mathbf{q} d\Omega = 0. \tag{40}$$

For multiphase simulations, the flow rate $\mathbf{q}$ is calculated using (36) in conjunction with (29) and (39), otherwise (8) can be used without additional equations.

Because of the elliptic nature of (40), conditions are necessary at each boundary to complete the problem description. The simplest case is the Neumann condition, which may be obtained for free (i.e. without further manipulation of the residual at the boundaries). This condition is equivalent to a no flow condition, $\mathbf{N} \cdot \mathbf{q} = 0$ on a boundary, where $\mathbf{N}$ is the normal of that boundary. This condition is useful for solid boundaries. Another common condition is the Dirichlet condition, which strongly sets the pressure at boundary nodes to a set value, $p = C$. This condition is useful for specifying atmospheric conditions or specifying a flow profile through the geometry.

3.2.2.3.4 FSI implementation

Two steps are required to enforce the full fluid-structural couplings discussed in Sec. 3.2.2.2.4. First, (20) must be applied to the solid at its boundary with the lubrication region. This results in the residual equation at the boundaries,

$$\int_\Gamma \phi_i \left[\mathbf{n} \cdot \mathrm{T} - \mathbf{n} \cdot p - \frac{\mu}{h} \left(\mathbf{B}_{1,\mathrm{II}} - \mathbf{B}_{2,\mathrm{II}} \right) \right] d\Gamma = 0, \tag{41}$$

which imposes the fluid stress on the solid. Second, (21) is applied directly as discussed in Sec. 2.4. No additional equation or boundary conditions are necessary for this coupling, as h is directly included in the lubrication equation via (22).

3.2.2.4 Numerical results

In this section, we show a number of numerical examples to demonstrate the capabilities of our model. Results are compared to both analytical solutions and experimental results. To test the correct calculation of the interface curvature using level-set fields and the resulting pressure

jump, we show calculations for a static liquid drop confined between two plates in Sec. 3.2.2.4.1 and compare to the analytical solution for the pressure. Next, the accuracy of the level-set algorithm for transient problems is addressed in Sec. 3.2.2.4.2 by comparing to the analytical solution for a liquid drop between plates being squeezed together. In Sec. 3.2.2.4.3, we then compare our calculations to experiments of capillary liquid rise between two plates at a small angle. Finally, we demonstrate our curvilinear coordinate system through the computation of the pressure distribution in a journal bearing in Sec. 3.2.2.4.4 and compare to the analytical values.

3.2.2.4.1 Static confined liquid drop

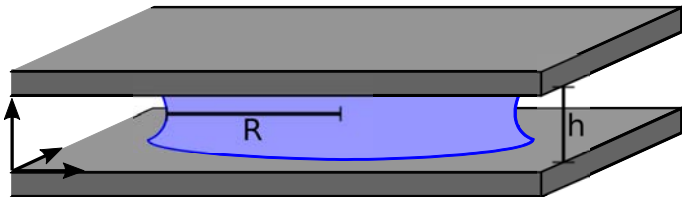

Figure 45: Illustration of a static liquid drop confined between two parallel plates.

A liquid drop confined between two parallel plates is illustrated in Fig. 45. If both plates are held in place, the drop will remain static. Because of the presence of the free interface, the pressure inside the drop will differ from the external pressure, and this pressure jump can be calculated analytically from (9,13-15) with the viscous stress terms removed. If the drop is circular with radius R_{drop}, the outside of the drop is at atmospheric pressure, and the plates have the same contact angle, (9,13-15) can be simplified, resulting in an analytical solution for the pressure inside the drop,

$$p = \sigma\left(-\frac{2}{h}\cos(\theta) + \frac{1}{R_{drop}}\right). \tag{42}$$

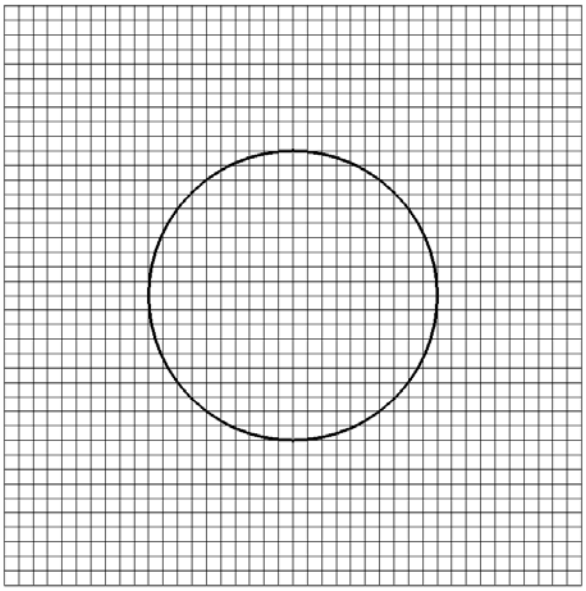

Figure 46: Mesh used for static drop example Sec. 3.2.2.4.1, with the outline of the level-set field used to denote the liquid-air interface drawn atop.

Static drop simulations are performed on a planar, 2-D mesh of shell elements, shown in Fig. 46. The level-set field is initialized with a circle of radius R_{drop}, which is also shown in Fig. 46.

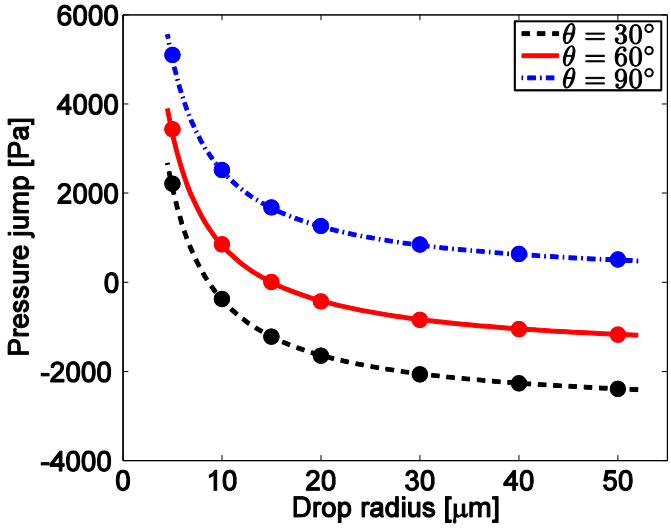

Figure 47: Validation of pressure jump in middle of a static drop, compared to the analytical solution of (42) (solid lines). Physical parameters are $h = 15\mu\text{m}$, $\sigma = 25\text{mN/m}$, $\theta_1 = \theta_2 = 30^\circ$. Domain width is 4x drop radius and the mesh has 40x40 elements.

Numerical simulations of this configuration were performed for varying contact angles and drop radii and are compared with (42) in Fig. 47. At large drop radii, the curvature in the flow direction, κ_{II}, is much less significant than the curvature in the normal direction, κ_z, making the drop pressure relatively insensitive to changes in the drop radius. However, once the drop radius becomes similar to the plate height ($h = 15\mu\text{m}$), the pressure becomes quite sensitive to the radius, increasing rapidly as the drop radius decreases. These two curvatures have competing effects; the positive curvature in the flow direction causes a higher pressure in the drop, while the negative curvature in the normal direction (due to the wetting contact angles) causes a decreased drop pressure. In all of these cases, the results of our simulations show excellent agreement with (42).

3.2.2.4.2 Spreading confined liquid drop

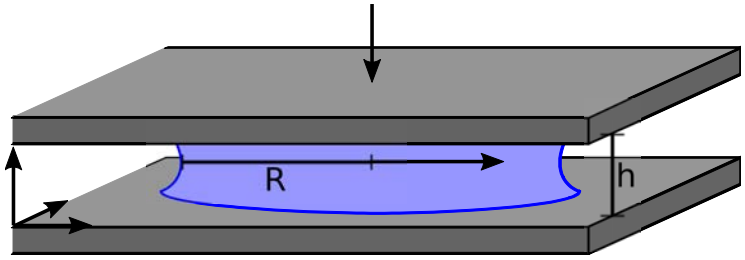

Figure 48: Illustration of liquid drop confined between two parallel plates, where the top plate is moving downward with a constant velocity.

When the parallel plates confining a liquid drop are squeezed together, as in Fig. 48, the problem becomes inherently transient, as the drop must spread between the plates and the pressure profile changes with time. In this section, we address two versions of this problem. First, we assume that the squeezing velocity is constant and compare to an analytical solution (Sec. 3.2.2.4.2.1). Second, a variable squeezing rate is obtained from experimental images, and simulations are performed to compare to these images (Sec. 3.2.2.4.2.2).

3.2.2.4.3 Constant squeezing rate

The problem of a drop being squeezed between two plates at a constant velocity was analytically solved by Chauhan et al. [Chauhan et al. (2009)] who arrived at the solution

$$P(r,t) = P_{\text{atm}} - \frac{\sigma}{h(t)}\left(\cos(\theta_1)+\cos(\theta_2)\right) + \frac{-3\mu W_1}{h(t)^3}\left(R(t)^2 - r^2\right), \tag{43}$$

$$R(t) = R(0)\sqrt{\frac{h(0)}{h(t)}}, \tag{44}$$

$$u_r(r,z,t) = \frac{3W_1 r}{h(t)^3}(z^2 - h(t)z), \tag{45}$$

$$w(r,z,t) = \frac{6W_1}{h(t)^3}\left(\frac{h(t)z^2}{2} - \frac{z^3}{3}\right). \tag{46}$$

In (43-46), P_{atm} is the atmospheric (external) pressure, $R(t)$ is the drop radius at time t, r is the radial coordinate, u_r is the radial velocity, and w is the z-velocity. Under the lubrication approximation, we use a height-averaged velocity, which may be calculated by integrating (45) over the drop height. This results in an average radial velocity

$$\bar{u}_r(r,t) = -\frac{h(t)rW_1}{2}. \tag{47}$$

The expressions for drop pressure (43) and radius (44) remain unchanged.

Simulations were carried out using a mesh similar to the previous example (Fig. 47). The level-set field was initialized with a circle of radius $R(0)$. The simulation was transient, with a time step of $\Delta t = 5\mu\text{s}$, and the simulation was run until the drop nearly reached the edge of the domain. The plate velocity W_1 was directly imposed by setting $B_{1,N} = W_1$ and the interface height is calculated as $h(t) = h(0) + W_1 t$.

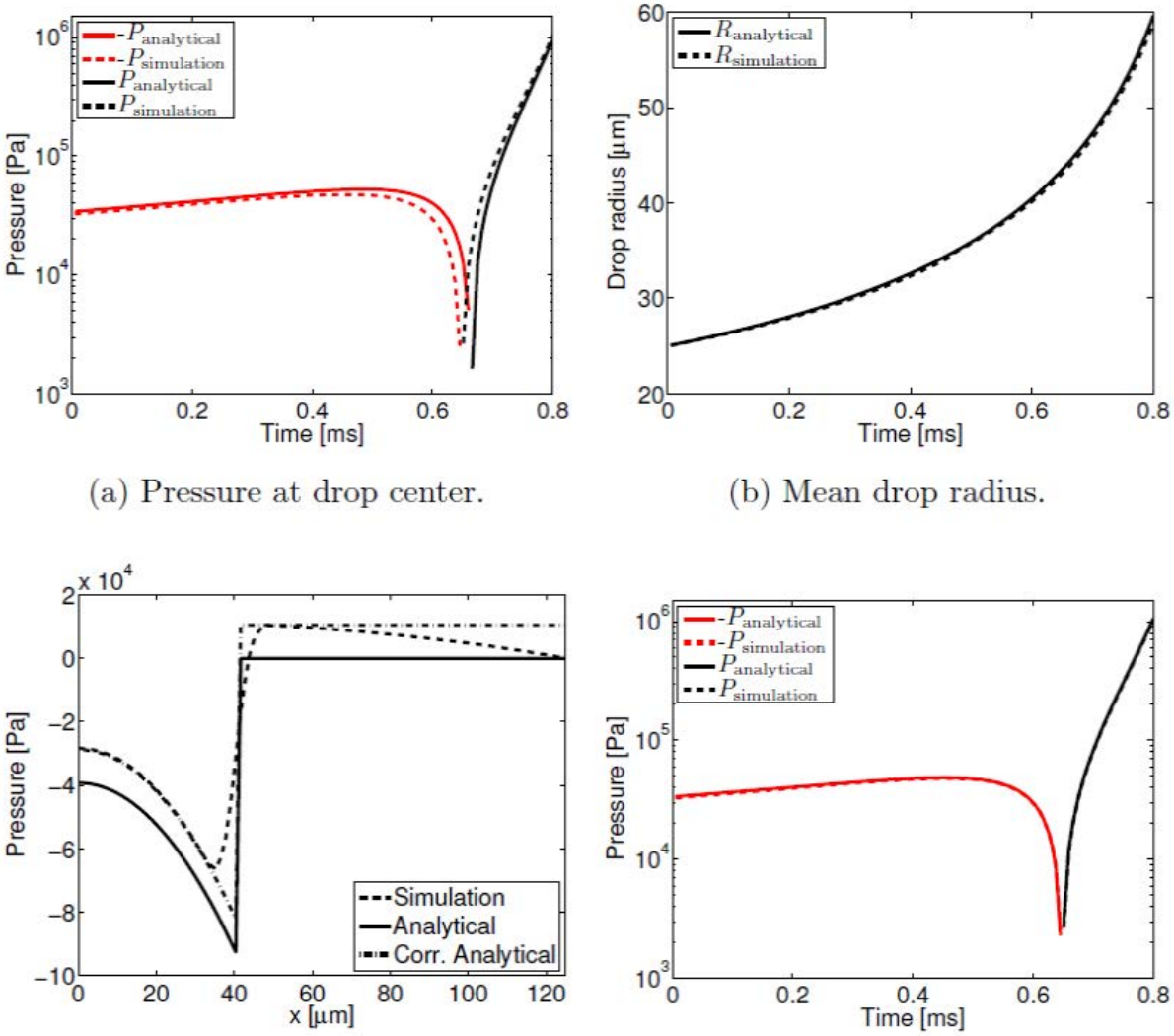

(a) Pressure at drop center.

(b) Mean drop radius.

(c) Pressure profile at drop mid-plane, $t = 6.03 \times 10^{-4}$ s. Drop edge is at $x = 40.3\,\mu$m.

(d) Pressure at drop center, corrected for external pressure.

Figure 49: Comparison of simulations in Sec. 3.2.2.4.2 of a spreading drop with the analytical solution (43--47). Calculations are for a water drop with air as the surrounding fluid. Initial drop radius is $R(0) = 25\mu$m and the domain width is $10R(0)$, with a 120×120 element mesh. Other physical parameters are $h(0) = 1.32\mu$m, $\sigma = 25$mN/m, $\theta_1 = 30^\circ$, $\theta_2 = 5^\circ$, $W_1 = -1.36$mm/s.

A numerical comparison of our model to this analytical solution is shown in Fig. 49. At early times in the simulation, the pressure at the center of the drop is negative, as shown by the red curves in Fig. 49, due to the pressure drop across the drop interface from the wetting contact angle. As the top plate continues to lower, pressure builds up in the center of the drop, which leads to spreading of the drop. The increasing pressure can be observed in Fig. 49, as pressure

begins increasing exponentially, becoming positive at $t \approx 0.6\text{ms}$. Fig. 49 shows the increasing drop radius through time, which matches nearly exactly with the analytical solution (44).

The drop pressure comparison shown in Fig. 49, however, shows slight positive deviation from the analytical solution (43), with the difference between the calculated and the analytical pressures growing over time. This apparent systematic error can, in fact, be attributed to a simplification in the analytical solution, which ignores any dynamics of the surrounding gas phase. This discrepancy can be clearly seen in Fig 49, which shows the pressure as a function of the radial coordinate for the analytical (solid) and computed (dashed) solutions. Outside of the drop, the computed solution exhibits a slight pressure gradient which must be present in order for the gas to flow out from between the plates. The analytical solution (43) may be corrected for this pressure gradient by using the maximum air pressure value from the computed solution as P_{atm}, which is also shown in Fig. 49 as the dot-dash curve. Correcting the analytical solution at each time plane leads to much better agreement between the computed and analytical pressures at the drop center, as shown in Fig. 49.

3.2.2.4.4 Variable squeezing rate

In this section, we compare simulations with and without fluid-structural interactions of a liquid drop being squeezed with an arbitrary velocity to results obtained from image analysis of an experimental video as well as an analytical solution. A slow motion video [Singhal and Sreenivasan (2011)] was taken of liquid drops spreading under a transparent substrate at 500 frames per second. Several drops were analyzed in Matlab [The MathWorks Inc.] to determine their radius and height versus time. Each frame of the movie was first cropped to show only a single drop, and the frame was filtered using a FIR filter implemented in Matlab [The MathWorks Inc.]. The filtered images were then thresholded automatically using Otsu's method [Otsu (1979)] to obtain the drop shape. The radius was obtained by measuring the area of the drop from the thresholded image and then calculating the radius, assuming the drop was circular. The data for the height was fit to a third order polynomial in time for use as the height function in the computational models. All drops had an initial radius of 25 μm and an initial height of 1.32 μm [Singhal and Sreenivasan (2011)].

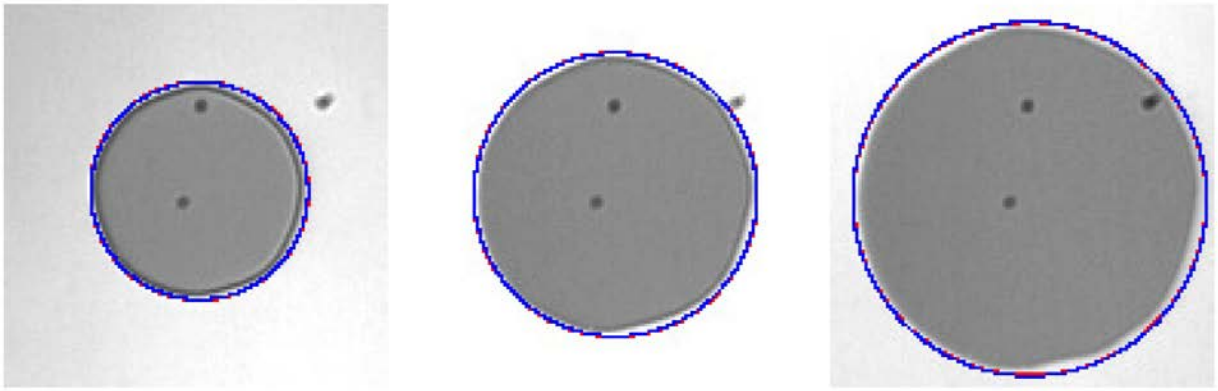

(a) $t = 0.06$ s (b) $t = 0.12$ s (c) $t = 0.18$ s

Figure 50: Snapshots of experimental images of a drop spreading under a variable squeezing rate [Singhal and Sreenivasan (2011)]. The blue line is the drop outline calculated from the direct lubrication model, while the red line is from the coupled FSI model.

A single drop was chosen for this analysis. Three snapshots of this drop are shown in Fig. 50. This drop sequence was produced with a squeezing velocity of

$$W_1(t) = -13.6 + 65.9t - 126.9t^2 \tag{48}$$

with W_1 in μm/s and t in seconds. The correlation is depicted in Fig. 51, showing that the experimental data and correlation are in good agreement.

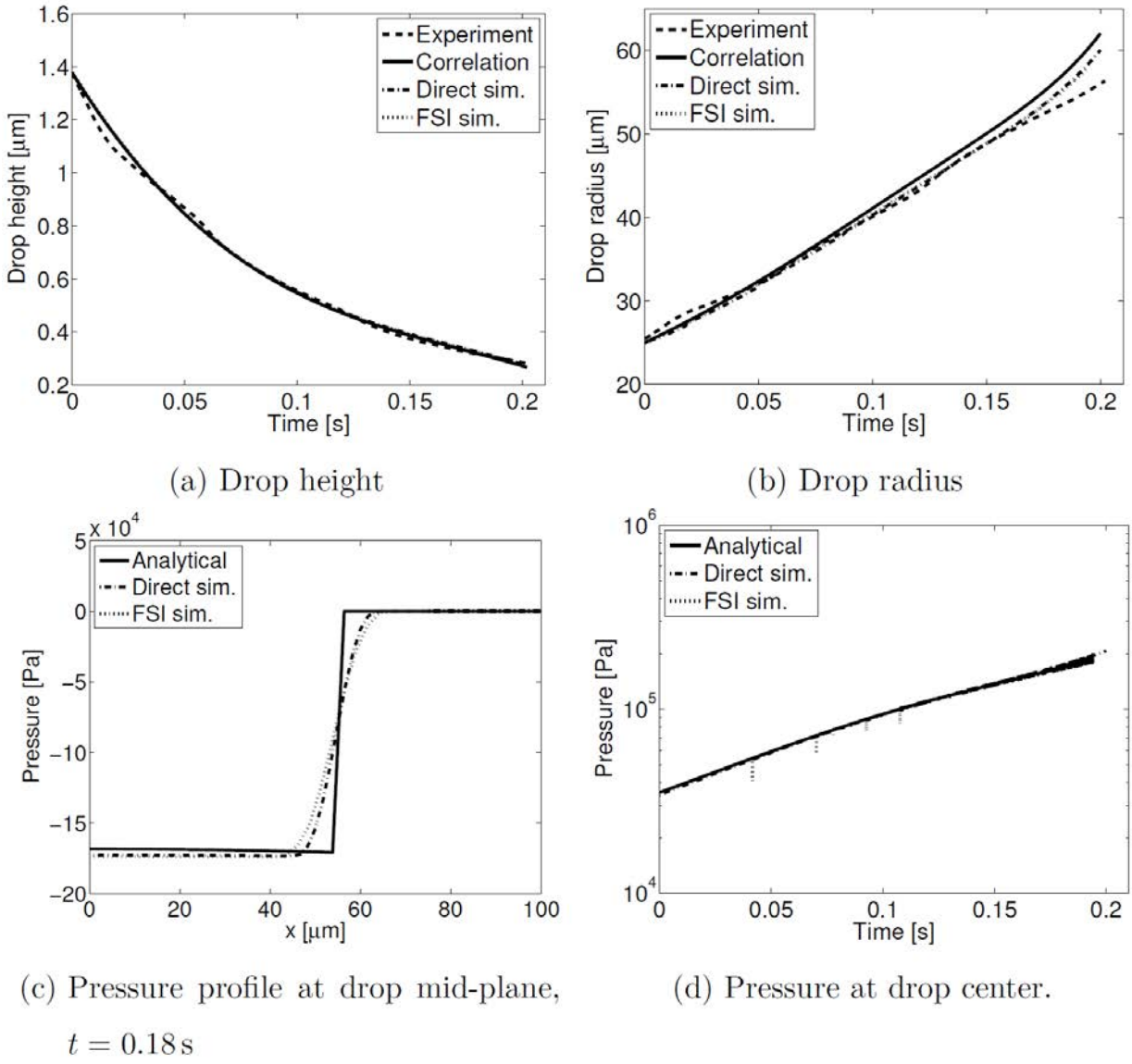

Figure 51: Data for simulations in Sec. 3.2.2.4.2.2 and analytical results. When shown, experimental results are represented by a dashed line, correlations and analytical solutions are a solid line, simulations with the direct model are a dot-dash line, and simulations with the FSI model are a dotted line.

While the analytical solution discussed in Sec. 3.2.2.4.2 (43--46) was originally derived for a constant squeezing velocity, it is equally valid for a time-dependent velocity, $W_1(t)$, such as the one fit from the experimental images. Therefore, simulations are compared to both the experimental and analytical results in Fig. 51.

Simulations of this system were run using two different computational models. First, the lubrication-only model from Sec. 3.2.2.4.2 was used with the squeezing rate (48). The other simulation utilizes the fluid-structural interaction capability discussed in Sec. 3.2.2.3.4. This simulation consists of a mesh similar to Fig. 46, but with the addition of an adjoining continuum

solid region. For these simulations, the solid thickness was 1 mm with Lame parameters of $\mu = 3.1\times10^{8}\,\text{dyne/cm}^2$ and $\lambda = 2.0\times10^{8}\,\text{dyne/cm}^2$. There was no observable deflection of the solid due to the relatively high values of the Lame parameters compared to the peak fluid pressures observed. For the remainder of this discussion, we refer to the first, lubrication-shell-only, simulation as the ``direct'' simulation, while the second one will be notes as the ``FSI'' simulation.

Overall the simulation results showed strong agreement with the experimental results as well as the analytical solution. Fig. 51 shows the edge of the drop, calculated using both simulation methods, superimposed atop the experimental images at three time frames. Good agreement is observed, with a lightly larger radius shown for the simulations. This deviation can be attributed to inaccuracies in the thresholding of the images.

Other simulation metrics are compared to the experiments in Fig. 51, e.g. the top shows the drop height and radius. The drop height matches very well for all times, while there are slight deviations in the calculated radius at longer times. These deviations can be attributed to errors in the velocity fit to experimental data, also shown in the top half of Fig. 51. Good agreement is also shown in the pressure field, shown in bottom half. The abnormal spikes visible in the pressure fluctuations that occur when the level-set field is renormalized, and they are resolved in the next time step. The pressures profiles of the two simulations match each other well outside of the level-set region; however, they do not match the analytical pressure profile quite as strongly.

These two example problems show that our multiphase lubrication model is very capable of modeling transient flows of thin, confined films. This example also shows that under proper conditions, the direct and FSI models give similar results, proving that coupled lubrication-solid simulations can be used to study more complicated problems.

3.2.2.4.5 Liquid front rising between plates with small angle

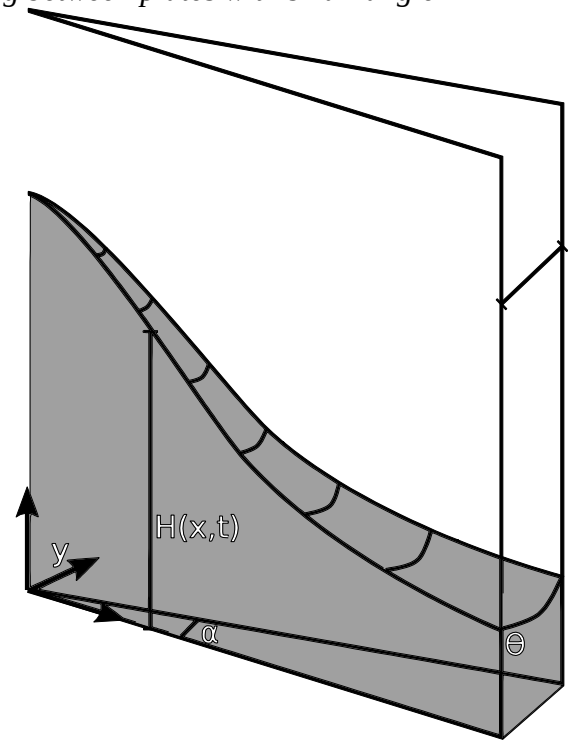

Figure 52: Illustration of two vertical plates making a small angle, α, inserted into a pool of liquid. Capillary forces draw the liquid into the plates, yielding a height profile $H(x,t)$.

Many science instructors use the rise of a liquid in a tube of small diameter as an example of capillary forces. In this example, a wetting liquid rises in the tube due to the negative capillary pressure generated from the fluid-air interface. This rise is slowed by gravity, however, the liquid will approach an equilibrium height that can be determined by the tube radius and liquid contact angle.

A significantly more complicated problem involves the capillary rise of a liquid between two plates making a small angle, a setup illustrated in Fig. 52. The small angle made by the plates means that the curvature along the plate width (x-direction) increases, decreasing the capillary pressure jump and therefore changing the equilibrium height of the interface. This problem was recently studied by Higuera et al. [Higuera2008], who observed the interface profile over time in experiments and then compared those results to their asymptotic theory.

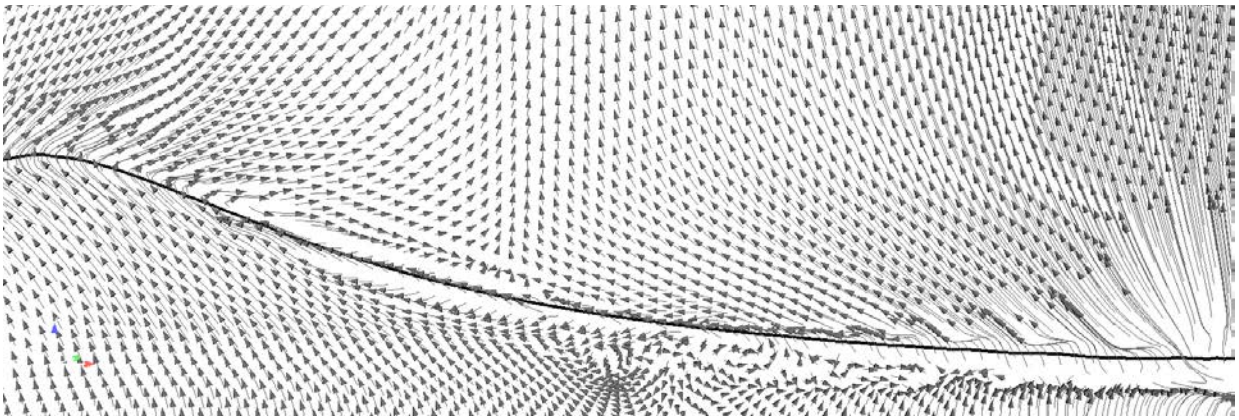

Figure 53: Plot of the velocity vectors at $t = 700\text{s}$ in a simulation of liquid rise between plates. Liquid is a silicone oil, with fluid and geometrical parameters identical to the experiments in Ref. [Higuera2008].

This problem provides a challenging verification of our computational model as it incorporates most of the features we have implemented, including gravitational forces, curvature calculation, and interface tracking. Additionally, the gradient in curvature along the interface at early times induces a very strong shearing flow tangential to the interface, shown in Fig. 53, which requires heightened grid resolution and small time steps to resolve.

For our calculations, we use a rectangular mesh with dimensions and orientation consistent with the experiments in Ref. [Higuera2008]. The mesh is oriented in the $x-z$ plane, and gravity acts in the $-z$ direction. The top ($z = 20\text{cm}$) and bottom ($z = 0\text{cm}$) boundaries are kept at atmospheric pressure, while no-flow conditions are applied on the vertical boundaries. The domain is resolved with a 300×300 element mesh and the level-set field is initialized with the interface at $z = 0.5\text{cm}$.

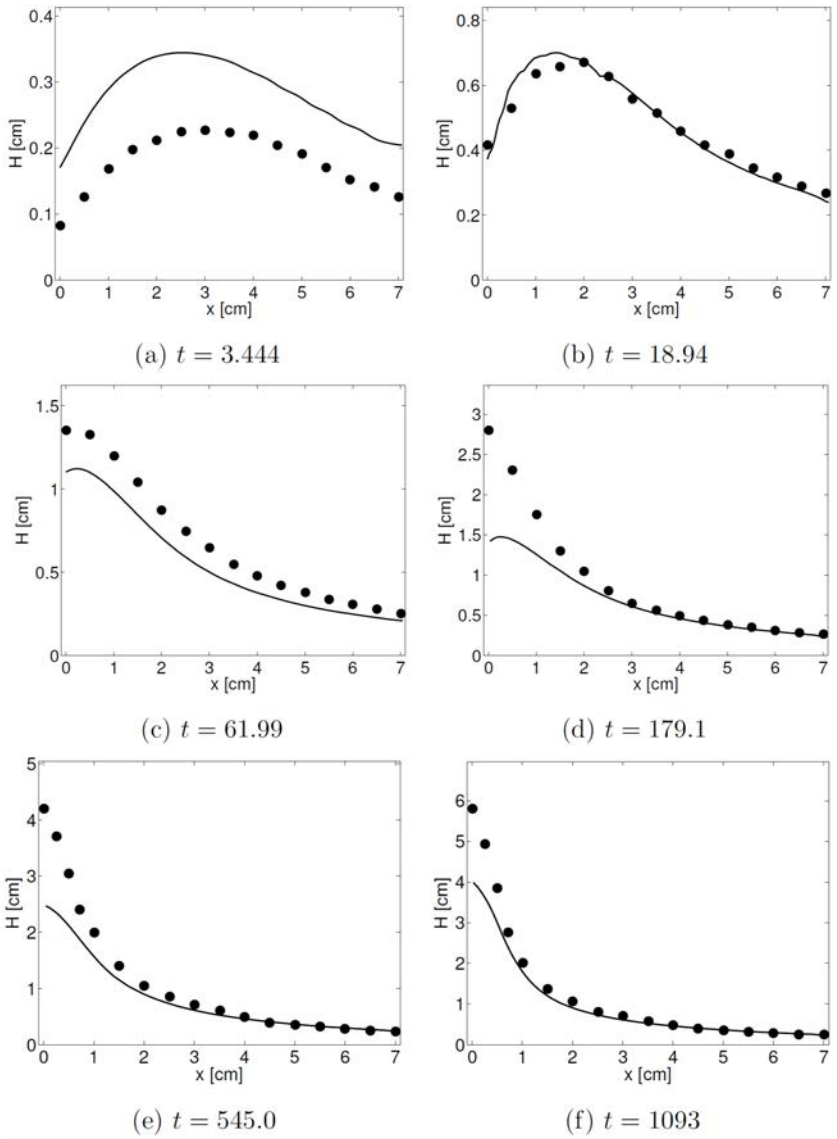

Figure 54: Direct comparison of interface profiles at six time points from computation (solid lines), compared with experiments (data points) [Higuera2008]. Fluid and geometrical parameters are identical to the experiments in Ref. [Higuera2008].

Fig. 54 shows a comparison between our calculations and experiments [Higuera2008]. The calculations, shown as the solid line, show good qualitative agreement with the experimental results, yielding consistent interface shapes at each of the time steps shown. At very early times, shown in Fig. 54, the interface profile is matched nearly perfectly, yet the calculated solution is higher than seen in the experiments. This disparity may arise because our simulations cannot start with the interface exactly at $H = 0$, as there would be no fluid in the plates. Additionally, measurement error may exist in the experiments due to the small length scales, possible unknown plate depth, or dynamics of the pool interface. Other discrepancies occur near the left side of the domain, where in the experiments the plate spacing goes to zero. As we cannot achieve that in our simulations, we set a minimum plate spacing of $h = 0.005\text{cm}$. Despite these few quantitative discrepancies, we believe that our model accurately captures the interface

shapes and dynamics observed in experiments, and at long time scales, our model would reach the steady-state configuration.

3.2.2.4.6 Journal bearing

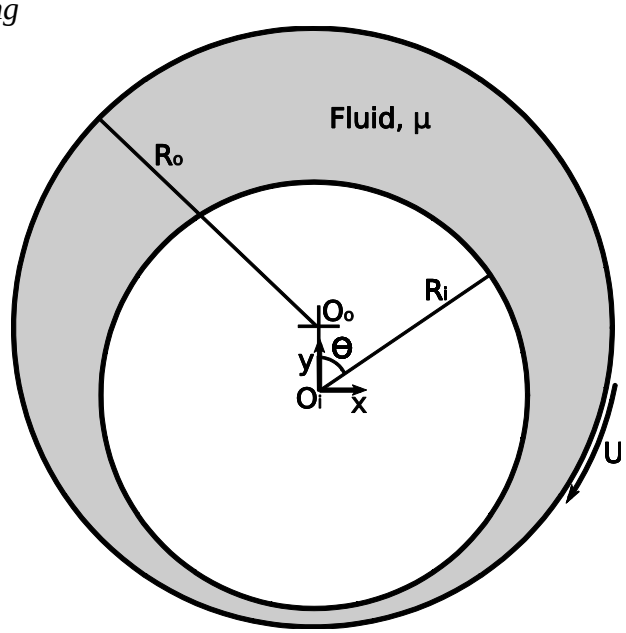

Figure 55: Illustration of a journal bearing. The mean film thickness is $C = (R_o - R_i)/2$ and the eccentricity is $\varepsilon = \| \mathbf{O}_o - \mathbf{O}_i \| / C$.

Journal bearings are a type of fluid bearing used widely in industry to lubricate and support a spinning shaft. A simple journal bearing is illustrated in Fig. 55. The outer bushing supports the load of the shaft due to the lubrication forces generated by the relative rotation. Wada and coworkers [Wada1971] investigated the pressure distribution in journal bearings over four decades ago, and we will use this problem to validate our implementation of lubrication hydrodynamics on curvilinear shell elements into our general finite-element code.

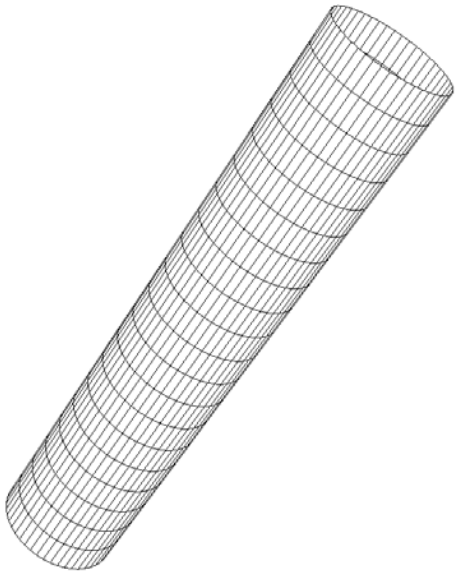

Figure 56: Journal bearing mesh, $n = 48$.

In order to simulate this bearing, a cylindrical solid is generated and a region of shell elements is meshed along the circumference, as shown in Fig. 56. These elements conform to the inner cylinder of the journal bearing. The varying thickness of the lubrication gap, illustrated in Fig. 55, is given as an analytical function as a function of the cylindrical angle, θ, by

$$h(\theta) = C(1 + \varepsilon \cos(\theta)), \tag{49}$$

where C is the mean lubrication film thickness and ε is the eccentricity. This lubrication thickness is applied as a varying h in the lubrication model, as a function of the location around the outside of the cylinder. This implementation of a cylindrical geometry, but computed in a Cartesian coordinates, highlights the power of the curvilinear shell elements, as it allows arbitrary shapes to be meshed with shell elements and used in computations.

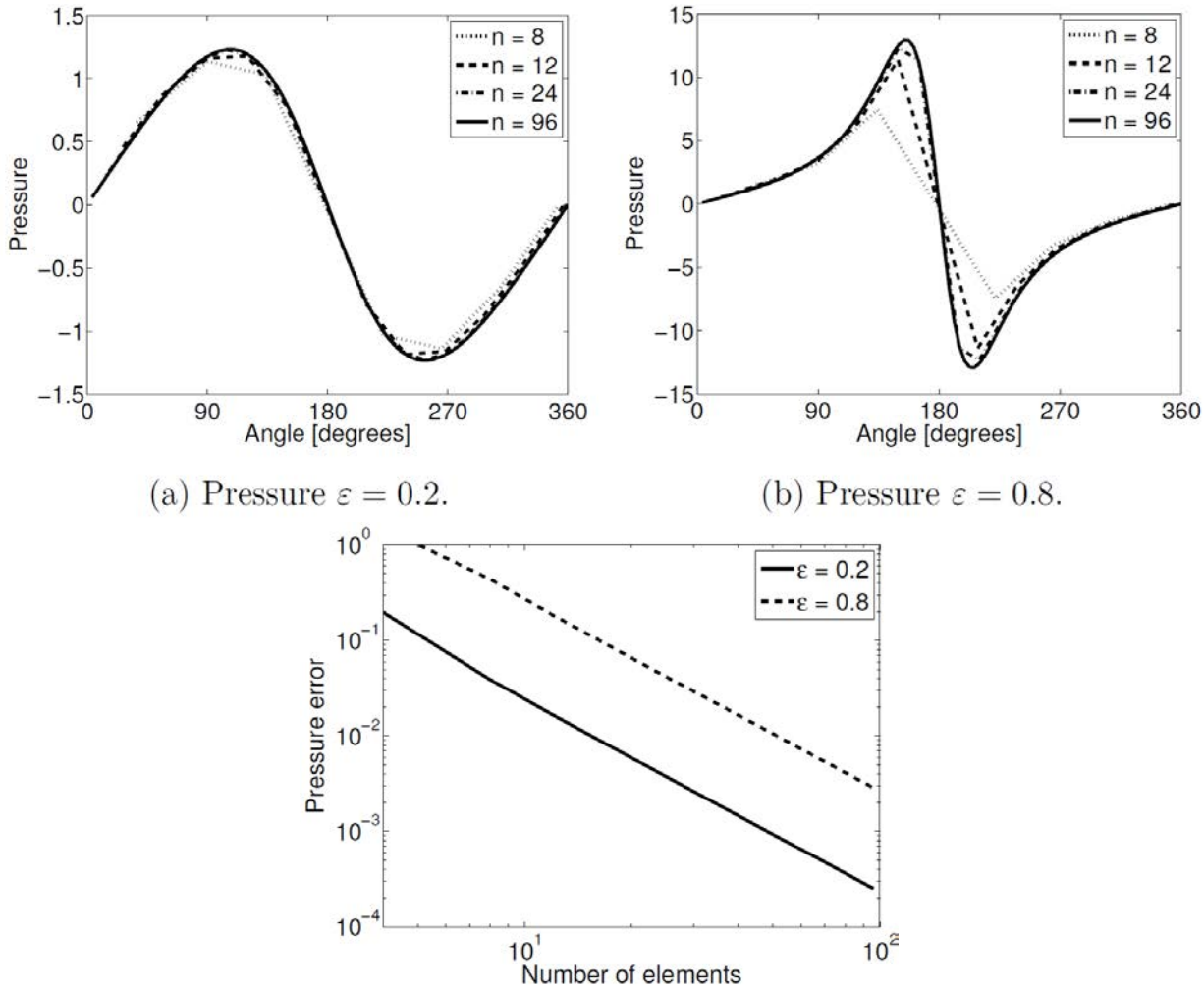

(a) Pressure $\varepsilon = 0.2$.

(b) Pressure $\varepsilon = 0.8$.

(c) Mesh convergence of pressure at $\theta = 90°$. Analytical values are 1.176 for $\varepsilon = 0.2$ and 3.636 for $\varepsilon = 0.8$ [3].

Figure 57: Dimensionless pressure profiles and mesh convergence for a journal bearing. For these simulations, $R_i = 10\text{cm}$, $C = 0.1\text{cm}$, $U = 1\text{cm/s}$, and $\mu = 0.01\text{P}$

Pressure distributions in the lubricating film of the bearing are shown in Fig 57 as a function of number of mesh elements n around the circumference of the cylinder. In all cases, the shape of the pressure distribution is captured qualitatively. However, with fewer elements around the circumference, the maximum and minimum pressures are missed; refining the mesh improves the accuracy in capturing these pressures. As the eccentricity of the system increases, the pressure profile becomes more steep and concentrated towards the bottom of the bearing ($\theta = 180^\circ$). In the case of $\varepsilon = 0.8$, a much more refined mesh is required to accurately capture the shape of the pressure distribution.

Wada et al.[Wada1971] provided analytical solutions for the pressure at $\theta = 90^{\circ}$ with eccentricities $\varepsilon = 0.2$ and $\varepsilon = 0.8$. The convergence of our solution to the analytical values with mesh refinement is shown in Fig. 57. This metric converges quadratically with mesh refinement, with a convergence rate of 2.010 for $\varepsilon = 0.2$ and 1.996 for $\varepsilon = 0.8$.

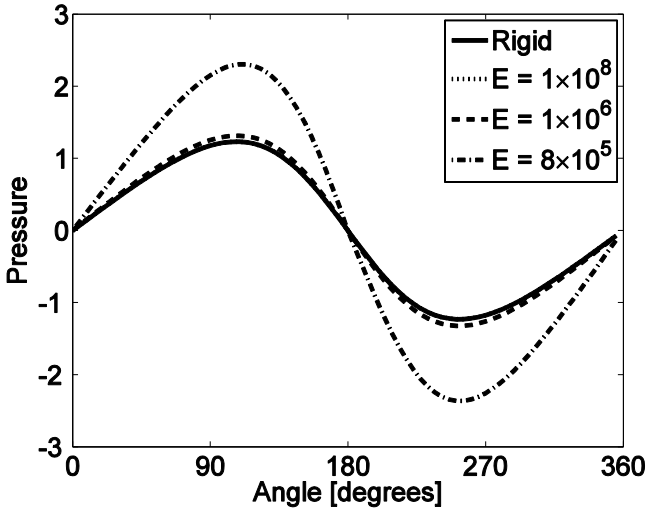

Figure 58: Pressure distribution in journal bearing with a deformable inner cylinder for various values of the bulk modulus.

To further demonstrate the fluid-structural interactions (FSI) between continuum solid elements and shell lubrication elements, the inner cylinder (journal) can be made deformable. In this case, the pressure profile generated by the rotation will be directly coupled to deformation of the journal. The results of these simulations for varying journal moduli are shown in Fig. 58. When the material modulus is sufficiently high, the pressure profile remains identical to the rigid case, as expected. However, when the modulus is lowered, significant deviations from the rigid case are seen. Namely, the pressure extrema are increased as the modulus is lowered, an effect that may be important for high pressure or high velocity systems.

3.2.1 Conclusions

In this chapter we described our efforts in this LDRD project to build interactive models of a nano-imprinting processes which spans the feature scale to the machine/wafer scale. Although we elected not to pursue feature scale models in this project, we made clear what work still needs to be done on that level to allow for defect prediction at the template level. In order to build predictive models at the template level we developed a unique, interactive shell-element capability to allow for expedience in an otherwise intractable three dimensional problem. Together with the shell elements we also developed a pixel/pattern to mapping tool described in section 3.2.1 to facilitate our coarse-graining of pattern representation.

Next, in section 3.2.2 we described an implementation of Reynolds' lubrication theory using shell elements inside a generalized three-dimensional continuum finite-element code. This implementation allows for the application of lubrication theory to a variety of problem, particularly those with complex geometries and with interactions to continuum regions. The lubrication flow equations were augmented with terms for free fluid interfaces, using the balanced-force level-set approach. This multiphase flow model allows for the study of a variety

of industrially relevant problems, such as coating and patterning flows. A continuum solid mechanics model was also coupled to the lubrication flow model, allowing the study of fluid-structural interactions with thin fluid flows.

These capabilities were demonstrated on a number of model problems having analytical or experimental solutions. First, the multiphase flow capability was tested by calculating the pressure drop inside a static, confined drop. Nearly exact simulation of the pressure drop was demonstrated. Next, the level-set tracking and fluid-structural interactions were examined with a drop confined between two moving plates. Analytical solutions and experimental images were used to compare to these simulations, showing excellent agreement. Capillary flow between two vertical plates served as another example problem, and solutions were compared with other numerical and asymptotic results. Finally, we demonstrated the flexibility of curvilinear shell elements on a journal bearing, calculating the pressure distribution in the lubricating film.

3.2.3 Methods development – coarse grained closed and open-pore shell models.

Model development

In this section, we derive the governing equations for a thin porous medium and also present the associated equations for multiphase lubrication flows. The geometry used in the development of this model is shown in Fig. 59. The system is bounded at the bottom by a rigid, impermeable substrate, shown in dark gray. Atop this substrate is a multiphase lubrication layer of thickness h_{lub}, where the light gray region represents a liquid and the white region is a gas. The liquid-air interface is shown with the dashed curve. This lubrication layer is bounded above by a porous medium of thickness h_{por}. The location of these material boundaries are denoted by h_i, such that $h_{\text{lub}} = h_1 - h_2$ and $h_{\text{por}} = h_3 - h_1$. This system is characterized by physical properties and parameters which will be further discussed in the following sub-sections. All of these quantities, including thickness of the layers, may vary spatially and temporally, as $\beta = \beta(x, y, t)$, to obtain complicated topology and spatially inhomogeneous materials.

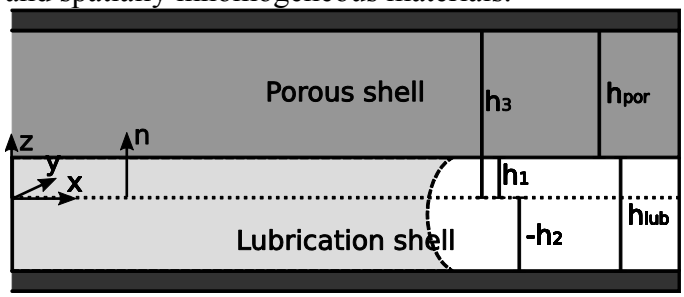

Figure 59 Illustration of the geometry used in this model.

In Fig. 59, the substrate is shown aligned in the $x-y$ plane. This is done for ease of the presentation of equations in this section. However, this assumption can be generalized to accommodate arbitrary orientation, including curved surfaces, consistent with Roberts et al. (2012). This is accomplished through the use of the shell gradient operator, $\nabla_{\text{II}} = \text{I} - \mathbf{nn}\cdot\nabla$, where I is the identity tensor, $\mathbf{n}$ is the normal vector to the shell/substrate, illustrated in Fig. 59,

and ∇ is the traditional three-dimensional gradient operator. More details on the implementation of this in a finite-element framework can be found in Roberts et al. (2012).

Multiphase lubrication flow

In order to understand porous flow in thin geometries, such as shown in Fig. 59, we must first be able to model the flow in the adjoining fluid region. This multiphase lubrication model was presented thoroughly by Roberts et al. (2012), but will be shown here for completeness. Flow in a thin region is governed by the lubrication theory of Reynolds (1886), which is stated by the governing equation

$$-\nabla_{\text{II}}\cdot\mathbf{q}_{\text{lub}} + \mathbf{B}_{1,\text{II}}\cdot\nabla_{\text{II}}h_{\text{lub},1} - \mathbf{B}_{2,\text{II}}\cdot\nabla_{\text{II}}h_{\text{lub},2} = \mathbf{n}\cdot(\mathbf{B}_{1,\text{n}} - \mathbf{B}_{2,\text{n}}). \tag{1}$$

In this equation, $\mathbf{B}_i$ is the translation of boundary i, where $i = 2$ is the bottom, rigid substrate and $i = 1$ is the top, porous medium. Tangential movement of the boundary is given by $\mathbf{B}_{i,\text{II}} = \text{I} - \mathbf{nn}\cdot\mathbf{B}_i$ and movement or flow normal to the boundary is $\mathbf{B}_{i,\text{n}} = \mathbf{nn}\cdot\mathbf{B}_i$. It is important to note that flow through the upper, porous boundary is included in the $\mathbf{B}_{1,\text{n}}$ term. Slopes in the upper or lower boundaries are expressed by $\nabla_{\text{II}}h_{\text{lub},i}$. The primary physics of this equation are contained in the flow rate term, $\mathbf{q}_{\text{lub}}$, which is given by

$$\mathbf{q}_{\text{lub}} = -\frac{h_{\text{lub}}^3}{12\mu}\left(\nabla_{\text{II}}p_{\text{lub}} - \rho\mathbf{g}_{\text{II}} + \mathbf{F}_{\text{CSF}}\right) + \frac{h_{\text{lub}}}{2}(\mathbf{B}_{1,\text{II}} + \mathbf{B}_{2,\text{II}}). \tag{2}$$

The independent variable in this system is the lubrication pressure, p_{lub}. Additionally, μ is the fluid viscosity, $\mathbf{g}_{\text{II}} = \text{I} - \mathbf{nn}\mathbf{g}$ is the gravity vector, and $\mathbf{F}_{\text{CSF}}$ is the surface tension body force. From this flow rate, a mean velocity field can be calculated by $\bar{\mathbf{u}} = \mathbf{q}_{\text{lub}} / h_{\text{lub}}$.

Interfaces between two fluids (in this case, a liquid and air, as shown in Fig. 59) are captured by a level-set field. The level-set distance function, f, is governed by

$$\frac{\partial f}{\partial t} = -\bar{\mathbf{u}}\cdot|\nabla_{\text{II}}f|. \tag{3}$$

Surface tension forces are calculated from this level-set field using the balanced-force formulation [Francois et al. (2006), Herrmann (2008), Roberts et al. (2012)], where the force is given by

$$\mathbf{F}_{\text{CSF}} = \sigma\kappa\nabla_{\text{II}}H. \tag{4}$$

Here, σ is the surface tension, κ is the total curvature of the interface, and H is the Heaviside function describing the smoothed location of the interface. Specifics of this implementation can be found in Roberts et al. (2012). All material properties are also weighted by the Heaviside function, following

$$\beta = \beta_{\text{a}} + (\beta_{\text{b}} - \beta_{\text{a}})H. \tag{5}$$

The total curvature κ is broken down into two components, $\kappa = \kappa_{\text{n}} + \kappa_{\text{II}}$. The curvature in the shell direction is calculated from the level-set field,

$$\kappa_{\text{II}} = \nabla_{\text{II}}\cdot\mathbf{n}_{ab}, \tag{6}$$

while the curvature through the lubrication thickness is given by the model

$$\kappa_z = \frac{1}{h_{\text{lub}}}\left[\cos(\pi - \theta_1 - \tan^{-1}(\mathbf{n}_{ab}\cdot\nabla_{\text{II}} h_{\text{lub},1})) + \cos(\pi - \theta_2 - \tan^{-1}(\mathbf{n}_{ab}\cdot\nabla_{\text{II}} h_{\text{lub},2}))\right], \tag{7}$$

which assumes a circular arc for the interface. In these equations, $\mathbf{n}_{ab} = \nabla_{\text{II}} f$ is the normal vector to the interface and θ_i is the liquid contact angle at boundary i.

Thin-region porous flow

Flow through porous media has been modeled for over a century with Darcy's law [Darcy (1856)], which relates the liquid pressure in the pores, p_{por}, to the liquid flux, or superficial velocity, $\mathbf{v}$,

$$\mathbf{v} = -\frac{1}{\mu}\mathrm{K}\cdot\nabla p_{\text{por}}. \tag{8}$$

Here, μ is again the liquid viscosity and K is a tensor permeability. Commonly, for isotropic materials, the permeability can be characterized by a scalar k, $\mathrm{K} = k\mathrm{I}$. An unsteady-state mass conservation equation completes the description of this flow,

$$-\frac{\partial C}{\partial t} = \rho\nabla\cdot\mathbf{v}, \tag{9}$$

where C is the liquid mass concentration in the medium and ρ is the liquid density. Instead of using the concentration, it is more common to recast (9) in terms of more physically-intuitive variables

$$-\phi\frac{\partial S}{\partial t} = \nabla\cdot\mathbf{v}. \tag{10}$$

Here, ϕ is the porosity of the material, which is the ratio of the volume of pore space to the total volume, and S is the saturation of the material, defined as the ratio of the volume of pore space filled with liquid to the total pore space. Therefore, (9) and (10) are related by $C = \rho\phi S$.

The purpose of this model, however, is to obtain a reduced-order model that takes advantage of the thin nature of the flow. To obtain this thin-porous-flow model, the velocity can be separated into components normal ($\mathbf{v}_{\text{n}}$) and tangential ($\mathbf{v}_{\text{II}}$) to the thin direction,

$$\mathbf{v} = \mathrm{I} - \mathbf{nn}\cdot\mathbf{v} + \mathbf{nn}\cdot\mathbf{v} = \mathbf{v}_{\text{II}} + \mathbf{v}_{\text{n}}. \tag{11}$$

This split velocity expression is then inserted into (10), transforming it to

$$-\phi\frac{\partial S}{\partial t} = \nabla_{\text{II}}\cdot\mathbf{v}_{\text{II}} + \nabla_{\text{n}}\cdot\mathbf{v}_{\text{n}}. \tag{12}$$

If we make the assumption, typical of a lubrication-type model, that gradients of velocity do not change through the thickness of the material, then (12) can be integrated through the thickness of the film to obtain

$$-h_{\text{por}}\phi\frac{\partial S}{\partial t} = h_{\text{por}}\nabla_{\text{II}}\cdot\mathbf{v}_{\text{II}} + \mathbf{n}\cdot\mathbf{v}_{\text{n}}\,|_{z=h_3} - \mathbf{n}\cdot\mathbf{v}_{\text{n}}\,|_{z=h_1}. \tag{13}$$

At the top of the porous layer, we assume no liquid flux, which sets the third term in (13) to zero, leaving

$$-h_{\text{por}}\phi\frac{\partial S}{\partial t} = h_{\text{por}}\nabla_{\text{II}}\cdot\mathbf{v}_{\text{II}} - \mathbf{n}\cdot\mathbf{v}_{\text{n}}\,|_{z=h_{\text{l}}} \,. \tag{14}$$

Finally, the Darcy relation for the liquid velocity (8) can be split according to (11) and inserted into (14), yielding

$$-h_{\text{por}}\phi\frac{\partial S}{\partial t} = -\frac{h_{\text{por}}}{\mu}\nabla_{\text{II}}\cdot\left(\mathrm{K}_{\text{II}}\cdot\nabla_{\text{II}}p_{\text{por}}\right) + \frac{1}{\mu}\mathrm{K}_{\text{n}}\nabla_{\text{n}}p_{\text{por}}\Big|_{z=h_{\text{l}}}, \tag{15}$$

where $\mathrm{K}_{\text{II}} = \mathrm{I} - \mathbf{nn}\cdot\mathrm{K}$ and $\mathrm{K}_{\text{n}} = \mathbf{nn}\cdot\mathrm{K}$. In (15) the first term represents accumulation of liquid in the pore space (or saturation of the pores), the second term represents diffusion of liquid through the porous medium, but only in the planar direction, and the third term is effectively a source term for liquid flux into the porous layer from the lubrication layer. As was necessary for the curvature in the z-direction, a model is required for this final source terms. Options for this model, along with additional modifications to (15), for specific porous media types are discussed in the following two sections.

Closed-feature flow

One interest for this model development is for manufacturing applications where the porous material may be highly structured. An example of this type of geometry is shown on the feature scale in Fig. 60, where the porous medium is made up for a solid material with a regular array of holes (pores) arranged in it. Each of these pores is cylindrical having radius r and height h_{por}. They are open to the lubrication layer at $z = h_{\text{l}}$ but are not open at the top, $z = h_3$. These pores are isolated and liquid cannot flow between them, except by flowing through the lubrication layer. Therefore, each of these pores, or features, are "closed."

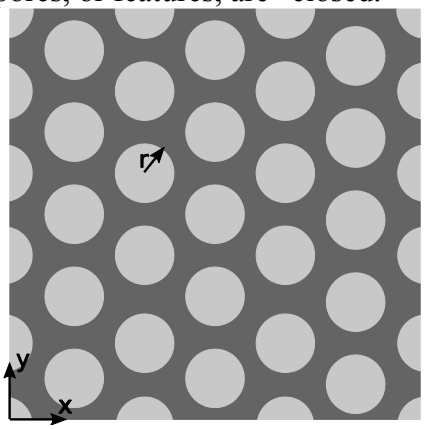

Figure 60 Sample illustration of a closed-feature porous material, shown in the x-y plane, featuring an array of hexagonal-packed holes in an otherwise impermeable solid. Light gray regions are pores while the dark gray is impermeable material.

Because the features are closed, there can be no transport along the plane of the material. This leads to a significant simplification of (15), removing the need for the second term, leaving

$$-h_{\text{por}}\phi\frac{\partial S}{\partial t}=\frac{1}{\mu}K_{zz}\left.\frac{dp_{\text{por}}}{dz}\right|_{z=h_{\text{l}}}. \tag{16}$$

Here, the last term was simplified by recognizing that there is only one remaining component to the permeability tensor, K_{zz}, and that the normal component of the pressure gradient is in the z direction. This leads to a simple expression for the velocity in the z direction,

$$v_z=-\frac{1}{\mu}K_{zz}\frac{dp_{\text{por}}}{dz}. \tag{17}$$

To model this geometry using a continuum model such as (16), we must upscale our microscopic view of the geometry shown in Fig. 60 and create continuum properties from it. In this case, an expression for the permeability and pressure gradient must be determined.
From the Hagen-Poiseuille law for flow through a cylindrical pipe [de Nevers (1991)], we obtain an expression for the mean velocity as a function of the pressure gradient.

$$v_{\text{pipe}}=-\frac{r^2}{8\mu}\frac{dp}{dz}. \tag{18}$$

To account for an array of holes with porosity ϕ, we simply multiply (18) by ϕ to obtain the upscaled mean velocity through an array of cylindrical holes, $v_z=\phi v_{\text{pipe}}$. Comparing (17) and (18) leads to a simple form for the cross-shell permeability, $K_{zz}=\phi r^2/8$.

This procedure for determining the permeability is easily generalizable to other closed pore configurations oriented in the z direction. For example, following the solution for laminar flow in a square duct presented by Panton (2005), one can integrate the velocity profile to determine the mean velocity and solve for the effective permeability, $K_{zz}^{\text{square}}=0.0351449L^2\phi$, where \$2L\$ is the width of the square channel.
In this reduced-order model, pressure gradients in the thin direction are not resolved numerically. Therefore, a model is necessary for $\frac{dp_{\text{por}}}{dz}$ in (16). We assume that the pressure gradient can be approximated by a finite difference, where the distance, Δz, is the amount of the pore filled with liquid (Sh_{por}). The pressure difference over this distance can be calculated by knowing the pressure in the lubrication layer (which is the same as the pressure at the bottom or the pore) and the pressure below the interface ($z=h_{\text{l}}+Sh_{\text{por}}$),

$$\begin{aligned}\frac{dp_{\text{por}}}{dz}&=\frac{\Delta p_{\text{por}}}{\Delta z}\\&=\frac{p\,|_{z=h_{\text{l}}+Sh_{\text{por}}}-p\,|_{z=h_{\text{l}}}}{Sh_{\text{por}}}\\&=\frac{(p_{\text{gas}}-p_{\text{cap}})-p_{\text{lub}}}{Sh_{\text{por}}}\end{aligned} \tag{19}$$

In the last line of (19), we recognize that the pore is initially full of gas at atmospheric pressure. When liquid begins invading the pores, the gas is compressed and its pressure increases following the ideal gas law, which sets the pressure at the top of the pore. The pressure below the liquid interface is simply adjusted by the capillary pressure jump across the interface, the sign of which depends on whether the medium is hydrophillic or hydrophobic.
We determine the pressure in the gas trapped in the pore using the ideal gas law. Assuming that the system is isothermal, this yields the expression $p_{\text{por}}V_{\text{por}} / n = p^0_{\text{por}}V^0_{\text{por}} / n^0$, where n is the moles of gas in the pore, V_{por} is the volume of the pore occupied by gas, and a superscript 0 denotes the initial condition. Knowing that the saturation is inversely related to the gas volume, we relate the current and initial volume, $V_{\text{por}} / V^0_{\text{por}} = 1 - S$. Defining a molar change ratio as $\bar{n} = n / n^0$, we can finally express the gas pressure as

$$p_{\text{gas}} = \frac{p^0_{\text{gas}}\bar{n}}{1-S}. \tag{20}$$

In the simplest case, all of the gas is trapped in the pore, so $\bar{n} = 1$. Later we relax this assumption and allow gas to diffuse out of the pores and into the liquid, leading to $\bar{n} < 1$.

The jump in pressure across the liquid-gas interface, or capillary pressure p_{cap}, is calculated from the Young-Laplace equation,

$$p_{\text{cap}} = \frac{2\sigma\cos(\theta_1)}{r}. \tag{21}$$

Traditionally, as in (7), the contact angle θ_1 is the equilibrium, or static, value. However, when the interface velocity is very fast, and a dynamic contact angle results. To capture this effect, we use a molecular-kinetics-based wetting model [Martic et al. (2002), Blake et al. (2002), Blake et al. (2004)] to calculate the effective dynamic contact angle

$$h_{\text{por}}\frac{\partial S}{\partial t} = C_1 \sinh\left(\sigma C_2\left[\cos(\theta_1^0) - \cos(\theta_1)\right]\right), \tag{22}$$

where C_1 and C_2 are parameters based on the molecular-kinetic theory [Martic et al. (2002), Blake et al. (2002), Blake et al. (2004)], θ_1^0 is the equilibrium contact angle, and θ_1 is the dynamic contact angle. We follow Reddy et al. (2005) for calculation of the C_i parameters. This equation is solved for $\cos(\theta_1)$ and used in (21) to calculate the capillary pressure.
Combining the governing equation (16) with the model for pressure gradient (19), along with the calculated values for the permeability, gas pressure (20), and capillary pressure (21) yields the complete model for closed, cylindrical features,

$$-h_{\text{por}}\phi\frac{\partial S}{\partial t} = \frac{1}{\mu}\frac{\phi r^2}{8}\left(\frac{\frac{p^0_{\text{gas}}\bar{n}}{1-S} - \frac{2\sigma\cos(\theta_1)}{r} - p_{\text{lub}}}{Sh_{\text{por}}}\right). \tag{23}$$

This model for the pore saturation is coupled to the lubrication flow in two ways. First, the lubrication pressure directly appears in (23), influencing the saturation rate. Secondly, the velocity of liquid flowing into the porous medium (17) is included as the upper-wall velocity, $\mathbf{B}_{l,n}$ in (1), ensuring that conservation of mass is enforced. Of course, if this expression is being evaluated in a multiphase flow simulation, where there are liquid and gas phases in the lubrication layer, we can simply set $\partial S / \partial t = 0$ in gas regions, as liquid can flow neither into or out of the pores when there is not liquid in the neighboring lubrication region. Similarly, if S approaches 1, which would happen as all gas leaves the pores ($\bar{n} \to 0$), the capillary interface would disappear, and the entire pressure gradient would disappear, $dp_{\text{por}} / dz = 0$.

Closed-feature gas diffusion

As mentioned earlier, gas is trapped when liquid fills closed pores. Gas pressures may get quite high, however, allowing the gas to diffuse into the liquid. While a rigorous understanding of this behavior would require a full accounting of gas inventory in the pores and the lubrication layer, we choose to take a simpler approach. If we assume that there is much more liquid in the lubrication layer then there is in the pores, we can effectively treat the lubrication layer as an infinite sink of dissolved gas. This leaves only the liquid in the pore to model.

The gas flux in the pore can be written $J = -D\partial C / \partial z$, where J is the flux, D is the coefficient of diffusion for gas in liquid, and C is the concentration. Assuming a linear concentration profile through the pore, the flux can be re-written

$$J = -D\frac{\partial C}{\partial z} = -D\frac{C|_{z=h_l+Sh_{\text{por}}} - C|_{z=h_l}}{Sh_{\text{por}}}. \tag{24}$$

The concentrations at the interface can be estimated using Henry's law, which relates the concentration to the gas pressure, $p_{\text{gas}} = k_H C|_{z=h_l+Sh_{\text{por}}}$. If the liquid was exposed to air prior to the processing, equilibrium of the gas to atmospheric pressure can also be assumed as the condition at the open end of the pore, $p_{\text{atm}} = k_H C|_{z=h_l}$. This allows (24) to be written as

$$J = -\frac{D}{Sh_{\text{por}}k_H}(p_{\text{gas}} - p_{\text{atm}}) = -\frac{DP^0_{\text{gas}}}{Sh_{\text{por}}k_H}\left(\frac{\bar{n}}{1-S} - 1\right) \tag{25}$$

after substituting (20) for p_{gas} and assuming that $P^0_{\text{gas}} = p_{\text{atm}}$.

In order to determine the amount of gas remaining in a pore, a mass conservation equation is needed. Equating the rate of mass loss with the flux in a single pore yields

$$\frac{\partial n}{\partial t} = \pi r^2 J. \tag{26}$$

If we scale this equation to the continuum level using the porosity, (26) can be rewritten

$$\frac{\partial \bar{n}}{\partial t} = -\left(\frac{RTD}{h^2_{\text{por}}k_H}\right)\frac{1}{S}\left(\frac{\bar{n}}{1-S} - 1\right), \tag{27}$$

after some algebraic manipulation and simplification. Here, R is the universal gas constant and T is the temperature, which arise from the ideal gas law. Equation (27) can be solved simultaneously with (23) to study the diffusion of gas out of the pores as they fill.

Open-feature flow

In contrast to the closed-feature flow discussed earlier, a fully-porous medium allows flow in the in-plane direction, in addition to the thin direction. This material may still be structured, as illustrated in Fig. 61. Conversely from Fig. 60, Fig. 61 consists of solid pillars surrounded by open regions that allow fluid flow. As before, the cylinders have a radius r and thickness h_{por}. The open regions are open to the lubrication layer at $z = h_1$ but are not open at the top, $z = h_3$.

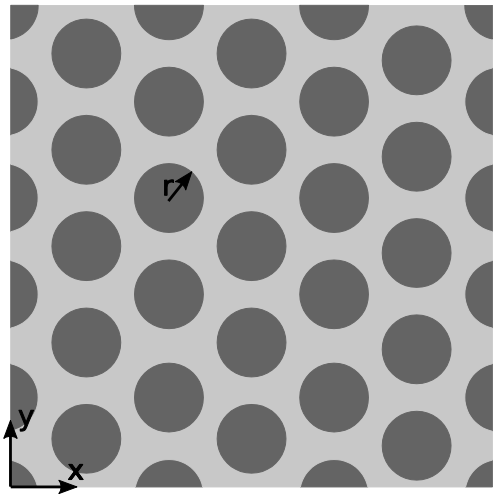

Figure 61 Sample illustration of an open-feature porous material, shown in the x-y plane, featuring an array of hexagonal-packed solid pillars in an otherwise open material. Light gray regions are pores while the dark gray is impermeable material.

For open features, all terms in (15) are necessary. However, we still need a model for the last term in (15), which represents flow through the neighboring lubrication region. Derivation of the pressure gradient in this term is not as straight-forward as it is for cylindrical, closed features, as the geometry is more complex and the physics less clear. However, one can imagine a form similar to (19). For open features, we assume that the gas can move throughout the template freely and does not pressurize as it does in the closed feature case; this leads to $p_{\text{gas}} = p_{\text{atm}}$. This holds for the case when the features are not fully saturated, $S < 1$. If the features are saturated, $S = 1$, unlike the closed-feature case, liquid can still flow in or out of the features, depending on the pore pressure, p_{por}. Therefore, the pressure gradient has a different form when the features are fully saturated,

$$\nabla_{\text{n}} p_{\text{por}}\Big|_{z=h_1} = \begin{cases} \dfrac{p_{\text{atm}} - \dfrac{2\sigma\cos(\theta_1)}{r_{\text{por}}} - p_{\text{lub}}}{S h_{\text{por}}} & S < 1 \\ \dfrac{p_{\text{por}} - p_{\text{lub}}}{2h_{\text{por}}} & S = 1 \end{cases}. \tag{28}$$

Here, r_{por} is the average pore radius.

Values for the permeability can be calculated using a series solution to the flow past an array of cylinders, originally derived by Drummond and Tahir (1984). The geometry described in Fig. 61 is orthotropic, with a different value for the permeability in the thin direction as compared to the in-plane direction. Following a similar methodology to that presented earlier, but using the drag force solution of Drummond and Tahir (1984), we arrive with the permeability tensor

$$\mathrm{K} = \begin{bmatrix} K_{xx} & 0 & 0 \\ 0 & K_{xx} & 0 \\ 0 & 0 & 2K_{xx} \end{bmatrix}. \tag{29}$$

Here, the permeability expression K_{xx} is the series solution [Drummond and Tahir (1984)]

$$K_{xx} = \frac{\pi r^2}{8\acute{U}}\left[\ln\left(\frac{1}{\acute{U}}\right) - 1.353663936 + 2\acute{U} - \frac{\acute{U}^2}{2} - \frac{0.358221\acute{U}^3}{1+2.26579\acute{U}^2} \right], \tag{30}$$

where $\acute{U} = 1-\phi$ is the feature density. This form assumes that z is the thin direction, although this tensor could easily be rotated for different orientations.

Earlier, the saturation S was treated as the independent variable, as the pore pressure p_{por} did not appear in the final expression (23). In (15), however, both S and p_{por} appear as unknowns. To address this, we recognize that S is a function of p_{por} and use the chain rule to rewrite the time derivative in the first term of (15) as $\partial S/\partial t = (\partial S/\partial p_{\mathrm{por}})(\partial p_{\mathrm{por}}/\partial t)$. This reorganization leaves p_{por} as the independent variable, assuming a relationship between S and p_{por}, known as a capillary pressure-saturation relationship [Cairncross et al. (1996)]. These relationships can be analytically or experimentally obtained, and often exhibit hysteresis. However, here we derive a simple analytical form following the method presented by Cairncross et al. (1996).

In a hexagonal-packed cylinder configuration, the cylinder radius r and porosity ϕ fully specify the arrangement. For a given arrangement the minimum pore distance, $r_{\mathrm{por}}^{\mathrm{min}}$, is given by

$$r_{\mathrm{por}}^{\mathrm{min}} = -2r + \frac{\sqrt{2\pi}r^2}{3^{1/4}\sqrt{r^2(1-\phi)}}, \tag{31}$$

while the maximum pore spacing, $r_{\mathrm{por}}^{\mathrm{max}}$, is

$$r_{\mathrm{por}}^{\mathrm{max}} = 2r(\sqrt{3}-1) + \sqrt{3}r_{\mathrm{por}}^{\mathrm{min}}. \tag{32}$$

If we assume that the pore distribution is a Gaussian, with a mean value of $r_{\mathrm{por}}^{\mathrm{mean}} = (r_{\mathrm{por}}^{\mathrm{max}} + r_{\mathrm{por}}^{\mathrm{min}})/2$ and a standard deviation of $r_{\mathrm{por}}^{\mathrm{stdv}} = (r_{\mathrm{por}}^{\mathrm{mean}} - r_{\mathrm{por}}^{\mathrm{min}})/2$, the probability distribution function of the pore size distribution is

$$F(r_{\mathrm{por}}) = \frac{1}{\sqrt{2\pi}r_{\mathrm{por}}^{\mathrm{stdv}}} \exp\left[\frac{-(r_{\mathrm{por}} - r_{\mathrm{por}}^{\mathrm{mean}})^2}{2r_{\mathrm{por}}^{\mathrm{stdv}} r_{\mathrm{por}}^{\mathrm{stdv}}} \right]. \tag{33}$$

Further following Cairncross et al. (1996), the saturation as a function of pore size is

$$S(r_{\text{por}}) = \frac{\int_0^{r_{\text{por}}} r^2 F(r_{\text{por}})dr}{\int_0^{\infty} r^2 F(r_{\text{por}})dr}. \tag{34}$$

Assuming the Young-Laplace form of the capillary radius, $r_{\text{por}} = 2\sigma\cos(\theta_1)/p_{\text{por}}$, along with (34) yields a functional form for the capillary pressure-saturation relationship, $S(p_{\text{por}})$. This expression allows calculation of $\partial S/\partial p_{\text{por}}$, completing the description of the governing equation for open-feature flow,

$$-h_{\text{por}}\phi\frac{\partial S}{\partial p_{\text{por}}}\frac{\partial p_{\text{por}}}{\partial t} = -\frac{h_{\text{por}}K_{xx}}{\mu}\nabla_{\text{II}}^2 p_{\text{por}} + \frac{2K_{xx}}{\mu}\nabla_{\text{n}} p_{\text{por}}\Big|_{z=h_1}. \tag{35}$$

Numerical method

The multiphase lubrication and porous flow equations are implemented into the Galerkin finite element method code GOMA [Schunk et al. (2006)]. This method uses isoparametric quadrilateral shell elements with bi-linear (Q1) Lagrange interpolation functions, the implementation of which was discussed in a previous work [Roberts et al. (2012)]. The nonlinear residual equations were solved using fully-coupled Newton iterations, and the resulting linear equations were solved with direct (LU) and iterative (GMRES) algorithms deployed from a third party library Trilinos. Transient problems are advanced in time with the backward Euler method.

Physical properties and system characteristics, such as material thicknesses or pore properties, may vary spatially. In order to handle complex shapes and distributions, such as those that may arise in nano-fabrication, a pattern-to-mesh algorithm was developed and implemented into the code. This tool enables a gray-scale raster image, representing spatial variations in a given property, to be mapped onto the computational mesh and used for simulations.

3.3 Jet-and-Flash Imprint Lithography Application

A number of demonstration problems for the porous shell model with closed features are presented in this section, including one for our ultimate, intended application. First, we investigate the time scales for the filling of closed-pores. Then we examine filling of closed pores with spatially varying properties under multiple squeezing drops.

Flooded closed-feature filling

In this example, we consider a closed feature porous region with a lubrication region flooded with liquid (does not include a free interface). The porous media has a uniform, constant porosity of $\phi = 0.1$ of cylindrical pores with $h_{\text{por}} = 1\mu\text{m}$ and $r_{\text{por}} = 100\text{nm}$. The liquid is water and the gas air, both initially at atmospheric pressure, and the lubrication layer is held at a constant thickness of $h_{\text{lub}} = 15\mu\text{m}$. The liquid has a static contact angle of $\theta_1 = \theta_2 = 30^\circ$ with the substrate and the liquid-air surface tension is $\sigma = 25\text{dyne/cm}$. The simulation domain is $50\mu\text{m}$ square. Simulations are performed using both static and dynamic contact angles (22) and with

and without gas diffusion through the pores. When gas diffusion is included, the diffusivity of air in water was $D = 10^6 \text{cm}^2/\text{s}$, the temperature was $T = 25°C$, and the Henry's law constant was $k_H = 10^{12} \text{cm}^3\text{Ba/mol}$. Results of simulations comparing the effect of the physics of contact angle and gas diffusion are shown in Fig. 62.

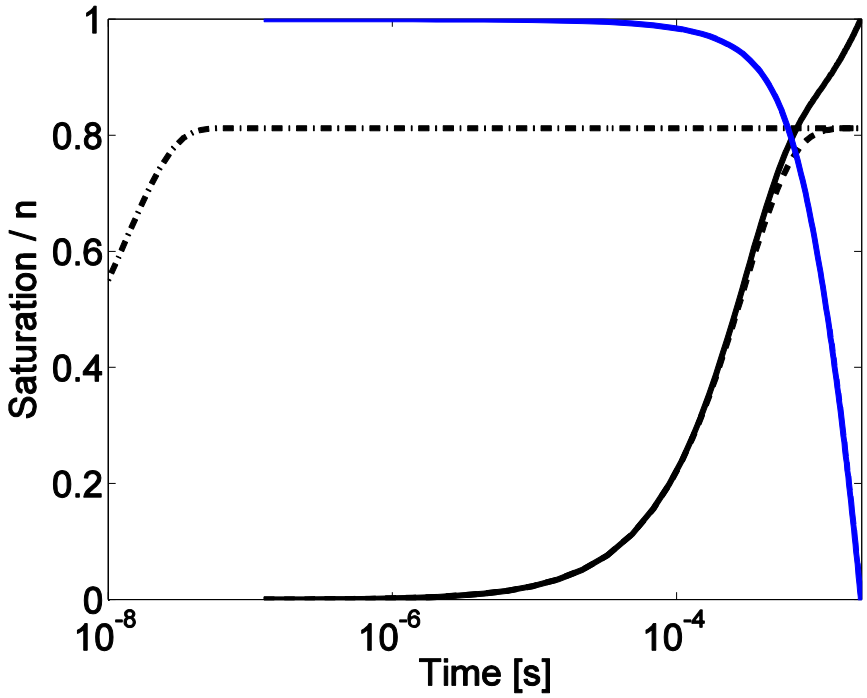

Figure 62 Results from filling of closed features with a flooded lubrication region. The dash-dot curve (- . -) is the saturation when then static contact angle is used and no gas transport is allowed, the dashed curve (- -) uses a dynamic contact angle, but still no gas transport, and the solid curves us a dynamic contact angle and allow gas diffusion. Black curves are saturation and the blue curve is the molar gas ratio, nbar.

The first comparison is the effect of using a dynamic contact angle, shown in the dash-dot and dashed curves in Fig. 62. Using only a static contact angle, the features fill to their equilibrium value of 0.81 in less than $0.1\mu\text{s}$. However, in order for that to happen, an average interfacial velocity of 10m/s would be required, a significantly higher velocity than is capable of maintaining a static contact angle. More physically, the filling curve for using a dynamic contact angle is shown by the dashed line in Fig. 62. In this case, the filling happens over $\sim 1\text{ms}$, still reaching the same equilibrium saturation value.

In these first two simulations, the saturation reached an equilibrium value due to the trapping of gas in the pores, not allowing it to diffuse out. The equilibrium value of 0.81 represents a balance between the increased pressure of the gas due to compression (20) and the capillary forces (21). This increased gas pressure, however, increases the equilibrium concentration of gas in the liquid. When (27) is applied, the gas fully diffuses out of the pores, allowing complete saturation, as shown by the solid curves in Fig. 62. The rate of gas diffusion only increases as the pores fill and the pressure increases, leading to gas diffusion on a slower time scale than the initial filling operation, with complete saturation being reached at 2ms. This example problem

shows that both dynamic wetting behavior and gas diffusion are important processes in complete filling of closed features.

Patterned, multiphase closed-feature filling

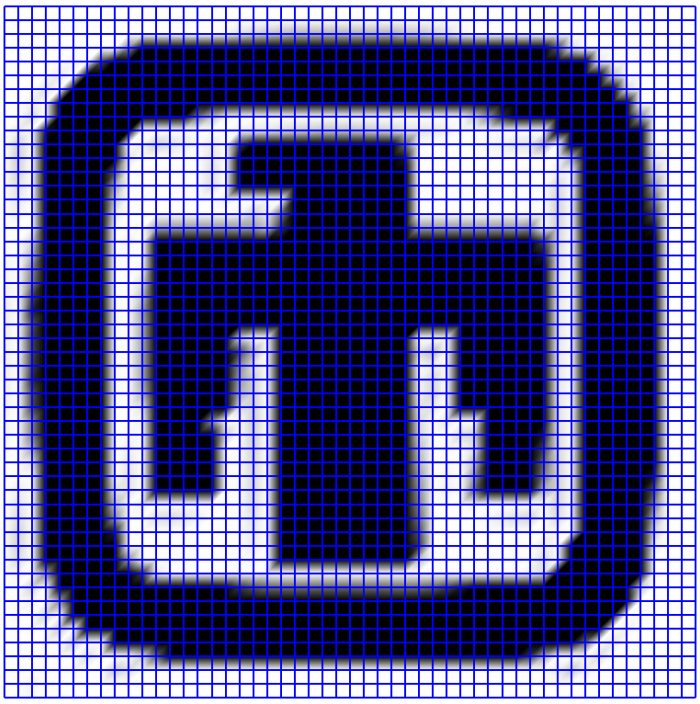

Figure 63: Computational mesh and porosity pattern for simulations. White regions represent unpatterned regions ($\phi = 0$), black is $\phi = 0.2$, and there is a gradient of gray-scale regions between. The computational domain is 90μm wide, and the mesh lines are shown in blue.

Finally, we present an example problem when utilizes the pattern-to-mesh capability presented in section 3.1 to study porous flow with spatially-varying properties in the porous medium. The lubrication layer initially consists of five liquid drops placed in an equally-spaced array. The drops do not initially cover the entire patterned area. The pattern used in this study is shown in Fig. 63, where the porosity varies $\phi = 0 - 0.2$. Fluid and pore properties are the same as the previous example. The initial lubrication height is 5.6μm and the initial drop radius is 15μm.

Figure 64 Results of closed-feature simulations under the patterned template shown in Fig. 5. The dark green curves represent the location of the liquid-air lubrication interface, while the color scheme represents the relative saturation, $S\phi$. In these figure (a) is at t =10^{-6} s, (b) is at t=12 s, and (c) is at t=920 s.

Three time-shots of this simulation are shown in Fig. 64. Figure 64 shows the state shortly after the initial condition. The liquid drops are near their initial configuration, and the patterned, porous region is just beginning to take up liquid. In Fig. 64, the drops have spread to where they are nearly touching in the middle, and some of them have spread outside of the domain at the edges. The patterned regions that are in contact with liquid are fully saturated, while the regions outside the drops remain empty. Finally, in Fig. 64, the drops have fully merged and covered nearly the entire domain. All patterned regions covered with liquid are fully saturated. An interesting thing to note is that through the merging process, a few air bubbles have been trapped in the lubrication region, and the patterned areas covered by these bubbles remain unsaturated. This highlights the need for this type of simulation, to intelligently design imprinting process to minimize air bubble entrapment and eliminate pattern defects.

4. NANOPARTICLE COATINGS AND MICROSTRUCTURES

4.1 Nanoparticles coating on hydrophilic-patterned substrates

Introduction

A key unit operation in most nano-manufacturing processes regards coating or printing the polymer layer to be imprinted or embossed. As discussed in Chapter 1 of this report, this can be achieved a number of ways, depending on the application. In this Chapter we explore two key aspects of such coating processes, together with additional complicating factors. The first is coating and drying on a substrate which has be pre-patterned with regions of hydrophobic and regions of hydrophyllic surface energies. Many have suggested that this is one route to take for hierarchical manufacturing, in which patterned layers at a coarser level can serve as a template for bottom-up manufacturing of smaller microstructural features. We examine this process with the theory of Reynolds film lubrication, overloaded with the effects of nanoparticles, drying, and conjoining/disjoining pressure (Section 4.1).

We also drill down into the nanoparticle-solvent drying processes with direct molecular simulation (Section 4.2). The aim and intent of this work is to study the competition of various physical rate processes on the final microstructure of nanoparticles in a coating. Specifically, the effect of drying rate vs. particle diffusion rate (size, temperature) is examined with LAMMPS models of nanoparticles and explicit solvent. This chapter ends with a summary of an already published study of nanorod-formation under imprint pressure (Section 4.3).

Model development on Continuum Scale

Nanoparticles deposition based on wettability difference has received attention due to their potential applications in microscale devices such as field-effect transistor (Wang et al 2004). Nanoparticles laden liquid is deposited onto a substrate with patterned wettability and after the subsequent drying process, leaving behind layers of nanoparticles at the area where the liquid preferentially wetted. This method employs both lithographic techniques, in order to chemically pattern the substrate with different wettability, and conventional liquid coating process, in order to deposit the liquid onto it. The practical issues worth the investigations here are the limits of the process, i.e. the minimum feature size and maximum pattern density, and the interplay between hydrodynamic and drying.

Model development

Following the coarse-grained approach employed in the analysis of imprinting processes, we are employing Reynolds lubrication equation to describe the liquid film flow on a substrate, with capillary and disjoining pressure as the primary driving forces:

$$\frac{\partial h}{\partial t} + \nabla_{II} \cdot \left\{ \frac{h^3}{3\mu} \left(-\nabla_{II} p + \nabla_{II} \Pi \right) + \mathbf{U}_{bot} h \right\} - \dot{E} = 0$$

$$p + \sigma \nabla_{II}^2 h = 0$$

where h is film thickness, p is capillary pressure, Π is disjoining pressure, $\mathbf{U}_{bot}$ is bottom wall velocity, and $\dot{E}$ is liquid evaporation rate. Disjoining pressure Π in general is a function of the separation between liquid-gas and liquid-solid interfaces, i.e. film thickness h. In this study, we were using disjoining pressure functional form reported by Schwartz et al 2001:

$$\Pi = B\left[\left(\frac{h_*}{h}\right)^n - \left(\frac{h_*}{h}\right)^m\right]$$

$$B = \frac{\sigma}{h_*}\frac{(n-1)(m-1)(1-\cos\theta_{eq})}{n-m}$$

$$n > m$$

where m corresponds to the exponent of the van der Waals potential, n is the exponent of the Born repulsion potential, h_* is the thickness of precursor film at the substrate, and θ_{eq} is the equilibrium contact angle. The dependence on θ_{eq} creates driving force for flow from high to low contact angle.

Particles are treated as continuum field and represented as a volume fraction φ where the appropriate governing equation is the thickness-averaged convective diffusion equation:

$$h\frac{\partial \varphi}{\partial t} + \left\{\frac{h^3}{3\mu}\left(-\nabla_{II} p + \nabla_{II}\Pi\right) + \mathbf{U}_{bot} h\right\}\cdot\nabla_{II}\varphi - \nabla_{II}\cdot\left(Dh\nabla_{II}\varphi\right) - \varphi\dot{E} = 0$$

The coupling between the particles transport and the film flow occurs in the convective term – second term of the equation, the evaporation term – the last term of the equation, and viscosity. Evaporation rate is related to the volume fraction following Schwartz et al 2001:

$$\dot{E} = \dot{E}_0\left[1 - \frac{\varphi}{\varphi_{\max}}\right]^{\nu}$$

$$0 < \nu < 1$$

where $\dot{E}_0$ is evaporation rate of the pure liquid. This evaporation model reflects trends observed in the experiments qualitatively, i.e. as the suspension becomes more concentrated, the evaporation rate falls due to increase of flow resistance put up by packing particles. At a maximum packing φ_{max}, the evaporation rate becomes zero. The values of $\dot{E}_0$ and ν can be determined by curve-fitting of an available experimental data.

Another coupling between film flow and particles transport also occurs in the viscosity where it follows Krieger-Dougherty relationship:

$$\mu = \frac{\mu_0}{\left(1 - \frac{\varphi}{\varphi_{\max}}\right)^2}$$

where μ_0 is viscosity of the pure liquid.

Application

We employed this model in order to predict liquid film shape at two patterned substrates: First is a substrate with only one line on it, in order to study the minimum feature size that the method can coat, and the second is a substrate with multiple lines on it, in order to study the maximum feature density. The dimensions of the substrates and the features are shown 65. The black lines are hydrophilic region with contact angle of 10° and the surrounding area is superhydrophobic with contact angle of 160°.

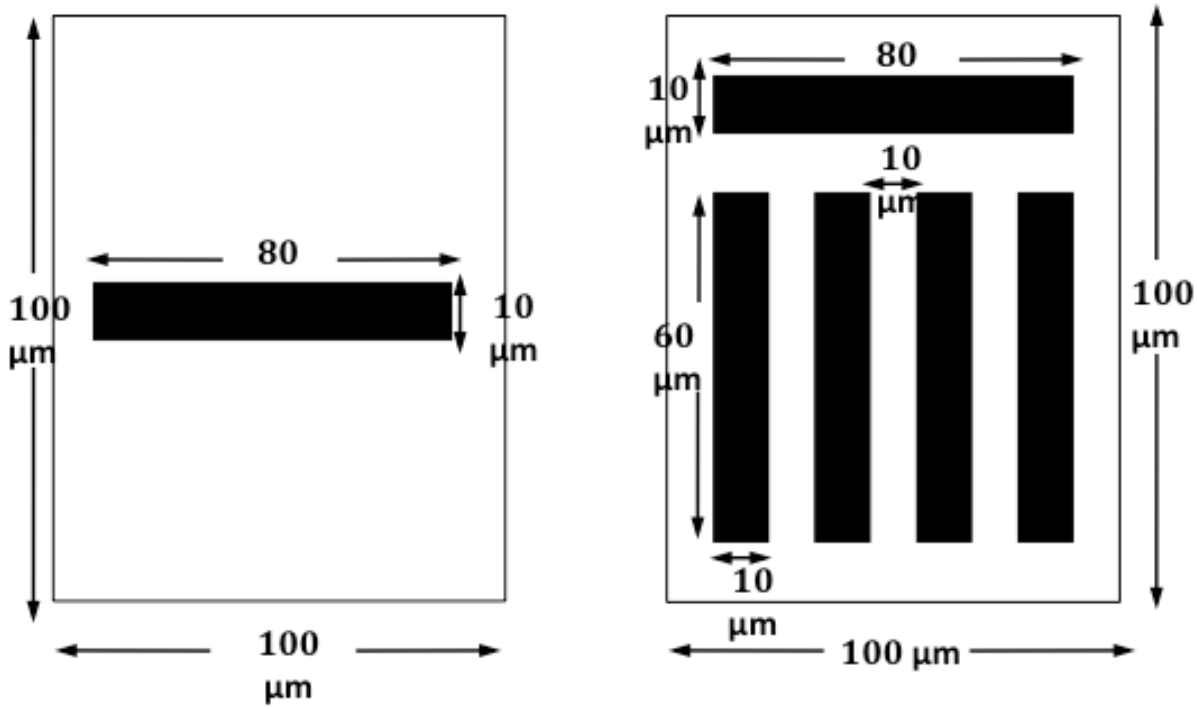

Figure 65: Geometry and dimesions of single-feature and multi-feature substrates.

In our initial analysis, the liquid rearrangement is decoupled from the drying in order to simplify the analysis. The approach is based on assumption that the time scale of rearrangement flow is much faster than that of evaporation. The liquid properties and model parameter values are summarized in the table below.

LIQUID PROPERTIES	Viscosity - μ	1 cP
	Surface tension - σ	70 dyne/cm
DISJOINING PRESSURE MODEL PARAMETERS	Precursor film thickness – h_*	1 μm
	Attractive potential exponent – n	2
	Repulsive potential exponent – m	3

At time t = 0, the liquid layer is uniform at a prescribed thickness with uniform particles concentration. After less than 1 milisecond, the liquid film shape reaches steady state, as shown in Figure 66.

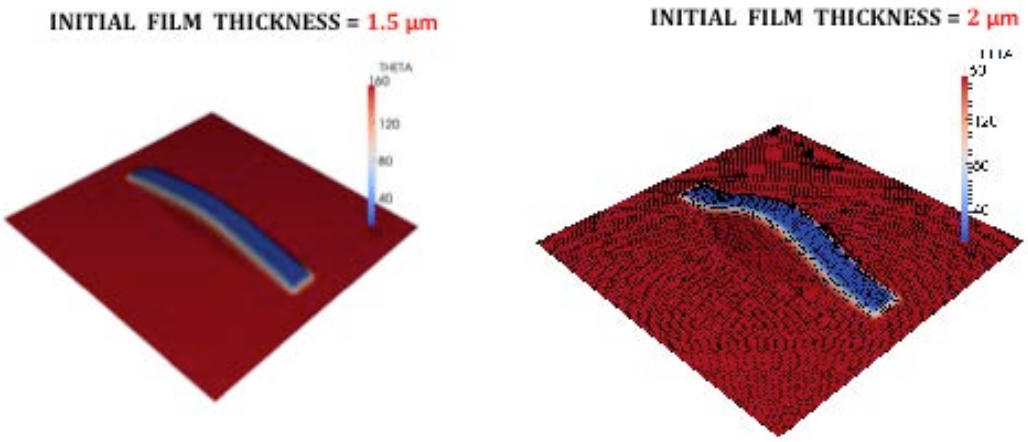

Figure 66: Final film shapes of liquid layer applied onto a substrate with a single feature with different initial film thicknesses.

The final film shape conforms to the pattern at the case where the initial layer thickness is 1.5 microns. It does not, however, at the case of 2 microns, indicating that there is a maximum amount of liquid that a feature can take. We repeated the analysis on a multi-feature substrate and the result is shown in Figure 67.

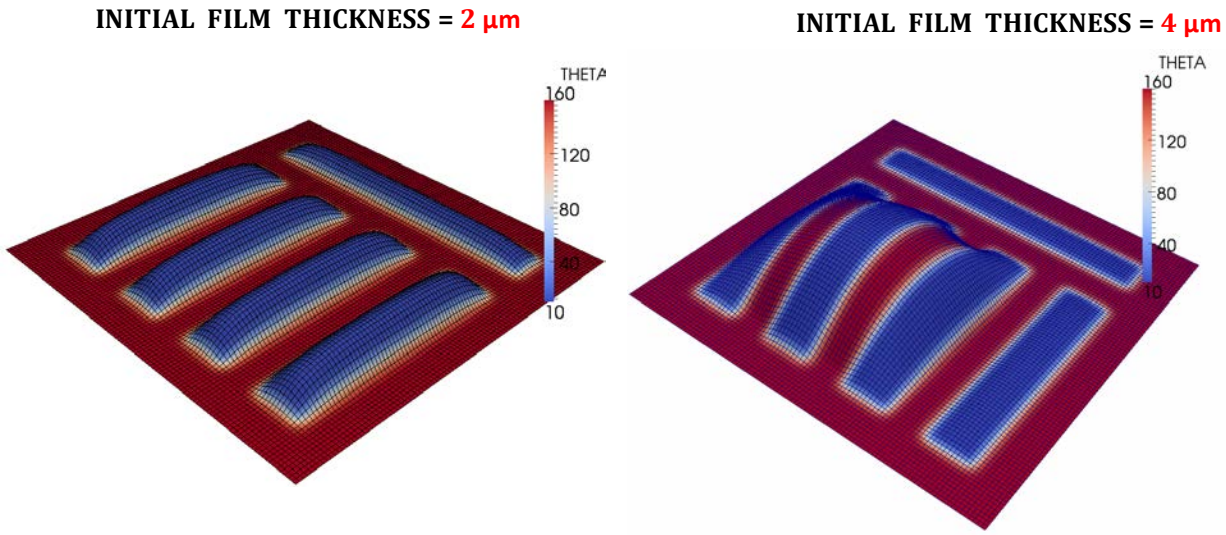

Figure 67: Final film shapes of liquid layer applied onto a substrate with multi feature with different initial film thicknesses.

Here, the film is broken into several droplets conforming to the pattern shapes at the substrate with initial film thickness of 2 microns. However, at the initial film thickness of 4 microns, droplets between the features merged into a bigger droplet that bridged the features. This also indicates the presence of an upper bound of liquid volume that the features can take.

In summary, the limits on the feature size and density are also set by the liquid application step, and not just by the lithography method employed for creating the patterns in the substrate. When the deposited liquid volume exceeded what the features can handle, the resulting droplets no longer conform to the pattern and in the case of multi-feature substrate, merging and bridging droplets will occur.

We have not completed our analysis on the drying process that includes nanoparticles due to difficulties in solving the thickness-averaged convective diffusion equation of nanoparticles. The difficulties arise from very high Peclet number of the transport process (in the order of 500) that the solution from the finite element method that we employed is marred with unphysical concentration fluctuation. We tried to cure some of those numerical instabilities by implementing Taylor Galerkin method and while the method helps alleviating some of the instabilities, it does not completely cure it.

A continuation of this work in the future, if deemed necessary, will include the competition between hydrodynamic force and drying, once the numerical instabilities in solving convective diffusion equation are eliminated. The expectation is that the competition between those two forces will determine the final film shape and nanoparticles deposition pattern.

4.2 Nanoparticle suspension drying at the molecular scale

Simulation Methodology

Solvent evaporation is an important process that can be used to control the assembly of nanoparticles initially dispersed in the solution.[1] We used molecular dynamics (MD) to study this complex phenomenon at the molecular scale. Systems are typically composed of 600-1000 spherical nanoparticles with diameters about 20σ (~6nm) in a solvent consisting of 6-17 million atoms depending on volume fractions. The interactions between solvent atoms are described by a standard Lennard-Jones (LJ) 12-6 potential, and those between nanoparticles and between solvent atoms and nanoparticles are given by integrated LJ potentials.[2] Parameters in potentials are chosen such that nanoparticles are dispersed in the solvent and the equilibrium state is a uniform nanoparticle solution.

Initially the nanoparticle suspension is in thermodynamic equilibrium with its vapor phase and a liquid/vapor interface forms in the xy-plane as illustrated in Figure 1. Periodic boundary conditions are employed in the x and y directions. In the z direction, the suspension is confined by a wall at z=0 while a top wall, far above the liquid/vapor interface, confines the vapor. Evaporation is implemented using LAMMPS fix_evaporate command. A thin deletion zone is introduced near the top wall. To model evaporation into a vacuum all LJ atoms entering this deletion zone are removed from the simulation cell. This gives the maximum evaporation rate. Slower evaporation rates are studied by removing atoms that reach the deletion zone at a controlled rate. A sketch of the evaporating system is shown in Figure 68, where the vapor phase is not included. During evaporation, the evolution of the structure of the nanoparticles as well as the density and temperature profiles of solvent and nanoparticles are monitored. To capture the correct dynamics of evaporation, we used a NVE ensemble, except in a thin layer of thickness about 15σ near the lower wall where the solvent atoms are weakly coupled to a Langevin thermostat. This layer is far enough from the liquid/vapor interface where evaporation occurs that the results are not sensitive to the thermostat.

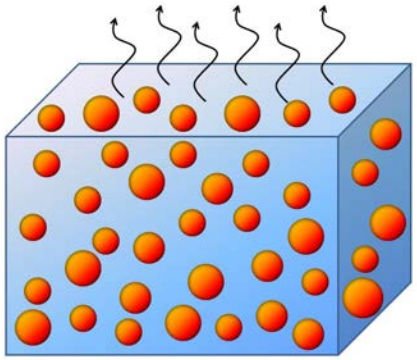

Figure 68: Illustration of the evaporation of solvent from a nanoparticle solution

Nanoparticle Assembly during Evaporation

During the evaporation of the solvent, nanoparticles move towards the liquid/vapor interface but remain in the solution. As the consequence, the density of nanoparticles builds up at the interface. Since the interface has a finite area and can only accommodate a finite number of nanoparticles, a second layer of nanoparticles starts to form after the number of nanoparticles in the top layer near the interface saturates. Therefore, nanoparticles accumulate and layer near the

interface during evaporation. This process is illustrated in Figure 69, where the solvent evaporates quickly into vacuum.

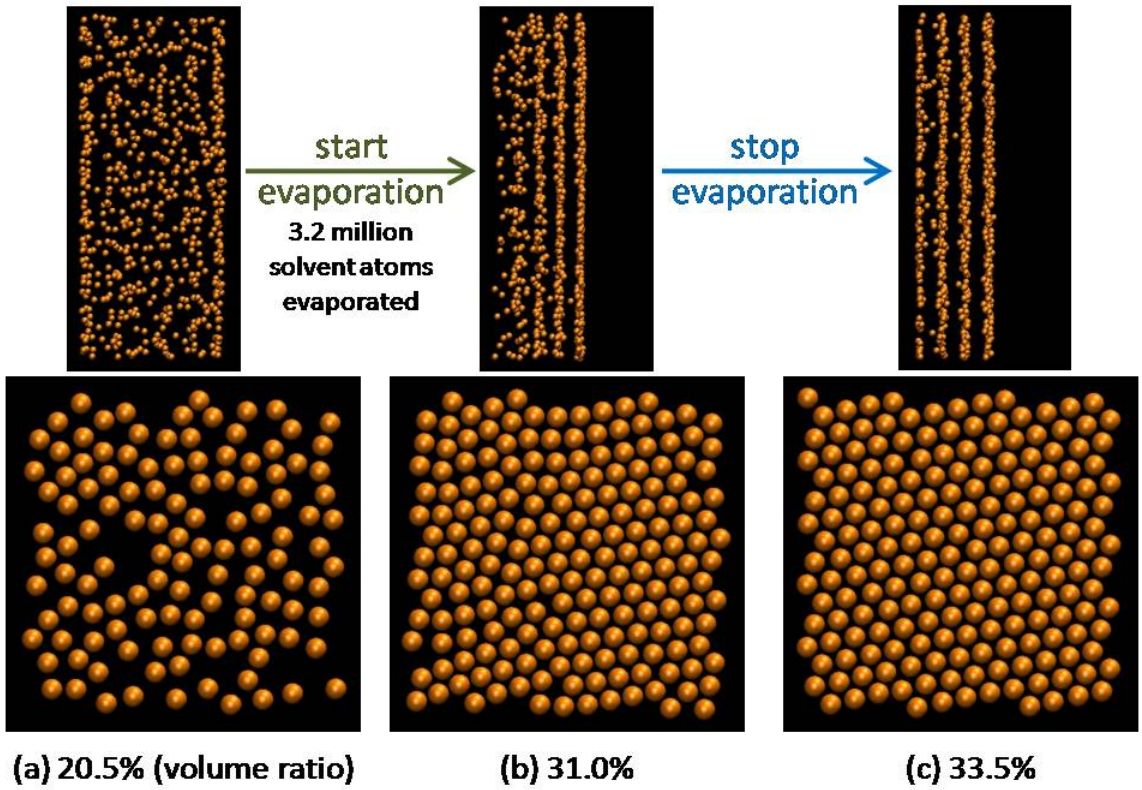

Figure 69: Sample results

Nanoparticles in the top layer essentially form a close packed triangular lattice, as shown in the bottom-middle picture of Figure 69. However, there are several defects and grain boundaries in between. After the evaporation is stopped, the vapor phase re-establishes (which was depleted during the evaporation process), and the packing of nanoparticles in the top layer has time to adjust and relax. The grains coalesce and defects gradually disappear. The final structure is an almost perfect triangular lattice. Note that in the final state, the volume fraction of nanoparticles is about 33.5%, which is still smaller than the critical volume ratio, about 45%, for the crystallization transition. We would expect the layered structure of nanoparticles to collapse and nanoparticles to dissolve and form a uniform solution again. However, this evaporation-induced structure is very stable at our MD time scale (typically 1ns to 10ns). It indicates that the layered structure may be metastable and it requires much longer time to achieve the thermodynamically stable uniform-solution state.

Effect of Evaporation Rate on Assembly Quality

During the solvent evaporation into vacuum, the evaporation rate is not controlled and decreases with time dramatically (see Figure 70), similar to the case of the evaporation of a pure liquid.[3] To study the effect of evaporation rate on nanoparticle assembly, we also simulated the case where the evaporation rate is controlled. The fixed rate we chose is small than the initial

(final) rate into vacuum by a factor of 100 (6), and is about 1/10 of the average rate into vacuum. The comparison is shown in Figure 69, where stucture of the top layers is shown when enough solvent atoms are evaporated and the remaining thickness of the liquid solvent film is very similar.

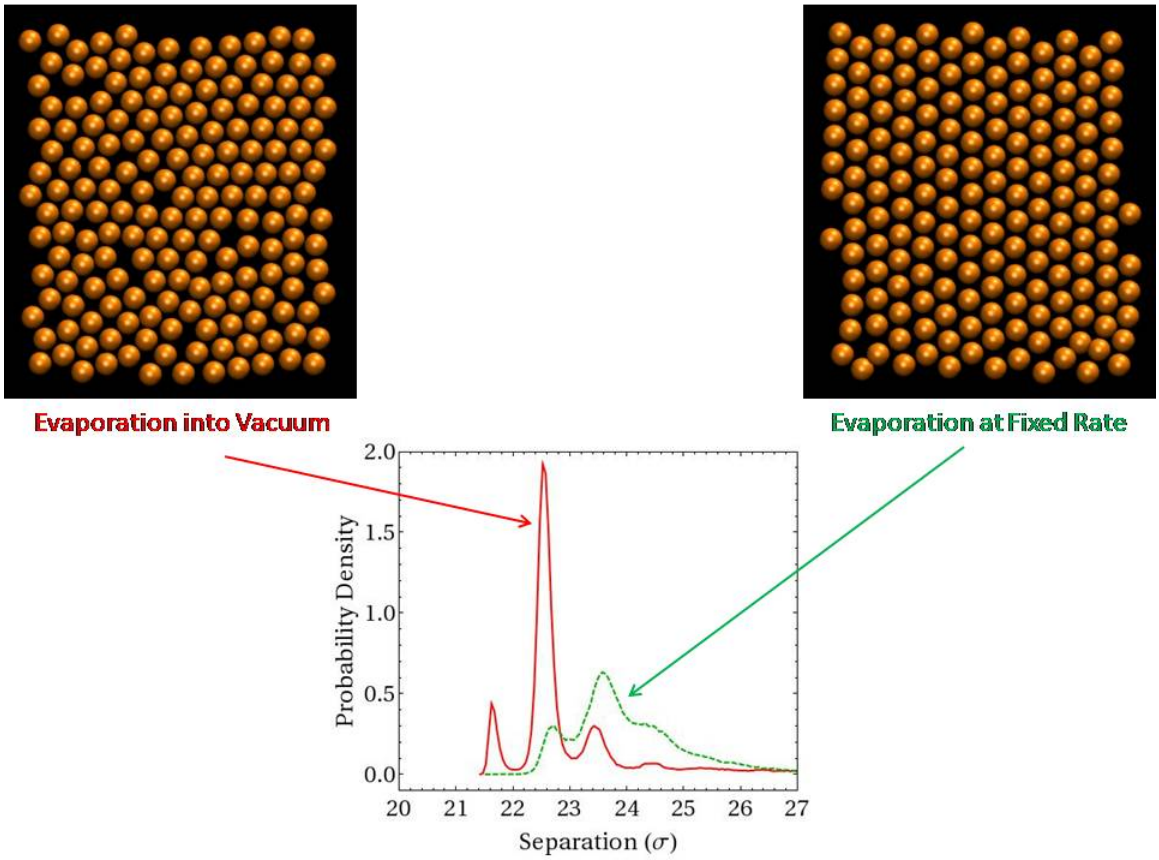

Figure 70: Comparison of assembly structure induced by evaporation into vacuum and evaporation at a small fixed rate (top two pictures). The probability density distribution of inter-nanoparticle separations is shown in the bottom figure.

Figure 69 clearly shows that the assembly quality is better for evaporation at the small fixed rate, in which case nanoparticles assemble into an almost ideal close packed triangular lattice. Note that in both cases the assembled structures may not have sufficient time to completely relax since as seen above if the assembly on the left (for evaporation into vacuum) is allowed to go through a relaxation stage, then it will also adjust into a perfect triangular lattice similar to the structure on the right.

The effect of evaporation rate on assembly quality can be understood from a simple physical picture. Essentially, the assembly process is controlled by the competition of two time scales. One is the time scale to transport nanoparticles to the interface, and another is the time scale for nanoparticles to diffuse along the interface. For the case of evaporation into vacuum, the transport time scale is shorter than the diffusion time scale and the accumulation of nanoparticles is very fast. In this case, local packing of nanoparticles dominates and many grains form with different crystalline orientations. Therefore, many defects and grain boundaries are

produced. However, for the evaporation at the smaller fixed rate, the transport time scale is reduced, but the diffusion time scale remains roughly the same. In this case nanoparticles have

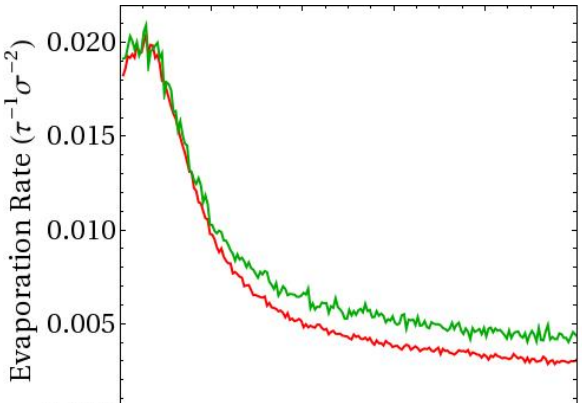

Figure 71: Comparison of evaporation rate vs. time for the pure solvent (green, top curve) and the nanoparticle solution (red, bottom curve).

enough time to diffuse along the interface after they move close to the interface and the assembled lattice gains sufficient time to adjust and relax. As the consequence, the assembly quality induced by slower evaporation is better.

Figure 69 also shows the probability density distribution of inter-nanoparticle separations in the two cases. For evaporation into vacuum, the separations are generally smaller and more strongly peaked. Detailed analyses show that each peak corresponds to an integer number (1, 2, 3, …) of liquid layers between nanoparticles. However, the inter-nanoparticle separations are larger and more broadly distributed for the case of evaporation at the smaller fixed rate. The comparison shows that fast evaporation is more effective to reduce the liquid layer coating the nanoparticles, which are perfectly wetted by the liquid, and push the nanoparticles closer together.

Blockage Effect of Nanoparticle Assembly on Evaporation

There is interplay between the evaporation and evaporation-induced nanoparticle assembly. During evaporation, nanoparticles move towards the interface and assemble into a lattice. Their presence at the interface makes the effective area of latter smaller than the case without nanoparticles. After nanoparticles assemble near the interface, solvent atoms have to circumvent them in order to reach the interface. As the consequence, if the solvent evaporates into vacuum, the evaporation rate will decrease with time (due to depletion of the vapor) faster than the case of pure liquid evaporation. Results are shown in Figure 70, where the evaporation rates of the pure solvent and the corresponding nanoparticle solution are compared. It is obvious that the evaporation rate in the presence of nanoparticles decreases with time more dramatically. This indicates the blockage effect of nanoparticle assembly on evaporation. It can be imagined that if nanoparticles are non-spherical, for example flat platelets, which can align at the interface, the

blockage effect will be much stronger. This remains an interesting direction to investigate further.

4.3 Imprinting pressure on nanoparticle coatings: Pressure-induced phase change

Nanoparticle directed assembly is promising if microstructural control can be realized over large areas and at increased speed. So-called "self-assembly" is a natural process by which particles assembly into a phase-state characterized by a microstructure. On a surface film, such assembly of nanoparticles typically ends up as a hexagonal closed-pack array (HCP) due to van der Waals forces. The evaporation-induced self-assembly process (EISA) is the most commonly knownm method of scaling up scientific experiments of self-assembly into a practical batch or continuous process (through dip coating or spin coating) which can be exploited in manufacturing. Unfortunately, it remains to create a rapid technique to simultaneously drive assembly into different and perhaps more useful structures and at higher speeds. In this section we examine another way to perhaps create non-hexagonal surface microstructure packings of nanoparticles in a fashion which could be combined with a larger scale imprinting process. The work which was funded under this LDRD can be reviewed in papers by Wu et al. (2010). In this document we simply provide a synopsis of this work.

Mimicking embossing and imprinting processes, we developed a pressure-induced assembly method to tune nanoparticle packing and to synthesize new classes of chemical and mechanical stable metal nanostructures. Due to the size- and shape-dependent properties, nanoparticles have been successfully used as functional building blocks to fabricate multi-dimensional (D) ordered assemblies for the development of 'artificial solids' (e.g., metamaterials). At ambient pressure, entropy driven self-assembly of monosized or binary nanoparticles generally results in polycrystalline 2- or 3D close-packed arrangements, and extensive efforts have been made to develop structural perfection of nanoparticle arrays or 'single crystal-like' domain structures with precise long range order for their definite advantages for electron transport. To date, fabrications ofordered nanoparticle assemblies have been relied on specific interparticle chemical or physical interactions such as van der Waals interactions, dipole-dipole interaction, chemical reactions, and DNA-templating, etc. Recently we have discovered a pressure-induced self-assembly method in which an external pressure has been utilized to engineer nanoparticle assembly and to fabricate new nanoparticle architectures without relying onspecific nanoparticle interactions. We show that under a hydrostatic pressure field, the unit cell dimension of a 3D ordered nanoparticle arrays can be manipulated to reversibly shrink, allowing fine-tuning of interparticle separation distance. Under a uniaxial pressurefield, nanoparticles are forced to contact and coalesce, forming hierarchical nanostructures. Depending on the orientation of the initial nanoparticle arrays, 1-3D ordered nanostructures including nanorod, nanowire, and nanoporous network can be fabricated through the pressure-induced self-assembly method. Guided by computational simulations, we were able to rationalize the pressure-induced self-assembly of nanoparticle arrays for predictable nanostructures. Exerting pressure-dependent control over the structure of nanoparticle arrays provides a unique and robust system to understand collective chemical and physical characteristics and to develop novel electronic and photonic behavior for energy transduction related applications.

5. WRAP-UP AND CONCLUSIONS

Nanomanufacturing will continue to be topical for many years as nano-science and nano-technology breakthroughs and discoveries continue to push for practical approaches to application and economic viability. Based on the impact of modeling and simulation in related manufacturing industries (viz. thin-film coating and drying, polymer processing, casting, etc.) we can anticipate that it will play a strong role in the advance of this industry. The work undertaken in this LDRD and summarized here in this report is just the beginning.

We have demonstrated that beyond basic scientific understanding of the underpinning physics and materials of the J-FIL process, there is a crying need for design tools that expedite scale-up, process-control, and process-design. Tools development in the realm of computational mechanics are in their infancy. The distinguishing features of nano-patterning with imprinting, embossing or through directed nanoparticle assembly demand new approaches beyond traditional direct numerical simulation at a continuum scale. The need for true multiscale and multiphysics tools is paramount as is demonstrated in this work. In the continuum regime, reduced order models such as thin-film lubrication, structural shell theory are required to deal with the excessive aspect ratios encountered in thin-film/structure processing. Effective medium approaches (multiphase, porous, etc.) are critical to bridging scales. Fundamental understanding at the molecular level with molecular dynamics is critical to understanding the limits of the process. Finally, tools capability of coupling fluid and structural mechanics are critical in dealing with necessarily complaint systems.

As for the next steps, our work fell short in achieving rigorous cross-scale methodologies for surface interactions. While we laid the groundwork for coarse graining imprinting/release applications which simultaneously produce trillions of features, we fell short of a formal coupling to atomistic scales where friction, surface tension, wetting, and adhesion forces are born. An open question, however, is such a coupling required? It may be sufficient to determine the functional form of these connections by coupling machine-scale models with experiment. A second area of need is a formal methodology for bridging nanoparticle directed assembly simulations at the colloid-colloid level (particle level with LAMMPS, for example) and continuum level with suspension balance modeling. To date the only scale-bridging we utilize is through predicted mobilities (diffusivities), but there is a need to make connections to microstructure measures at the wafer scale.

Successful outcomes in this project are numerous. We list here those which we feel can serve as technology base for current and future customers.

- Production computing capability for applying effective traction-separation laws for adhesive de-bonding of structured rough surfaces (PRESTO).
- Production computing capability for thin-film, thin-gap, thin-porous regions in a generalized shell-element format (GOMA).
- Production capability for modeling the dynamics of polymer-grafted nanoparticles with general polydispersity (LAMMPS)
- Pixel-to-mesh image mapping capability (GOMA)

- Coupled thin-shell lubrication and thin-porous shells with continuum finite element regions of arbitrary physics (GOMA).
- Established capability and workflow for nanomanufacturing processes involving imprint, emboss and release unit operations with arbitrary feature patterns. Validated imprinting capabilities with experimental data from Molecular Imprints Inc.
- Established capability and workflow for modeling the directed assembly of nanoparticles at the meso- and continuum scale.

6. REFERENCES

J. J. Aklonis and W. J. MacKnight (1983). Introduction to Polymer Viscoelasticity, John Wiley and Sons.

N. R. Anturkar, T. C. Papanastasiou, and J. O. Wilkes. Lubrication theory for n-layer thin-film flow with applications to multilayer extrusion and coating. *Chemical Engineering Science*, 45 (11): 3271-3282, 1990.

R. Auhl, R. Everaers, G. S. Grest, K. Kremer, S. J. Plimpton, "Equilibration of long chain polymer melts in computer simulations," J. Chem. Phys. **2003,** 119, 12718.

T. Bailey, B. Smith, B. J. Choi, M. Colburn, M. Meissl, S. V. Sreenivasan, J. G. Ekerdt, and C. G. Willson. Step and flash imprint lithography: Defect analysis. *Journal of Vacuum Science Technology B*, 19 (6): 2806-2810, 2001.

A. R. C. Baljon, M. O. Robbins, "Simulations of crazing in polymer glasses: Effect of chain length and surface tension," Macromolecules, **2001**, 34, 4200.

G. K. Batchelor. An introduction to fluid dynamics. Cambridge Univ Press, 2000.

K. J. Bathe and E. N. Dvorkin. A formulation of general shell elements: The use of mixed interpolation of tensorial components. *International Journal for Numerical Methods in Engineering*, 22 (3): 697-722, 1986. DOI: 10.1002/nme.1620220312.

T. Belytschko, W. K. Liu, and B. Moran. *Nonlinear Finite Elements for Continua and Structures*. John Wiley & Sons, Chichester, New York, 2000.

M. Bhagavat, V. Prasad, and I. Kao. Elasto-hydrodynamic interaction in the free abrasive wafer slicing using a wiresaw: Modeling and finite element analysis. *Journal of Tribology*, 122 (2): 394-404, 2000. DOI: 10.1115/1.555375.

R. C. Bhattacharjee and N. C. Das. Power law fluid model incorporated into elastohydrodynamic lubrication theory of line contact. *Tribology International*, 29 (5): 405-413, 1996. DOI: 10.1016/0301-679X(95)00096-M.

T. P. Bigioni, X. Lin, T. T. Nguyen, E. I. Corwin, T. A. Witten, and H. M. Jaeger, *Kinetically driven self assembly of highly ordered nanoparticle monolayers*, Nature Materials **5**, 265 (2006)

M. Bischoff and E. Ramm. Shear deformable shell elements for large strains and rotations. *International Journal for Numerical Methods in Engineering*, 40 (23): 4427-4449, 1997. DOI: 10.1002/(SICI)1097-0207(19971215)40:23<4427::AID-NME268>3.0.CO;2-9.

J. F. Booker and K. H. Huebner. Application of finite element methods to lubrication: An engineering approach. *Journal of Lubrication Technology*, 94 (4): 313-323, 1972. DOI: 10.1115/1.3451719.

T. D. Blake and J. De Coninck. The influence of solid-liquid interactions on dynamic wetting. *Advances in Colloid and Interface Science*, 96 (1-3): 21-36, 2002.

T.D. Blake and J. De Coninck. The influence of pore wettability on the dynamics of imbibition and drainage. *Colloids and Surfaces A: Physicochemical and Engineering Aspects*, 250 (1-3): 395-402, 2004. DOI: 10.1016/j.colsurfa.2004.05.024.

J. U. Brackbill, D. B. Kothe, and C. Zemach. A continuum method for modeling surface tension. *Journal of Computational Physics*, 100: 335-354, 1992. DOI: 10.1016/0021-9991(92)90240-Y.

E. E. Brodsky and H. Kanamori. Elastohydrodynamic lubrication of faults. *J. Geophys. Res.*, 106 (B8): 16357-16374, 2001.

A. R. Burns, J. E. Houston, et al. (1999). "Molecular Level Friction as Revealed with a Novel Scanning Probe." *Langmuir* **15**: 2922-2930.

R. L. Burns, S. C. Johnson, G. M. Schmid, E. K. Kim, M. D. Dickey J. Meiring, S. D. Burns, N. A. Stacey, C. G. Wilson, "Mesoscale modeling for SFIL simulating polymerization inetics and densification", Emerging Lithographic Technologies VIII, R. S. Mackay, ed. Proceedings of SPIE, Vol. 5374. (2004).

N.M. Bujurke and R.B. Kudenatti. MHD lubrication flow between rough rectangular plates. *Fluid Dynamics Research*, 39 (4): 334-345, 2007.

R. A. Cairncross, P. R. Schunk, K. S. Chen, S. S. Prakash, J. Samuel, A. J. Hurt, and C. J. Brinker. Drying in deformable partially-saturated porous media: Sol-gel coatings. Technical Report SAND96-2149, Sandia National Laboratories, 1996.

R. W. Carpick, and E. E. Flater, et al. (2004). "Atomic-scale Friction and its Connection to Fracture Mechanics." *JOM* **56**: 48-52.

J. M. Y. Carrillo, A. V. Dobrynin, "Molecular Dynamics Simulations of Nanoimprinting Lithography," Langmuir, **2009**, 25, 13244.

S. Cheng, J. B. Lechman, S. J. Plimpton, and G. S. Grest, "Evaporation of Lennard-Jones fluids" *J. Chem. Phys*. **134**, 224704 (2011).

S. Y. Chou, P. R. Krauss, P. J. Renstrom, "Imprint Of Sub-25 Nm Vias And Trenches In Polymers," *Appl. Phys. Lett.* **1995**, *67*, 3114.

S. Chauhan, F. Palmieri, R. T. Bonnecaze, and C. G. Wilson, "Feature Filling Modeling for Step and Flash Imprint Lithography", *J. Vac. Sci. Technol.* B 27(4), Jul/Aug 2009.

H. S. Cheng. "A refined solution to the thermal-elastohydrodynamic lubrication of rolling and sliding cylinders." *ASLE Transactions*, 8 (4): 397-410, 1965. DOI: 10.1080/05698196508972110.

H. Christensen. "Some aspects of the functional influence of surface roughness in lubrication." *Wear*, 17 (2): 149-162, 1971.

H. Christensen. A theory of mixed lubrication. *Proceedings of the Institution of Mechanical Engineers*, 186 (1972): 421-430, 1972.

R. W. Clough and J. Penzien (1975). Dynamics of Structures, McGraw-Hill.

E. Cohen and E. Gutoff, Modern Coating and Drying Technology, Wiley-VCH, New York, 1992.

V. N. Constantinescu. On turbulent lubrication. *Proceedings of the Institution of Mechanical Engineers*, 173: 881-900d, 1959.

D. J. Coyle, C. W. Macosko, and L. E. Scriven. Film-splitting flows in forward roll coating. *Journal of Fluid Mechanics*, 171: 183-207, 1986.

J. V. Cox and H. Yu (1999) "A Micromechanical Analysis of the Radial Elastic Response Associated with Slender Reinforcing Elements within a Matrix," *Journal of Composite Materials*, **33**:2161-2192.

H. Darcy. *The Public Fountains of the City of Dijon.* Kendall Hunt Publishing, 1856. English translation by Patricia Bobeck.

J. E. Drummond and M.I. Tahir. Laminar viscous flow through regular arrays of parallel solid cylinders. *International Journal of Multiphase Flow*, 10 (5): 515-540, 1984. DOI: 10.1016/0301-9322(84)90079-X.

H. G. Elrod and C. W. Ng. "A theory for turbulent films and its application to bearings". *ASEM J. Lubr. Technol.,* 89: 346-362, 1967.

C. Eringen and K. Okada. A lubrication theory for fluids with microstructure. *International Journal of Engineering Science*, 33 (15): 2297-2308, 1995. DOI: 10.1016/0020-7225(95)00071-5.

R. Everaers and M. R. Ejtehadi, "*Interaction potentials for soft and hard ellipsoids"*, Phys. Rev. E **67**, 041710 (2003).

J. Feng and S. Weinbaum. “Lubrication theory in highly compressible porous media: the mechanics of skiing, from red cells to humans”. *Journal of Fluid Mechanics*, 422: 281-317, 2000.

J. Q. Feng. “Computational analysis of slot coating on a tensioned web”. *AIChE Journal*, 44 (10): 2137-2143, 1998.

J. Ferron, J. Frene, and R. Boncompain. A study of the thermohydrodynamic performance of a plain journal bearing; comparison between theory and experiments. *Journal of lubrication technology*, 105 (3): 422-428, 1983.

M. M. Francois, S. J. Cummins, E. D. Dendy, D. B. Kothe, J. M. Sicilian, and M. W. Williams. A balanced-force algorithm for continuous and sharp interfacial surface tension models within a volume tracking framework. *Journal of Computational Physics*, 213 (1): 141-173, 2006.

B. D. Gates and G. M. Whitesides “Replication of Vertical Features Smaller than 2 nm by Soft Lithography”, *J. AM. CHEM. SOC*. 2003, 125, 14986-14987.

Gates, B. D.; Xu, Q. B.; Stewart, M.; Ryan, D.; Willson, C. G.; Whitesides, G. M., “New approaches to nanofabrication: Molding, printing, and other techniques,” Chem. Rev. **2005**, 105, 1171.

G. S. Grest, K. Kremer, “Molecular-Dynamics Simulation For Polymers In The Presence Of A Heat Bath,” Phys. Rev A **1986**, 33, 3628.

G. S. Grest, K. Kremer, “Statistical Properties Of Random Cross-Linked Rubbers,” Macromolecules **1990**, 23, 4994.

M. Herrmann. A balanced force refined level set grid method for two-phase flows on unstructured flow solver grids. *Journal of Computational Physics*, 227 (4): 2674-2706, 2008.

R. S. Hoy, K. Foteinopoulou, M. Kröger, “Topological analysis of polymeric melts: Chain-length effects and fast-converging estimators for entanglement length,” Phys. Rev. E **2009**, 80, 031803.

G. Y. Jung, Z. Y. Li, W. Wu, Chen, Y.; Olynick, D. L.; Wang, S. Y.; Tong, W. M.; Williams, R. S., “Vapor-phase self-assembled monolayer for improved mold release in nanoimprint lithography,” *Langmuir* **2005**, *21*, 1158.

M. S. Kent, H. Yim, et al. (2001). "Use of Self-assembled Monolayers at Variable Coverage to Control Interface Bonding in a Model Study of Interfacial Fracture: Pure Shear Loading." *Journal of Adhesion* **75**: 267-298.

K. Kremer, G. S. Grest, “Dynamics Of Entangled Linear Polymer Melts - A Molecular-Dynamics Simulation,” *J. Chem. Phys.* **1990**, 92, 5057.

G. Martic, F. Gentner, D. Seveno, D. Coulon, J. De Coninck, and T. D. Blake. A molecular dynamics simulation of capillary imbibition. *Langmuir*, 18 (21): 7971-7976, 2002.

D. Morihara, H. Hiroshima, and Y. Harai, "Numerical study on bubble trapping in UV-nanoimprint lithography", *Microelectronic Engineering,* 86 (4-6), pp 684-687 (2009).

N. de Nevers. *Fluid Mechanics for Chemical Engineers.* McGraw Hill, 2nd edition, 1991.

P. K. Notz, S.R. Subia, M. M. Hopkins, H. K. Moffat, D. R. Noble, "Aria 1.5: User's Manual", Sandia National Laboratories Internal Report, SAND2007-2734. (2007).

J. A. Greenwood. An extension of the grubin theory of elastohydrodynamic lubrication. *Journal of Physics D: Applied Physics*, 5 (12): 2195, 1972.

F. Guo, P. Yang, and S. Qu. On the theory of thermal elastohydrodynamic lubrication at high slide-roll ratios--circular glass-steel contact solution at opposite sliding. *Journal of Tribology*, 123 (4): 816-821, 2001.

F. Hauksbee. An experiment touching the ascent of water between two glass plates in an hyperbolick figure. *Philos. Trans. R. Soc. London*, 27: 539, 1712.

M. Heil and T. J. Pedley. Large axisymmetric deformation of a cylindrical shell conveying a viscous flow. *Journal of Fluids and Structures*, 9 (3): 237-256, 1995.

M. Heroux, R. Bartlett, V. Howle R. Hoekstra, J. Hu, T. Kolda, R. Lehoucq, K. Long, R. Pawlowski, E. Phipps, A. Salinger, H. Thornquist, R. Tuminaro, J. Willenbring, and A. Williams. An Overview of Trilinos.

M. Herrmann. A balanced force refined level set grid method for two-phase flows on unstructured flow solver grids. *Journal of Computational Physics*, 227 (4): 2674-2706, 2008.

B. G. Higgins and L. E. Scriven. Capillary pressure and viscous pressure drop set bounds on coating bead operability. *Chemical Engineering Science*, 35 (3): 673-682, 1980.

F. J. Higuera, A. Medina, and A. Linan. Capillary rise of a liquid between two vertical plates making a small angle. *Physics of Fluids*, 20 (10): 102102, 2008.

G. G. Hirs. A bulk-flow theory for turbulence in lubricant films. *ASME Journal of Lubrication Technology*, 95 (2): 137-146, 1973.

Y. Hori. Hydrodynamic Lubrication. Springer Tokyo, 2006.

P. Hryniewicz, A. Z. Szeri, and S. Jahanmir. Application of lubrication theory to fluid flow in grinding: Part I--flow between smooth surfaces. *Journal of Tribology*, 123 (1): 94-100, 2001.

K. H. Huebner. “Application of finite element methods to thermohydrodynamic lubrication. “*International Journal for Numerical Methods in Engineering*, 8 (1): 139-165, 1974.

J. Y. Jang and M.M Khonsari. On the granular lubrication theory. *Proceedings of the Royal Society A: Mathematical, Physical and Engineering Science*, 461 (2062): 3255-3278, 2005.

M. W. Johnson, Jr. and S. Mangkoesoebroto. Analysis of lubrication theory for the power law fluid. *Journal of Tribology*, 115 (1): 71-77, 1993.

D. A. Jones. Elastohydrodynamic lubrication theory. In C.M. Taylor, editor, *Engine Tribology*, volume 26 of *Tribology Series*, pages 15-50. Elsevier, 1993.

M. Kang, R. P. Fedkiw, and X. Liu. A boundary condition capturing method for multiphase incompressible flow. *Journal of Scientific Computing*, 15: 323-360, 2000.

S. F. Kistler and L. E. Scriven. Coating flow theory by finite element and asymptotic analysis of the navier-stokes system. *International Journal for Numerical Methods in Fluids*, 4 (3): 207-229, 1984.

R.E. Kothmann and F. Stefani. A thermal hydraulic model of melt-lubrication in railgun armatures. *Magnetics, IEEE Transactions on*, 37 (1): 86 -91, January 2001.

G. A. LaBouff and J. F. Booker. Dynamically loaded journal bearings: A finite element treatment for rigid and elastic surfaces. *Journal of Tribology*, 107 (4): 505-513, 1985.

X. Liang, H. Tan, Z. Fu, and S. Y Chou. “Air bubble formation and dissolution in dispensing nanoimprint lithography”. *Nanotechnology*, 18 (2): 025303, 2007.

C.W. Macosko. Rheology: principles, measurements, and applications. VCH New York, 1994.

L. E. Malvern. Introduction to the Mechanics of a Continuous Medium. Prentice-Hall, 1969.

M. Mongkolwongrojn and C. Aiumpronsin. “Stability analysis of rough journal bearings under tehl with non-newtonian lubricants”, *Tribology International*, 43 (5-6): 1027-1034, 2010.

K. Prabhakaran Nair, V.P. Sukumaran Nair, and N.H. Jayadas. “Static and dynamic analysis of elastohydrodynamic elliptical journal bearing with micropolar lubricant”. *Tribology International*, 40 (2): 297-305, 2007.

V. P. S. Nair and K. P. Nair. “Finite element analysis of elastohydrodynamic circular journal bearing with micropolar lubricants.” *Finite Elements in Analysis and Design*, 41 (1): 75-89, 2004.

J. Nam and M. S. Carvalho. “Flow in tensioned-web-over-slot die coating: Effect of die lip design”. *Chemical Engineering Science*, 65 (13): 3957 -3971, 2010.

C. W. Ng. “Fluid dynamic foundation of turbulent lubrication theory”. *ASLE Transactions*, 7 (4): 311-321, 1964.

C. W. Ng and E. Saibel. “Nonlinear viscosity effects in slider bearing lubrication.” *J. Basic Eng*, 84: 192-196, 1962.

N. Nguyen-Thanh, T. Rabczuk, H. Nguyen-Xuan, and S. P.A. Bordas. “A smoothed finite element method for shell analysis.” *Computer Methods in Applied Mechanics and Engineering*, 198 (2): 165-177, 2008.

NSS User Manual V1.02. COGNOSCENS NIL Modeling Package. Copyright © 2010 Cognoscens SARL

K. P. Oh and K. H. Huebner. “Solution of the elastohydrodynamic finite journal bearing problem”. *Journal of Lubrication Technology*, 95 (3): 342-351, 1973.

E. Olsson, G. Kreiss, and S. Zahedi. “A conservative level set method for two phase flow II”. *Journal of Computational Physics*, 225 (1): 785-807, 2007.

A. Oron, S. H. Davis, and S. G. Bankoff. “Long-scale evolution of thin liquid films”. *Reviews of Modern Physics*, 69 (3): 931-980, Jul 1997.

N. Otsu. “A threshold selection method from gray level histograms”. *IEEE Trans. Systems, Man and Cybernetics*, 9: 62-66, 1979.

R. L. Panton. Incompressible Flow. Wiley, 3rd edition, 2005.

R. D. Piner, J. Zhu, F. Xu, S. Hong, C. A. Mirkin, “"Dip-pen" nanolithography,” *Science* **1999**, *283*, 661.

E. D. Reedy, J. V. Cox, “Modeling Nanofabrication Imprint and Release Steps: Adhesion Effects”, Proceed. Of the 33rd Annual Meeting of The Adhesion Society, Daytona Beach, Fl., Feb. 21-24, 2010.

E. D. Reedy, E. D., (2006). "Thin-Coating Contact Mechanics with Adhesion." *Journal of Materials Research* **21**: 2660-2668.

E. D. Reedy, Jr., F. J. Mello, et al. (1997). "Modeling the Initiation and Growth of Delaminations in Composite Structures." *Journal of Composite Materials* **31**: 812-831.

E. D. Reedy, Jr., M. J. Starr, et al. (2005). *Contact Modeling of Sam-Coated Polysilicon Asperities*. 28th Annual Meeting of The Adhesion Society, Mobile, AL.

S. Reddy, R. T. Bonnecaze, 2005 “Simulation of fluid flow in the Step and Flash Imprint Lithography process”, (354 KB) *Microelectronics Engineering*, **82**, 60-70.

S. Reddy, P. R. Schunk, R. T. Bonnecaze, "Dynamics of low capillary number interfaces moving through sharp features", *Physics of Fluids*, 17(12): 122104/1-122104/6, 2005.

O. Reynolds. On the theory of lubrication and its application to Mr. Beauchamp Tower's experiments, including an experimental determination of the viscosity of olive oil. *Philosophical Transactions of the Royal Society of London*, 177: 157-234, 1886.

S. A. Roberts, D. R. Noble, P. R. Schunk, and E. M. Benner. Multiphase hydrodynamic lubrication flow using a three-dimensional shell finite element model. *International Journal for Numerical Methods in Fluids*, 2012, *in preparation*.

N. O. Rojas, M. Argentina, E. Cerda, and E. Tirapegui. Inertial lubrication theory. *Physical Review Letters*, 104 (18): 187801, May 2010.

H. D. Rowland, W. P. King, A. C. Sun, and P. R. Schunk, "Simulations of non-uniform embossing: the effect of asymmetric neighbor cavities on polymer flow during nanoimprint lithography", Internal Report, Sandia National Laboratories, SAND2007-4121 (2007).

H. D. Rowland, W. P. King, A. C. Sun, and P. R. Schunk, GLW 2008. "Predicting polymer flow during high-temperature atomic force microscope nanoindentation" *Macromolecules.* Vol.40, iss.22, p.8096-8103

H. D. Rowland, W. P. King, A. C. Sun, and P. R. Schunk 2005. "Simulations of nonuniform embossing: The effect of asymmetric neighbor cavities on polymer flow during nanoimprint lithography*", J. Vac. Sci. Technol. B* **23**(6), 2958-2962.

H. D. Rowland, A. C. Sun, P. R. Schunk, W. P. King, 2005. "Impact of polymer film thickness and cavity size on polymer flow during embossing: toward process design rules for nanoimprint lithography". *J. Micromech. Microeng.* **15**, 2414-2425.

R. Ruchhoeft, M. Colburn, B. Choi, H. Nounu, S. Johnson, T. Bailey, S. Damle, M. Stewart, J. Ekerdt, S. V. Sreenivasan, J. C. Wolfe, C. G. Willson, "Patterning curved surfaces: Template generation by ion beam proximity lithography and relief transfer by step and flash imprint lithography," *J. Vac. Sci. Technol. B* **1999**, *17*, 2965.

P. A. Sackinger, P. R. Schunk, and R. R. Rao. A newton-raphson pseudo-solid domain mapping technique for free and moving boundary problems: A finite element implementation. *Journal of Computational Physics*, 125 (1): 83-103, 1996. DOI: 10.1006/jcph.1996.0081.

W. M. Scherzinger and D. C. Hammerand (2007). Constitutive Models in LAME, SAND2007-5873, Sandia National Laboratories.

P. R. Schunk, P. A. Sackinger, R. R. Rao, K. S. Chen, T.A. Baer, D. A. Labreche, A. C. Sun, M. M. Hopkins, S. R. Subia, H. K. Moffat, R. B. Secor, R. A. Roach, E. D. Wilkes, D. R. Noble, P. L. Hopkins, and P. K. Notz. Goma 5.0 - a full-newton finite element program for free and

moving boundary problems with coupled fluid/solid momentum, energy, mass, and chemical species transport: User's guide. Technical report, Sandia National Laboratories, 2006.

H. Schift and L.J. Heyderman. volume Alternative Lithography, Volume editor C. Sotomayor Torres of Nanostructure Science and Technology, chapter Nanorheology, pages 1– 37. Kluwer Academic /Plenum Publishers, 2004.

S. Singhal and S. V. Sreenivasan. Experimental movies of drop spreading under unpatterned, transparent templates. Personal communication, 2011.

S. V. Sreenivasan. Nanoscale manufacturing enabled by imprint lithography. *MRS Bulletin*, 33: 854-863, 2008.

H.A. Stone. On lubrication flows in geometries with zero local curvature. *Chemical Engineering Science*, 60 (17): 4838-4845, 2005. DOI: 10.1016/j.ces.2005.03.021.

S. Stoyanov, T. Tilford, F. Amalou, S. Cargill, C. Bailey, M. Desmulliez, "Modeling and optimization study on the fabrication of nano-structures using imprint forming process", Int. J. for Computer-Aided Engineering and Software, Vol. 28(1), 93-111, (2011).

M. Sussman, K.M. Smith, M.Y. Hussaini, M. Ohta, and R. Zhi-Wei. A sharp interface method for incompressible two-phase flows. *Journal of Computational Physics*, 221 (2): 469-505, 2007. DOI: 10.1016/j.jcp.2006.06.020.

M. Sussman. A second order coupled level set and volume-of-fluid method for computing growth and collapse of vapor bubbles. *Journal of Computational Physics*, 187 (1): 110-136, 2003.

S. T. N. Swamy, B. S. Prabhu, and B. V. A. Rao. Steady state and stability characteristics of a hydrodynamic journal bearing with a non-newtonian lubricant. *Wear*, 42 (2): 229-244, 1977.

A. Z. Szeri. *Fluid film lubrication*. Cambridge Univ Press, 2010. ISBN 0521898234.
B. Taylor. Concerning the ascent of water between two glass plates. *Philos. Trans. R. Soc. London*, 27: 538, 1712.

C. Taylor and JF O'Callaghan. "A numerical solution of the elastohydrodynamic lubrication problem using finite elements", *Journal of Mechanical Engineering Science*, 14 (4): 229-237, 1972.

H. Taylor, Y. C. Lam, D. Boning, "A computationally simple method for simulating the micro-embossing of thermoplastic layers", *J. Micromechanics and Microeng.* 19, 075007-075024 (2009).

B. Tower. First report on friction experiments. *Proceedings of the Institution of Mechanical Engineers*, 34 (1883): 632-659, 1883.

S. Wada, H. Hayashi, and M. Migita. Application of finite-element method to hydrodynamic lubrication problems: Part 1, infinite-width bearings. *Bulletin of the Japan Society of Mechanical Engineers*, 14: 1222-1233, 1971a.

S. Wada, H. Hayashi, and M. Migita. Application of finite-element method to hydrodynamic lubrication problems: Part 2, finite-width bearings. *Bulletin of the Japan Society of Mechanical Engineers*, 14: 1234-1244, 1971b.

H. Wu, F. Bai, Z. Sun, R. E. Haddad, D. M. Boye, Z. Wang, and H. Fan, "Pressure-Driven Assembly of Spherical Nanoparticles and Formation of 1D-Nanostructure Arrays", *Angew. Chem. Int. Ed.* 2010, 49, 8431 –8434

H. Wu, F. Bai, Z. Sun, R. E. Haddad, D. M. Boye, Z. Wang, J. U. Huang, and H. Fan, Nanostructured Gold Architectures Formed through High Pressure-Driven Sintering of Spherical Nanoparticle Arrays"**,** *J. Am. Chem. Soc.* 2010, *132*, 12826–12828.

P. Yang, S. Qu, Q. Chang, and F. Guo. On the theory of thermal elastohydrodynamic lubrication at high slide-roll ratios--line contact solution. *Journal of Tribology*, 123 (1): 36-41, 2001.

Y. Yang and M. Ruths (2009). "Friction of Polyaromatic Thiol Monolayers in Adhesive and Nonadhesive Contacts." *Langmuir* **25**: 12151-12159.

Y. Zhang and S. Wen. An analysis of elastohydrodynamic lubrication with limiting shear stress: Part I. Theory and solutions. *Tribology Transactions*, 45 (2): 135-144, 2002.

Zhao, X. M.; Xia, Y. N.; Whitesides, G. M., "Soft lithographic methods for nano-fabrication," J. Mater. Chem. **1997**, 7, 1069.

.

DISTRIBUTION

1 Kristianto Tjiptowidjojo
Department of Chemical and Nuclear Engineering
University of New Mexico
tjiptowi@unm.edu (Electronic Copy)

1	MS0836	Scott Roberts	1514 (electronic copy)
1	MS0836	Randy Schunk	1516 (electronic copy)
1	MS0836	Marcy Hoover	1516 (electronic copy)
1	MS1303	Gary Grest	1114 (electronic copy)
1	MS1314	Shengfeng Cheng	1814 (electronic copy)
1	MS0889	Mike Chandross	1814 (electronic copy)
1	MS0346	Dave Reedy	1526 (electronic copy)
1	MS0824	Jim Cox	1524 (electronic copy)
1	MS1349	Hongyou Fan	1815 (electronic copy)
1	MS0899	RIM-Reports Management	9532 (electronic copy)

For LDRD reports, add:

1	MS0359	D. Chavez, LDRD Office	1911 (electronic copy)


Sandia National Laboratories